Numerical Study of Cloud-Sized Droplet Impact and Freezing on Superhydrophobic Surfaces

Seyed Mohammad Reza Attarzadeh Niaki

A Thesis

in

the Department

of

Mechanical, Industrial and Aerospace Engineering

Presented in Partial Fulfillment of the Requirements

For the Degree of

Doctor of Philosophy (Mechanical Engineering) at

Concordia University

Montreal, Quebec, Canada

November 2017

CONCORDIA UNIVERISTY

School of Graduate Studies

This is to certify that the thesis prepared,

By: **Seyed Mohammad Reza Attarzadeh Niaki**

Entitled: **Numerical Study of Cloud-Sized Droplet Impact and Freezing on Superhydrophobic Surfaces**

and submitted in partial fulfillment of the requirements for the degree of

Doctor of Philosophy (Mechanical Engineering)

Complies with the regulations of the University and meets the accepted standards with respect to originality and quality.

Signed by the final examining committee:

_____ Chair
Dr. Mojtaba Kahrizi

_____ External Examiner
Dr. Mina Hoorfar

_____ External to Program
Dr. Amir Aghdam

_____ Examiner
Dr. Christian Moreau

_____ Examiner
Dr. Marius Paraschivoiu

_____ Thesis Supervisor
Dr. Ali Dolatabadi

Approved by _____
Dr. Martin Pugh, Chair
Department of Mechanical, Industrial and Aerospace Engineering

November 31st, 2017

_____
Dr. Amir Asif, Dean
Faculty of Engineering and Computer Science

Abstract

Numerical Study of Cloud-Sized Droplet Impact and Freezing on Superhydrophobic Surfaces

Reza Attarzadeh, Ph.D.

Concordia University, 2017

In-flight icing is a serious meteorological hazard caused by supercooled cloud particles (with an average size of 20–50 μm) that turn into ice as an immediate consequence of impact with an aircraft, and it poses a serious risk to the safety of the aircraft and its passengers. Anti-icing surface treatment is a potential solution to mitigate ice accretion and maintain optimal flying conditions. Superhydrophobic coatings inspired by nature (e.g., lotus leaf) have attracted much attention in recent years due to their excellent water repellent properties. These coatings have been extensively applied on various substrates for self-cleaning, anti-fogging, and anti-corrosive applications. The performance of these coatings depends on the chemical composition and their rough hierarchical surface morphology composed of micron and sub-micron-sized structures. Recently, there has been an increased interest to fabricate superhydrophobic coatings that can repel droplets of cloud-relevant sizes (20–50 μm) before they freeze to the surface in practical flight conditions (i.e., icephobic surfaces).

The main goal of this work was to numerically model the hydrodynamic and thermal behaviour of cloud-sized droplets on superhydrophobic surfaces when interacting with micron-sized surface features. Consequently, by correlating the hydrophobicity and the icephobicity of the surface, we found viable solutions to counteract icing and to prevent ice accumulation on critical aerodynamic surfaces. For this purpose, we developed a computational model to analyze the hydrodynamics of the impact of the micro-droplet on a micro-structured superhydrophobic surface under room temperature and freezing (including rapid-cooling and supercooling) conditions. All coding and implementations were carried out in the OpenFOAM platform, which is a collection of open-source C++ libraries for computational continuum mechanics and CFD analysis.

Superhydrophobic surfaces were directly modelled as a series of fine, micro-structured arrays with defined cross sections and patterns. Surface chemistry was included in the simulations using a dynamic contact angle model that describes well the hydrodynamics of a micro-droplet on rough surfaces. A multi-region transient solver for incompressible, laminar, multi-phase flow of non-isothermal, non-Newtonian fluids with conjugate heat transfer boundary conditions between solid and fluid regions was developed to simulate both the dynamics of the micro-droplet impact on the substrate and the associated heat transfer inside the droplet and the solid bulk simultaneously. In addition, a phase change (freezing) model was added to capture the onset of ice formation and freezing front of the liquid micro-droplet. The computational model was validated using experimental data reported in the literature. In addition, an analytical model was derived using the balance of energy before impact and at the maximum spreading stage, which we found to be in good agreement with the data obtained from simulations.

Since aluminum (Al) is the base material used in aerospace industries, the thermo-physical properties of aluminum were extensively used in our simulations. Comparing laser-patterned aluminum substrates with a ceramic base composite material that has a low thermal diffusivity (such as titanium-dioxide), we showed that the onset of icing was significantly delayed on the ceramic-based substrate, as the droplet detached before freezing to the surface. Finally, a freezing model for the supercooled water droplet based on classical nucleation theory was developed. The model is an approximation for a supercooled droplet of the recalescence step, which was assumed to be initiated by heterogeneous nucleation from the substrate. This research extended our knowledge about the hydrodynamic and freezing mechanisms of a micro-droplet on superhydrophobic surfaces. The developed solvers can serve as a design tool to engineer the roughness and thermo-physical properties of superhydrophobic coatings to prevent the freezing of cloud-sized droplets in practical flight conditions.

Contribution of Authors

This thesis is prepared in manuscript format. Chapters 2, 3, 4, 5 and 6 are reprinted from journal papers with minor modifications. Reza Attarzadeh who is the author of the current thesis, is the first author of these journal papers. He is responsible for running the simulations, development and implementation of methods, and post processing the results. The papers titles, journals names, volumes numbers, pages numbers, and the contribution of the co-authors are given below:

Chapter 1: this is to serve as an introduction to the subject. Relevant terms and terminologies are introduced and discussed, and previous research studies are highlighted. In addition, it contains detailed description of the research objective and the research structure.

Chapter 2: the paper entitled "Numerical modelling of droplet impact on micro-structured superhydrophobic surface" is submitted to the "Journal of engineering science". The co-author of this paper is the project supervisor, Prof. Ali Dolatabadi.

Chapter 3: the paper entitled "Coalescence-Induced Jumping of Micro-Droplets on Heterogeneous superhydrophobic Surfaces" is published in the "Journal of Physics of Fluids, 2017, volume 29, pages 012104". The co-author of this paper is the project advisor, Prof. Ali Dolatabadi.

Chapter 4: the paper entitled "Numerical Study of the Effect of Surface Wettability on the Performance of the Spray Cooling Process" is published in the international "Journal of Computational Methods and Experimental Measurements, 2016, volume 4, pages 615-624". Prof. Ali Dolatabadi is the supervisor of the project and the co-author of this paper.

Chapter 5: the paper entitled "Icephobic Performance of superhydrophobic Coatings: A Numerical Analysis" is submitted to the "Journal of Aerospace Engineering". Prof. Ali Dolatabadi as the project advisor is the co-author of this paper.

Chapter 6: the paper entitled "On the Numerical Modelling of Supercooled Micro-Droplet Impact and Freezing on Hydrophilic and superhydrophobic Surfaces" has been submitted to the international Journal of Mass and Heat Transfer. Dr. Moussa Tembely, and Prof. Ali Dolatabadi are the co-authors of the paper. Dr. Tembely helped on theoretical development of the model. Numerical implementation, simulations and results gathering was performed by the main author of this thesis. The research advisor was Prof. Dolatabadi.

Acknowledgements

Firstly, I would like to express my sincere gratitude to my advisor Prof. Ali Dolatabadi for the continuous support of my Ph.D. study, for his patience, motivation, and immense knowledge. His guidance helped me in all the time of research and writing of this thesis. I could not have imagined having a better advisor and mentor for my Ph.D. study.

I would also like to express my appreciation to my second mentor, Dr. Moussa Tembely, and all my colleagues, Ali Nozari, Kourosh Pourang, Mehdi Jadidi, Firoozeh Yeganehdoust and Fariba Haghbin for helping me in several stages of my research. I would also like to thank my committee members for their helpful comments and ideas.

Last but not least, I would like to say a very special thank you to my parents, my brother, and my sister for their love, encouragement and supporting me spiritually throughout writing this thesis and various stages of my life.

Table of Contents

List of Figures

List of Tables

Nomenclature

A	Projected area
c	Sound speed
C	Specific heat
C_a	Capillary number
C_o	Compression Coefficient
D	Droplet diameter
D_0	Droplet initial diameter
D_m	Droplet maximum spreading diameter
D_c	Droplet maximum contact diameter
E	Total energy
E_K	Kinetic energy
E_S	Surface energy
F_b	Body force term
F_{sa}	Surface force term
F_{sv}	Volume force term
G	Pillars spacing
h	Convective heat transfer coefficient
H	Pillars height
H^*	Non-dimensional droplet penetration depth
h_{fs}	Latent heat of fusion
H_x	Pancake height

k_l	Liquid-solid transition coefficient
k	Thermal conductivity
K_n	Knudsen number
m	Mass
M	Mach number
n	Face unit normal flux
N_c	Pre-factor in nucleation rate expression
p	Pressure
P_{wh}	Water hammer pressure
P_D	Dynamic pressure
P_C	Capillary pressure
Pr	Prandtl number
q	Heat transfer rate
r	Droplet radius
R	Surface Roughness
Re	Reynolds number
S	Cell surface area
S_f	Cell face area vector
S_H	Energy source term
S_V	Momentum source term
t	Time
t_{ic}	Inertia-capillary time scale
T	Temperature
T_{ref}	Reference Temperature

V	Velocity
V_c	Vector of relative velocity normal to the interface
V_r	Relative velocity
V_{ic}	Inertia-capillary velocity scale
W	Pillars width
We	Weber number
x	Coordinate direction and distance
y	Coordinate direction and distance

Greek letters

α	Volume fraction
α_t	Thermal diffusivity
β	Parameter defined in Karman cozny formulation
γ	Karman cozny coefficient
δ	Small value (10^{-6})
δ_b	Boundary layer thickness
Δx	Mesh size
Δt	Time steps
Δt_c	Contact time
ΔG	Gibbs free energy
ε	Relative roughness
κ	Interface curvature
λ	Coupling interface (solid-fluid)
μ	Viscosity

ρ	Density
σ	Surface tension
τ	Shear stress
Π, Λ	Penetration coefficients
ϕ	Viscous dissipation
ψ	Face volume flux
χ	Dependent of Stefan number
Φ_s	Solid fraction in contact
φ	Face volume flux

Abbreviations

ALE	Arbitrary Lagrangien Eulerian
VOF	Volume of fluid method
LS	Level-set method
MAC	Marker and cells method
LBM	Lattice Boltzmann method
PFM	Phase field
SHS	Superhydrophobic surface
OF	OpenFOAM
CSF	Continuum surface force model

Subscripts

avg	Average

l	liquid
f	fluid
g	Gas
s	solid
d	droplet
C	capillary
WH	water hammer
D	dynamic
x	In axial direction
y	In normal direction

Chapter 1

Introduction

1.1 Motivation

Aircraft icing is known as one of the critical aviation safety issues. Although the equilibrium freezing temperature of water is at 0° C, water does not always freeze at that temperature and sometimes exists as a "supercooled" liquid. If the surface temperature of an aircraft structure flying through the clouds is below zero, then supercooled droplets may turn to ice as an immediate or secondary consequence of impact. Flying in icing condition causes the formation of ice layers which can result in the increased aerodynamic drag, reduced lift, and reduced aircraft control. Accumulation of ice disturbs the airflow pattern and consequently deviates the plane from optimal flight condition. There have been around 2000 icing-related reports from 1978 to 2002, and 228 incidents from 2006 to 2010 in the US, from which 723 incidents are considered aerodynamically significant [1].

Figure 1-1: Examples of unfavorable and catastrophe of ice accretion, a) Ice accumulation on the spinner of a jet engine [2], b) ice growth on the surface of the airfoil [3], and c) Avionic catastrophe as the result of airframe icing [4].

Only in the year 2002, the icing was the primary cause of $96 million regarding personal injuries and damages in the USA [5]. Weight gain from ice accumulation on the airframe can become a tremendous safety challenge for smaller aircraft. In addition to the impacts on the airframe, high ice density can extinguish engines (flame-outs), and ice accumulation can cause the failure of Pitot data sensor, thereby eliminating information required for safe flight. Figure 1-1 shows few examples of unfavorable ice accretion during flight.

Utilization of powered heat source to meltdown the ice is known as one of the practical solutions to mitigate ice accretion on airplane components such as the blades, airframe and airfoils. However, this requires additional installment which makes the airplane heavier and consequently, increases fuel consumption. An alternative potential solution is to treat the surfaces in such a way that they are immune to icing, i.e., ice does not form on them. Surfaces with extreme water repelling behavior have proven to exhibit excellent anti-icing property under specific condition.[6]. These surfaces are called superhydrophobic (SH) surfaces. Studies have also shown [7], [8] that in case of ice formation on a surface, superhydrophobic surfaces are beneficial since ice detachment from these surfaces requires less heating compared to conventional surfaces. According to a study [9], ice formation on superhydrophobic surfaces under specific configurations can be alleviated since supercooled water droplets do not easily stick to these surfaces and mainly bounce off and detach from the surface before they start to freeze. However, these studies are limited to large size droplets (i.e. millimeter size droplet) interacting with a superhydrophobic surface whereas the incident of aircraft icing is due to the impact of cloud-sized droplets (20-50 μm). Since the size of droplets in cloud is too small, i.e. comparable to the scale of surface asperities, hydrodynamic of the droplet during the impact and freezing may change from the case of milimiter size droplet impact.

It is important to mention that experimental study of a micro-droplet impact on the rough superhydrophobic surface is complicated and very limited due to the time scale associated with the droplet impact phenomena (on the order of microseconds) and limited imaging capabilities in this scale. Therefore, the computational tool can overcome difficulties above and provide more detailed information under varied conditions. By improving our understanding of micro-droplet interactions with superhydrophobic surfaces, and eventually finding the relationship between superhydrophobic and icephobic properties we can aim for a long-standing industrial solution to manufacture functional ice-free surfaces. To this objective, key developments in the field of droplet impact will be concisely discussed in the next section.

1.1 Surface wettability

The shape of a droplet sitting on a surface depends on the interaction between the liquid and the solid surface. If there is a high adhesion force between the liquid and the solid, liquid spreads over the surface. On the contrary, for low-adhesive surfaces, the liquid droplet hates the surface and tends to keep its spherical shape. Such behavior is described quantitatively by the concept of contact angle measured between droplet and solid surface at the three-phase contact line in a thermal equilibrium state (Figure 1-2). The more the contact angle, the more hydrophobic the surface, consequently the more spherical the droplet. Young's equation (eqn.1-1) [10] describes the balance of surface tension forces for a sessile droplet under equilibrium condition.

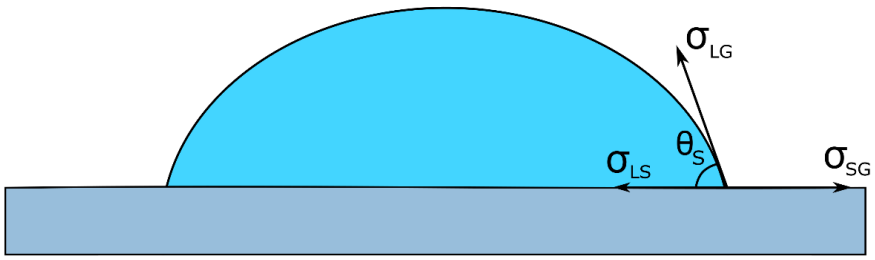

Figure 1-2: Equilibrium (static) contact angle of a sessile droplet

$$\cos\theta_s = \frac{\sigma_{SG} - \sigma_{LS}}{\sigma_{LG}} \tag{1-1}$$

where θ_s, σ_{SG}, σ_{LS}, σ_{LG}, corresponds to the static contact angle, solid-gas, liquid-solid, liquid-gas interfacial energies, respectively. The static contact angle divides the entire range of surface wettability into two regimes (Figure 1-3), hydrophilic and hydrophobic. For a static contact angle of $\theta_s < 90^{\circ}$ droplet spreads, wetting occurs, and the surface is called hydrophilic. For a contact angle $\theta_s > 90^{\circ}$ the surface is called hydrophobic and droplet tends to keep its spherical shape. Furthermore, if the contact angle increases beyond 150° the surface is so-called superhydrophobic or water repellent surface [11], [12].

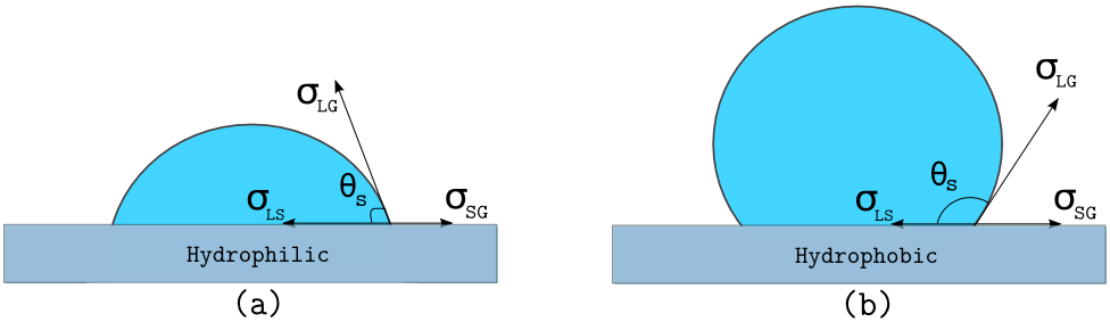

Figure 1-3: Different wetting behavior: a) Hydrophilic, b) Hydrophobic.

Superhydrophobicity of a surface is associated with both surface roughness and the surface chemistry. The surface chemistry refers to the presence of a preponderance of nonpolar bonds in molecular lattice structure of the substrate. Because water molecules are polar, that seemingly has little tendency to be surrounded by polar bonds so called hydrophobes, and they get repelled. Figure 1-4.a) shows the molecular structure of hydrocarbons, which contain many C-H bonds which are hydrophobic and do not interact with H_2O molecules. Figure 1-4.b) is an example of

physically modified superhydrophobic by including the effect of surface roughness and decreasing the area of surface adhering with a liquid droplet.

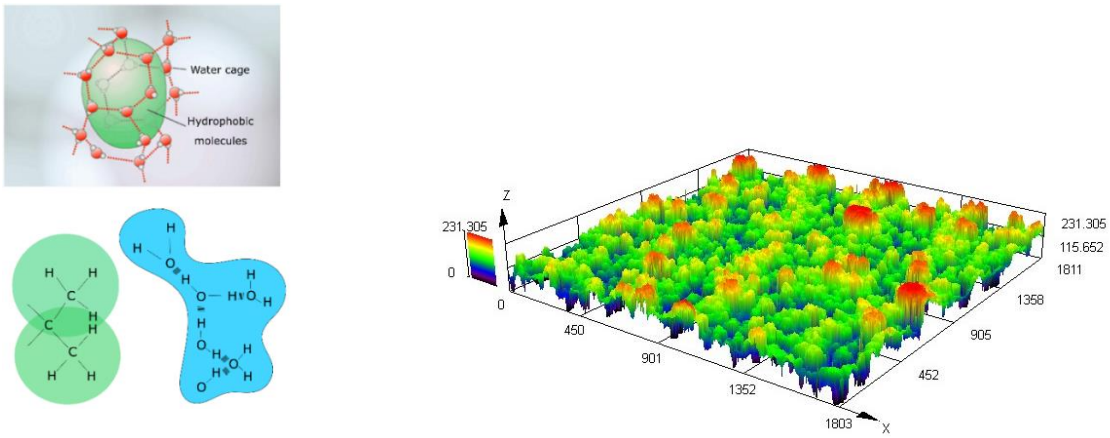

(a) (b)

Figure 1-4: A comparison between a) surface chemistry of superhydrophobic surfaces, b) Confocal microscopy of a superhydrophobic surface topology.

Researchers have been trying to determine which kind of sub-micron or nanostructures can make a surface superhydrophobic or superhydrophilic. To obtain these special properties, they have been looking at the examples in nature such as how Namib desert beetle collects water to drink or the self-cleaning property of lotus leaf (Figure 1-5).

Figure 1-5: Examples of superhydrophobic surface in nature, Namib beetle (left) [13] and lotus leaf (right) [14].

The lotus leaf has excellent water repellency and mobility [15]. The water droplet impinging on lotus leaf can bounce or roll off the surface and more likely remove dust and dirt particles. Figure 1-5 shows a water droplet sitting on the surface of the lotus leaf. As it can be seen, the surface of a lotus leaf is not perfectly smooth; rather it consists roughness on the micrometer scale. The entrapped air between asperities prevents water from contacting the entire solid surface and causing low adhesion (or surface energy). The low surface energy of the lotus leaf causes the water droplet to assume a nearly spherical shape, and the surface becomes repellent.

There are two different states when a water droplet comes in contact with a rough surface. The first state is the Wenzel state [16] (Figure 1-6.a), in which there are no air pockets underneath the water droplet, and the droplet is in complete contact with the surface. The droplet sticks very well to the surface, and it is called pinned droplet. In the Wenzel model, the surface roughness is quantified by "*r"* which is the real surface area divided by the projected surface area. Since every surface has some roughness, and no surface is completely smooth in the molecular level we can assume that *r* is always greater than one. The Wenzel model describes the contact angle of a droplet sitting on a rough surface in the following way,

$$\cos\theta_p = r\cos\theta_s \qquad (1\text{-}2)$$

where θ_p is the apparent contact angle or the contact angle droplet creates while sitting on a rough surface. Since *r* is greater than one, $\cos\theta_p > \cos\theta_s$ .This is an important statement, since if a surface is hydrophilic ($\theta_s < 90$), the increase in roughness makes the surface more hydrophilic.

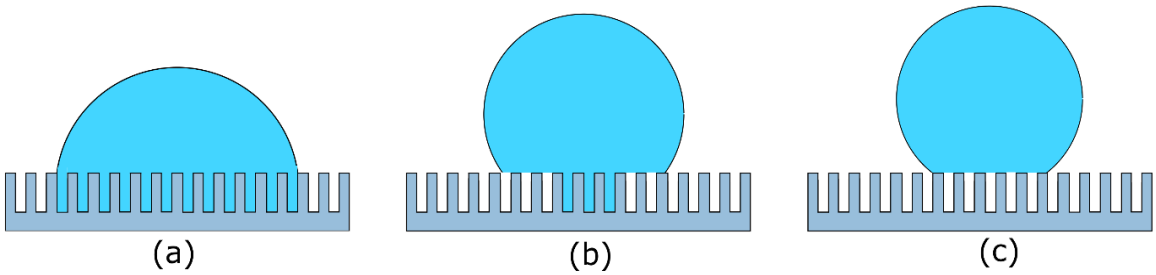

Figure 1-6: Different state of a droplet sitting on a rough surface; a) Wenzel state, b) Wenzel to Cassie-Baxter state (Mushroom), and c) Cassie-Baxter state.

The second state is the Cassie-Baxter state [17] in which the water droplet is in contact with both solid surface and air pockets trapped in the surface asperities. This property is useful for water repellent and self-cleaning surfaces. Technically, Cassie-Baxter state can occur for very rough surfaces. The Cassie-Baxter model describes the apparent contact angle in terms of the percentage of solid surface that is in contact with the liquid droplet as follow,

$$\cos\theta_p = -1 + \Phi_s(\cos\theta_s + 1) \qquad (1\text{-}3)$$

where, Φ_s, is the percentage (%) of solid surface which is in contact with the liquid droplet. According to eqn (1-3) if the water droplet is mostly sitting on the air pocket, then $\Phi_s \longrightarrow 0$, hence $\theta_p \longrightarrow 180^{\circ}$ which corresponds to the situation when droplet is fully spherical.

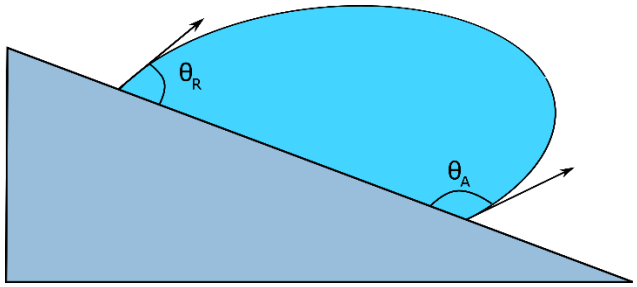

Figure 1-7: Tilting plate method for measurement of the advancing (θ_A) and receding (θ_R) contact angles.

Furthermore, surface mobility or the tendency of a droplet to shed from the surface is categorized using the contact angle hysteresis. Contact angle hysteresis is the difference between the advancing, θ_A, and receding, θ_R, contact angles. The smaller the contact angle hysteresis, the higher surface's mobility. The superhydrophobic surfaces are characterized by having a low contact angle hysteresis; smaller than 10° [18], [19]. There are various experimental methods to measure the contact angle hysteresis of a surface. One common technique is the tilting plate shown schematically in Figure 1-7. The tilting plate requires inclination of the surface carrying the droplet, and measuring the top and bottom angles right before the droplet starts to slide. However, for small size droplets this method does not produce effective results since the effect of gravitational force is negligible on the motion of the droplet. This behavior has been quantified using the Bond number ($Bo = \rho g D^2/\sigma$), which is the ratio of gravitational force to surface force. Therefore, for droplets with very small Bond number (D < 100 µm), the volume changing method (filling method) is used for measurement of droplet contact angle hysteresis (Figure 1-8). In this method, a droplet is injected and removed through a needle over the surface where the advancing and receding contact angles are measured during the ejection and removal of the liquid volume.

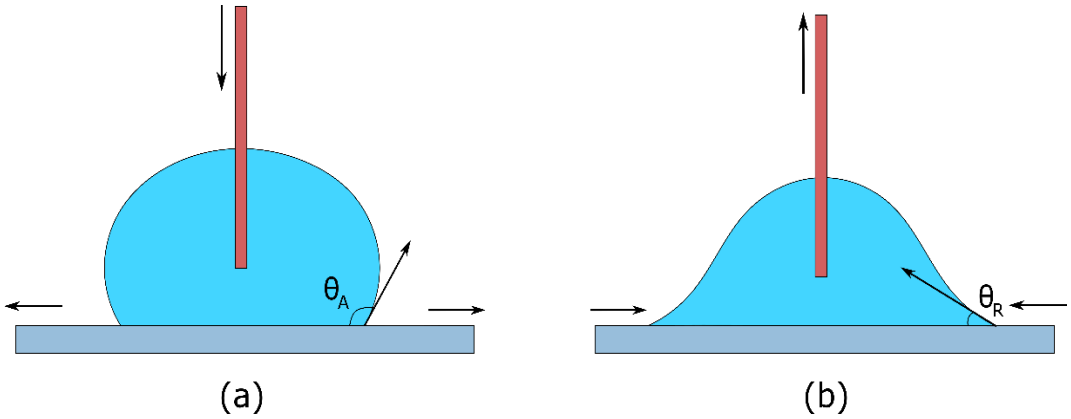

Figure 1-8: Measurement of the contact angle hysteresis using filling method during a) water injection for advancing contact angle (θ_A), b) water depletion for receding contact angle (θ_R).

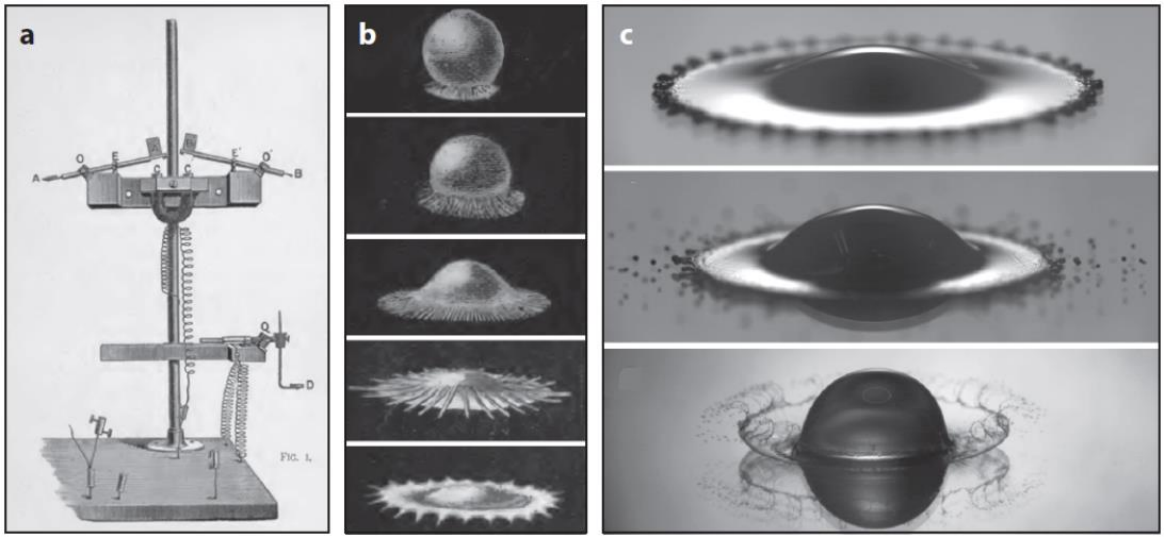

Figure 1-9: a) Worthington droplet dispensing unit, (b) Worthington's sketches from the impact of Mercury drop on a flat substrate. (c) Replication of Worthington impact condition captured by modern imaging technology [20].

1.2 Droplet Impact

Systematic study of droplet impact goes back to Worthington [21] in the 19th century by investigating the water droplet impact and splashing using a creative imaging process of his era (Figure 1-9). Impact of a droplet on a solid substrate is a key element of wide variety of phenomena which can lead to serious issues on many natural and engineering systems, such as inhibited data transfer for telecommunication systems [22], corrosion of structures exposed to the elements [23], absorption of water into porous building material [24], inkjet printing [25], rapid prototyping [26], microfabrication [27], paint spraying [28]. In addition, the effect of heat transfer associated with the impact is helpful on designing efficient spray cooling systems [29], fabrication of ice-free surfaces to eliminate undesired ice accretion and maintaining the aerodynamic performance of airplanes [30]. Dispersal of seed and microorganisms [31] and pesticide spraying in agriculture [32], internal combustion engines with direct fuel injection [33] where the fuel is sprayed into

engine cylinders in the form of small droplets, are some practical applications of this area. Despite the necessity of knowledge in this field, the underlying rapid dynamic of droplet impact process eluded explanation until the past 25 years, when high-speed video technology began to allow time-resolved imaging of the phenomenon [34]. As a result, plenty of discoveries on droplet behavior, several unresolved issues are yet to be addressed.

In the scenario of droplet impact on the smooth surface, various driving and dissipating mechanisms are involved that depends on several parameters. Research studies have been directed toward comprehending the relation between these parameters and its outcome including the accumulation and repellency of the liquid [35]–[37]. These outcomes primarily depend on the impact velocity, size of the droplet, liquid viscosity and surface tension [38]–[46]. The outcomes of the impact process are best studied using relevant dimensionless numbers, such as Reynolds and Weber numbers,

$$We = \frac{\rho D V^2}{\sigma}, \tag{1-4}$$

$$Re = \frac{\rho D V}{\mu} \tag{1-5}$$

Rioboo et al.[36], studied the impact of a millimeter size droplet on superhydrophobic and hydrophilic surfaces for a broad range of impact velocities, and categorized different outcomes based on the Weber number. Examples of the various impact outcomes are illustrated in Figure 1-10. These included deposition, splashing, and rebounding. The deposition occurs when a droplet is placed on a surface with very small Weber numbers ($We \ll 1$), and after slight deformation it reaches to an equilibrium state. When a droplet with small and moderate Weber numbers ($1 < We < 100$) impacts on a superhydrophobic surface, it completely rebounds off the surface. As the

Weber number increases to values above 100, splashing may encounter where small droplets detach from the peripheral edge of the spreading rim.

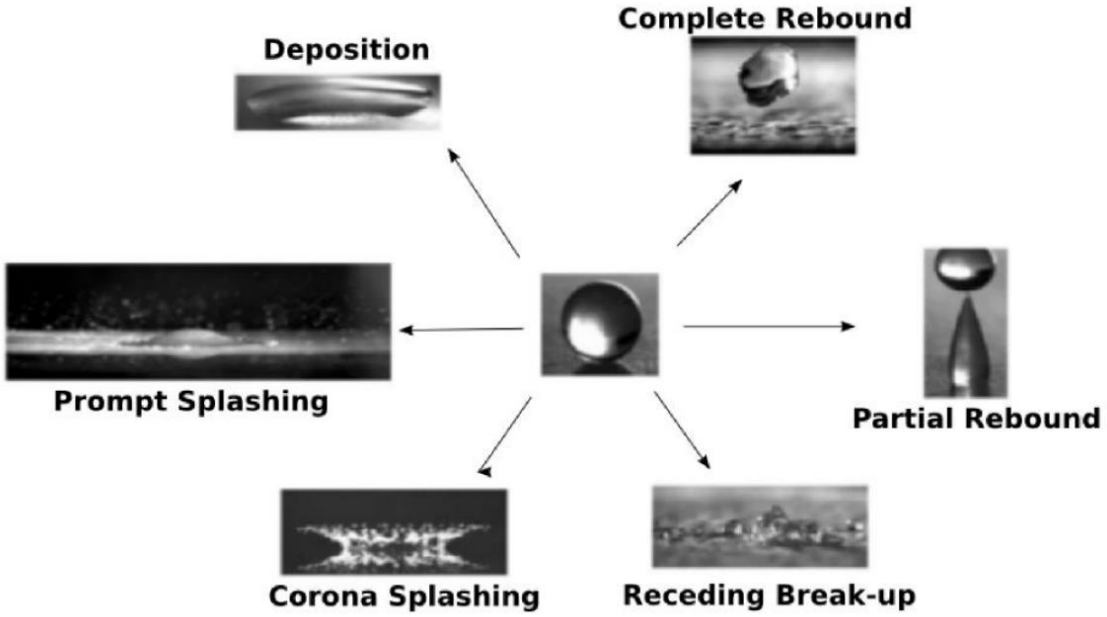

Figure 1-10: The various outcomes of droplet impact on solid surface [36]

Unlike a sessile droplet that its wetting states can be determined by measuring the contact angles, and compare them to that obtained from equilibrium Cassie and Wenzel states, for the scenario of a droplet impact, the situation is slightly different, since the outcome may depend on the balance of pressures in the system. Deng et al. [47], proposed a simple pressure balance model that explains the transition from Cassie to equilibrium Wenzel wetting during the impact on a superhydrophobic surface composed of micro-arrayed pillars with squared cross-sectional pillars. According to their model, wetting state depends on two wetting pressures; 1) water hammer pressure (P_{WH}) and dynamic pressures (P_D), 2) an antiwetting pressure, capillary pressure (P_C), which defined as follow;

$$P_{WH} = 0.2\,\rho CV \tag{1-6}$$

$$P_D = 0.5\,\rho V^2 \tag{1-7}$$

$$P_C = \left(\frac{-4\cos\theta_p}{\left(1+\frac{s}{2w}\right)-1}\right)\frac{\sigma_{LG}}{2w} \tag{1-8}$$

where C is the speed of sound, w and s are the surface features dimensions corresponding to the width and spacing of the pillar pattern.

According to their model, the outcome of impact was categorized as follows,

$$\begin{cases} P_C < P_D < P_{WH} \\ P_D < P_C < P_{WH} \\ P_D < P_{WH} < P_C \end{cases} \Rightarrow \begin{matrix} complete\ infiltration \\ partial\ pinning \\ complete\ recoil \end{matrix}$$

Above measurement was performed based on the impact of a millimeter size droplet on a microstructured surface.

Depending on the topography of the surface, different amount of energy dissipates during the impact. There were some models proposed to determine the amount of energy dissipates from droplet during the impact on a solid surface. Chandra and Avedisian [44] proposed a model in which the dissipated energy was assumed to equate the work done. This model suggested a pancake thickness to represent droplet boundary layer, where a linear velocity distribution across the entire thickness of the droplet was assumed. In addition, the time was simply the ratio between droplet size and its velocity. Pasandideh-Fard et al., [48] proposed a model based on the balance of energy. They used the maximum contact angle, which is the droplet's contact angle at maximum spreading, just as the contact line becomes stationary. In their analysis, it was emphasized that most of the viscous dissipation occurs in the thin boundary layer that is found on the substrate upon which the impact occurs.

Numerical modelling of droplet dynamic belongs to the class of two-phase interfacial problems. With the growing computational capabilities and the development of new numerical techniques, the simulation of droplet impact has become possible. One of the fundamental problems is the numerical description of the two-phase flow. There are different methods for simulation of interfacial flow problems, such as; Volume of Fluid method (VOF), Level-Set method (LS), Phase Field method (PF), etc. In this thesis, we focused on the VOF method because of several reasons; 1) capablity of handling high interface distortion, 2) possibility to extend the model to 3D, 3) capability of handling unstructured mesh and adaptive mesh refinement, and 4) capability of conserving mass at sharp curvatures. In VOF, the motion of the interface is not tracked, but rather the volume of each material (liquid or gas) in each cell is evolved in time that is why sometimes it has been called volume tracking method [49]. A historical review of VOF method can be found in [50], [51].

Harlow and Shannon [52] were the first to simulate droplet impact on a solid surface, shallow pool and deep pool using Marker-and-Cell technique. Their 2D model was a simple study of a droplet impact without considering the effect of the surface tension force. Some of the physics associated with the hydrodynamics of the impact such as recoiling, thin film formation, etc. was neglected in their study. Nevertheless, they are known as the pioneer of this subject. Tsurutani et al. [53] added the effect of surface tension into the model and were able to capture the hydrodynamic during the recoiling stage. Consequently, the transformation of kinetic energy to surface energy and vice versa was captured. Mehdi-Nejad et al. [54] simulated the impact of various size liquid droplets on the dry solid surface using a modified Volume of Fluid method. They were able to capture the entrapped air bubbles at the solid surface upon impact. A detailed review of this progression can be found in [55].

There are cases where stochastic analysis of train drops and their impingement on a solid surface or liquid film become a fascinating field of research. For instant, accumulation of water layers as the result of raindrops occurs naturally. This accumulation starts by the impact of a single droplet on a dry surface and is followed by the coalescence of several other droplets in a row on liquid film or solid surface. In some applications, accumulation of water is not favorable. These negative consequences are elevated when freezing conditions exist, and the threat of icing is involved. For instant, the buildup of ice on power lines [56]–[58], or accretion of the ice layers on the structure of an aircraft causes change in the lift, drag, weight of the aircraft, and threaten the safety of the airplane and passengers [59], [60]. To avoid these hazards, researchers potentially have been seeking ways to prevent undesired accumulation of water layers as the result of cloud-sized droplets (typically in size range of 20 μm) impact, nevertheless, understanding the mechanism of droplet solidification (freezing) is of the utmost importance.

Droplet Solidification

Solidification or freezing, is a phase change process in which liquid turns to solid when its temperature is lowered below freezing point. Regarding freezing phenomena, abundant theoretical [61], experimental [62] and numerical [63], [64] studies were carried out. In fact, a combination of heat transfer knowledge along with phase change mechanism (i.e., solidification) is necessary for prediction of droplet solidification.

The pioneering work in the modelling of phase change was the classical Stefan problem [65], the model which accounted for isothermal solidification in a multi-domain. Eventually Stefan model has become a bench mark solution for modelling of material phase change. His model is a particular kind of the boundary value problem for a partial differential equation (heat conduction),

adapted to the case in which a phase boundary can move with time (i.e., freezing line). Phase change process occurs over a region called mushy region which is bounded by solidus temperature (T_s) and liquid temperature (T_l) as shown in Figure 1-11. The mushy zone thickness may vary depending on thermal properties of the material undergoing phase transition. This behavior has been quantified using the ratio of latent heat to sensible heat (Stefan number). For instant in water, this ratio is about an order of magnitude greater than metals. This means that the discontinuity at the phase front for water is much more server. Therefore, using one-way (or weak solution) for modelling of water freezing results in poor calculation of the latent heat that releases during the phase change. Because of these difficulties, most of the research in the literature was dedicated to modelling of molten metal droplets solidification [66], [67]. Even with that, the integration between the free surface deformation and solidification has often been over-simplified.

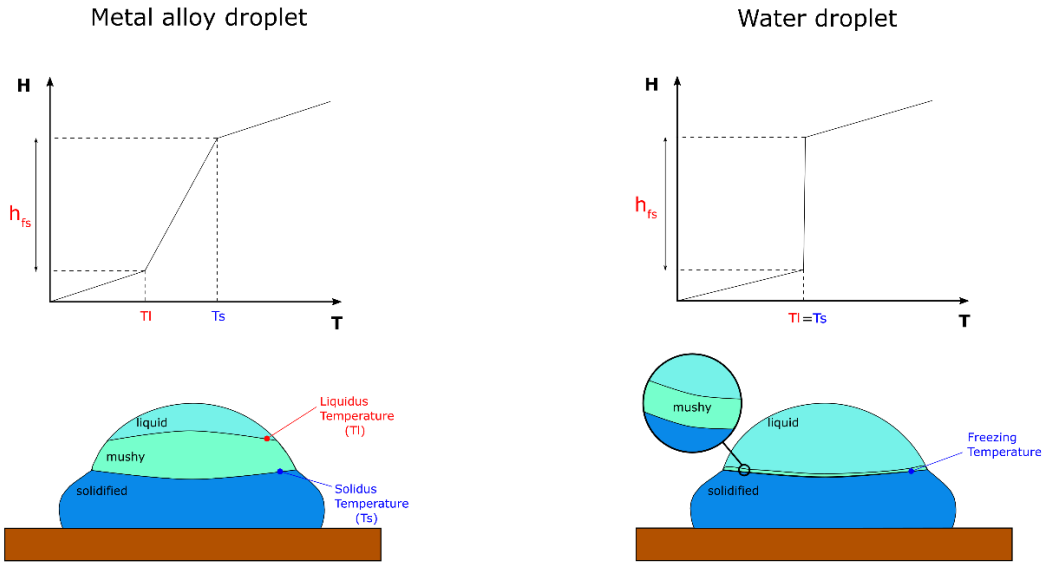

Figure 1-11: Schematic of a droplet solidification; in the left, metal droplet, and in the right, water droplet.

Several groups have employed VOF algorithm to model the impact and solidification of the liquid droplet [68]. Passandideh-Fard et al. [63] simulated the impact and solidification of the tin droplets

on a cold stainless steel substrate based on a modified SOLA-VOF method developed by Bussmann et al. [69]. He used the enthalpy transforming model of Cao et al. [70] to convert energy equation to have only one dependent variable (i.e., enthalpy), instead of two variables (enthalpy, and temperature). Although wall contact resistance varies with respect to time and position, they used a constant contact resistance in their model. Liu et al. [71], [72] studied the splat formation and solidification process using a VOF-based package, RIPPLE [68]. They also neglected the influence of the wall contact resistance in their model. Tong and Holt [7] used the enthalpy-porosity approach in studying a single copper droplet deposition on a substrate by numerically solving the complete energy equation inclusive of convection terms. The isothermal solidification front was approximated as an infinitesimally small artificial mushy region. Chung and Rangel [73] developed a numerical model to simulate the droplet deposition and solidification. They included the wall contact resistance based on a one-dimensional approximation. Zhang et al.[74] integrated a VOF-based solver with solidification process to study the substrate melting and solidification. However, the influence of melt convective in his model was neglected.

There are some studies which quantitatively determined the maximum spreading diameter of the solidified droplet (splat). Madejeski is known as the pioneer of this work [67] by assuming that thickness of the spreading lamella just varies with time and not space and droplet gets a cylindrical shape at the maximum spreading diameter. By proposing some approximations, the maximum spreading factor of the splat is demonstrated by,

$$\xi_{max} = 1.53K^{-0.395} \tag{1-9}$$

In addition, Passandideh-Fard et al. [66] presented another predictive model on spreading diameter with consideration of phase change,

$$\xi_{max} = \frac{D_{max}}{D} = \sqrt{\frac{We + 12}{\frac{3}{8}We + 3(1 - \cos\theta_{adv}) + 4\frac{We}{\sqrt{Re}}}} \quad (1\text{-}10)$$

This model which is based on the balance of energies incorporates another term of viscous dissipation along with conventional term in hydrodynamics model. It was assumed all kinetic energy is lost in the solidified ice layer thickness. However, they assumed that heat conduction is one-dimensional, the substrate is isothermal, the thermal contact resistance is negligible, and the Stefan number is small, as well. Similar study was performed by Azizi et al. [75] assuming heat conduction is one dimensional with no thermal contact resistance at the solid-liquid interface,

$$\xi_{max} = \frac{D_{max}}{D} = \sqrt{\frac{We + 12}{We\ Ste\sqrt{\frac{3\varepsilon_{substrate}^2}{2\pi Pe\varepsilon_{drop}^2}} + 3(1 - \cos\theta_{adv}) + 4\frac{We}{\sqrt{Re}}}} \quad (1\text{-}11)$$

where Ste is the dimensionless Stefan number, which is the ratio of sensible heat to the latent heat ($Ste = \frac{C_{pl}(T_m - T_s)}{H_f}$), and is directly related to the degree of subcooling (i.e., difference between substrate temperature and melting point temperature of liquid droplet ($T_m - T_s$)), Pe is the Peclet number ($Pe = VD/\alpha_w$), and ε^2, is the effusivity function ($\varepsilon = k\rho C_p$) . It was shown that if square root of Stefan number to Prandtl number ($Pr = \nu/\alpha$) becomes much smaller than one, the effect of solidified ice layer on the maximum spreading diameter is negligible. However, all these predictive models of the maximum spreading diameter slightly over-estimate the maximum spreading diameter because of the fact that thermal contact resistance were not taken into account.

Supercooling effect is referred to the situation when the liquid temperature is below 0°C but still in liquid phase. This is because of many complicated reasons allowing water to remain in liquid form below freezing temperature. In general, supercooled water exists because it lacks the

ability to complete the nucleation process. Nucleation process is the first step in the formation of a new thermodynamic phase. It is defined to be the process that determines how long it takes for a new phase structure appears. Nucleation often found to be very sensitive to the impurities in the system. These impurities sometimes can be too small that can be seen with naked eye. Sometimes it is important to distinguish the nucleation by their types; Heterogenous nucleation which occurs on the surface (i.e., surface vibration, surface asperities, etc.), and Homogenous nucleation that happens away from the substrate (i.e., condensation of gas-vapor, bubble formation, etc.), and is less common comparing with the heterogenous nucleation. Nevertheless, classical nucleation theory is the most common theoretical model used to understand why nucleation may take hours or years or sometimes it does not even happen, and it will be discussed later in this chapter.

When supercooled water freezes, latent heat is released suddenly. This means that if a whole droplet were to freeze instantaneously, the latent heat liberated would, unless the initial temperature below $-80^{\circ}\mathrm{C}$, raise the temperature of the droplet above $0^{\circ}\mathrm{C}$ which would be contradictory since ice cannot exist above $0^{\circ}\mathrm{C}$. In fact, only a small portion of the droplet freezes instantaneously, not more than enough to raise the temperature above $0^{\circ}\mathrm{C}$. Further progressive freezing takes place as the droplet loses heat by evaporation and conduction to the substrate [76].

The freezing mechanism of the supercooled droplet is still not fully understood. However, it is known that the entire process of freezing occurs in two stages [77]–[79]; 1) During the first phase, the supercooled liquid departs from the thermodynamically metastable state along with rapid growth of ice dendrites, resulting in a mixture of the liquid-solid at the melting temperature, which is referred to as the "recalescence phase", (Figure 1-12, A to B), 2) During the second stage, the remaining liquid in the solid-liquid mixture solidifies in a thermodynamically stable state at the

melting temperature, and the temperature gradually drops to the surface temperature (Figure 1-12, B-F).

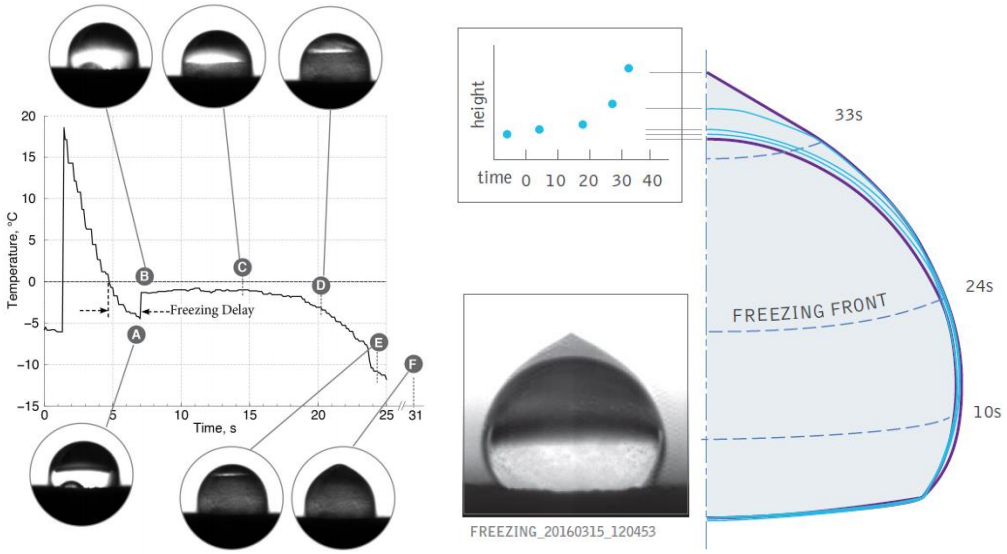

Figure 1-12: Freezing mechanism of the supercooled water droplet; the first abrupt freezing stage is observed between points A and B. Second stage of freezing continues after point B through F. Point B is expected to be close to 0°C [80].

In the case of cloud particles, the phase change process (heterogeneous nucleation) is initiated by the impact of the liquid droplet on a cold substrate (i.e., aircraft components). Some studies theoretically found temperature distribution of the formed ice based on the solution of transient conduction equation [81], [82]. However, there is no predictive model of maximum spreading diameter for supercooled water droplet except the model of Bahadur et al.[83] which was recently developed. Bahadur's model is through a combination of classical nucleation theory and droplet wetting dynamics. Bahadur's model is derived based on the three assumptions. First, droplet pinning occurs at the recoiling stage and the effect of phase change during spreading stage. Second, it was assumed the droplet spreads on the superhydrophobic substrate as a mass-spring model which was first shown by Okumura et al. [84]. Third, it has been demonstrated that hydrophobicity

of the surface breaks down by the growth of hemispherical ice cap underneath the impacting droplet.

The phenomena of supercooled droplet icing can be further elaborated through classical ice nucleation theory combined with thermal transport analysis based on the Gibbs free surface energy presented by Mishchenko et al. [62], and further discussed by Mohammadi et al. [85]. The nucleation rate [86], [87] can be related to the multiplication of kinetic rate (i.e., the activation energy of diffusion) with the exponential function of Gibbs free surface energy and interface temperature of an impacting water droplet on the substrate along with solid-liquid interfacial area and Boltzmann constant. According to the classical nucleation theory, the rate of nucleation under supercooled condition can be expressed through the critical Gibbs free energy as follows,

$$J = N_c \exp\left[-\Delta G^* / k_B T\right] = \frac{dv_s}{dt} \tag{1-12}$$

where J is the nucleation rate, k_B is the Boltzmann constant, prefactor N_c corresponds to kinetic coefficient for nucleation, k_B is the Boltzmann constant, and ΔG^* the critical Gibbs free energy under heterogenous supercooling freezing condition is given by,

$$\Delta G^* = \frac{16\pi \gamma_{SL}^{\ 3} T_m^{\ 2}}{3L^2 \Delta T^2} S(\theta_E) \tag{1-13}$$

where $S(\theta_E)$, is the geometrical factor and is defined as,

$$S(\theta_E) = \left[\frac{(2+\cos\theta_E)(1-\cos\theta_E)^2}{4}\right] \tag{1-14}$$

T_m is the water melting temperature and γ_{LS} is the ice water interfacial energy. The greater the supercooling $\Delta T = T_m - T$, the smaller the critical radius and the energy required to initiate the nucleation.

Jung et al. [64] formulated a modification to the classical heterogeneous nucleation theory, which predicts the observed freezing delay trends based on entropy reduction of water near a solid surface. It was obtained that surfaces with nanometer-scale roughness and higher wettability show unexpectedly long freezing delays comparing to the typical superhydrophobic surfaces with larger hierarchical roughness and low wettability.

On a dry surface, the spreading of the droplet is barely affected by the temperature of the substrate before nucleation occurs. The slight changes are because of the change of viscosity at lower temperature [88]. Hence, the vast body of literature addressing the dynamics of a liquid droplet impact onto dry surfaces [20], [89]–[91], and yet not discussed the impact on wet surfaces.

Yang et al. [92] performed an experimental investigation of the process of the supercooled water droplet impinging on dry cylindrical metal surfaces in different atmosphere temperature. They identified two main morphological characteristics of instantaneous and noninstantaneous freezing. The temperatures of the ambient air, the surface of the metal substrate, and the impinging supercooled droplet are the most critical parameters affecting the freezing patterns. They observed that the higher is the droplet impact velocity, the easier the freezing occurs. However, the influence of the impact velocity on freezing may be reduced by lowering the heat conduction of metal substrate.

Li et al. [93] performed an experimental study to identify the influence of solidification upon the impact process of a single water droplet on the aluminum surface with temperature ranges 20 °C to -13 °C. It was found that solidification does not influence the impact process during the first spreading phase while it suppressed receding significantly for lower impact velocities.

Mishchenko [63] performed an experimental study of the droplet impact and freezing on structured surfaces. They showed that an excellent superhydrophobic surface could remain entirely

ice-free down upto −30 °C. This is because of the ability of the surface to repel impacting water droplets before ice nucleation starts. In addition, they addressed factors contributing to droplet retraction, pinning and freezing by combining classical nucleation theory with heat transfer and wetting dynamics. They showed that the water droplets impinging on superhydrophobic surfaces exhibited a non-icing behavior if the time scale for droplet spreading and retracting from the surface was smaller than the ice nucleation time, and consequently the droplet would bounce or roll off the surface before nucleation occurs.

Maitra et al. [67] identified a complex role of viscosity for supercooled drop impact down to −17 °C on superhydrophobic micro-structured surfaces. They found that the increased viscous effect influences all stages of impact dynamics, in particular, the impact and meniscus impalement behavior, water retention by the textures (sticky versus rebounding drop) and possible icing. The results highlighted that at low temperatures, drop dynamics are affected by increasing of liquid viscosity caused by supercooling which led to a different mechanism of superhydrophobicity breakdown for supercooled drops.

In spite of all these studies, details of a droplet impact in the small-scale, under varied conditions are hardly known. The majority of studies of concurrent droplet impact and freezing have been performed using millimeter or sub-millimeter droplets [44]–[46], [94], [95], due to the ease of repeatability of large size droplets as well as obtaining different impact velocities due to the role of gravitational force on controlling the terminal velocity of impact. In this thesis, the impact of the micro-droplet on micro-structured superhydrophobic surfaces when the size of a droplet is comparable with the surface roughness under various conditions have been investigated.

Objectives

The main goal of the current study is to understand and identify the most influential parameters on hydrodynamic, heat transfer, and phase change of cloud-sized particles (micro-droplets) impinging on superhydrophobic surfaces having surface roughnesses comparable to the size of the droplets. Consequently, modifying these parameters, one can engineer a functional super/icephobic surface that repels water droplets before they freeze on the surface. To the best of author's knowledge, no study was carried out on the impact of cloud-sized droplets on superhydrophobic micro-structured surface when the size of the surface asperities is comparable with the size of the micro-droplet. All research in the literature neglect the importance of surface roughness on hydrodynamic of the micro-droplet. Specific objectives of this thesis are as follows,

- To understand the wetting behavior of micro-structured superhydrophobic surfaces by direct modelling of air pockets underneath the droplet and the surface morphology including micron/sub-micron features (roughness).
- To examine the influence of surface topography features (such as pillars width, height, and pitch) in determining the repellency and mobility of the surface, and consequently finding the optimum configuration for the least contact time.
- To examine the ice-phobic performance of the superhydrophobic surfaces through conjugate heat transfer modelling of the micro-droplet and the substrate during the impact.
- To derive a model to simulate the freezing of supercooled micro-droplet impacting on superhydrophobic surface.

1.3 Thesis Structure

This thesis is divided into seven chapters. The first chapter provides a brief introduction to the study of droplet-surface interaction, surface wettability, some relevant parameters that affect the wettability of a surface, droplet impact and different outcomes of the liquid droplet impact on a solid surface. A brief description of multiphase flow simulation and recent developments in the modelling of interfacial flow problems are pointed out. Finally, the motivation, research objectives and thesis structure are presented.

Chapter 2 presents a numerical and analytical study of cloud-sized droplets impacting on superhydrophobic surfaces. The droplet size and the impact velocity of the cloud particles in an in-flight condition was found to be 20 μm with 1.6 m/s (Appedix) on the surface, which has been used extensively in this study. The aim was to develop a numerical model that can capture the dynamics of the droplet on rough superhydrophobic surfaces. Consequently, using the computational tool we found the dependence of surface morphology to non-wetting property of the superhydrophobic surface with respect to change of the roughness features.

Chapter 3 presents a numerical study of coalescence induced-jumping of two identical micro-droplets on various micro-structured surfaces using the model developed in the previous chapter. The model was validated with the experimental data provided in the literature, and compared with other numerical models in the literature. Consequently, the threshold of relative roughness for which below that the smooth surface modelling of superhydrophobic surface is no more applicable was obtained.

Chapter 4 takes a further step toward modifying the model and adding the effect of conjugate heat transfer (between droplet and substrate) into the model. As a practical application, the model was used to evaluate the performance of superhydrophobic surfaces under practical spray cooling

process. Despite higher contact area between a droplet and a smooth hydrophilic surface, the heat transfer happened to be less comparing to that on a superhydrophobic surface. This was due to the better mixing of the liquid bulk in the peripheral rim of the droplet on the superhydrophobic surface.

Chapter 5 presents a detailed numerical analysis of the icephobic performance of superhydrophobic coatings. The solver has been further developed to include the phenomena of phase change into the model. A comparative study was performed to evaluate the icephobic property of superhydrophobic surfaces. the net effect of substrate thermal properties on transient heat conduction through the substrate was investigated by studying the impact of a droplet on two substrates with different thermal diffusivities. It was observed under similar conditions (i.e., wettability and surface morphology), the droplet was able to rebound on the surface with smaller thermal diffusivity.

Chapter 6 presents the numerical modelling of supercooled water droplet icing. The model is an approximation for a supercooled droplet of the recalescence step, assuming to be initiated by heterogeneous nucleation from the substrate. This is a modification of the model developed in Chapter 5 to calculate the latent heat release during the rapid freezing front based on the Gibbs free energy of the metastable droplet.

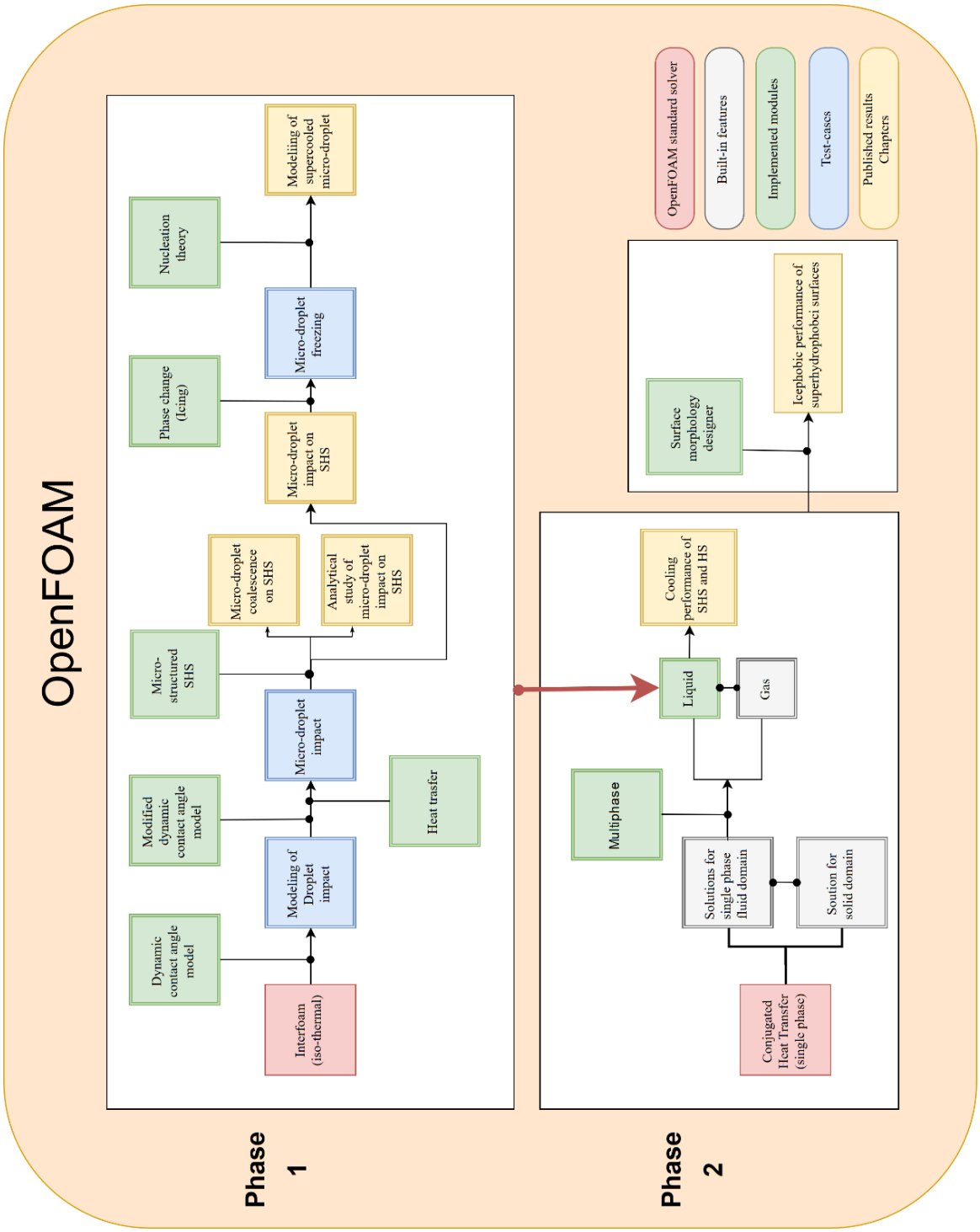

Figure 1-13: Schematic diagram of thesis structure.

Note that…

At realistic in-flight icing condition which mostly occurs during takeoff and landing at altitudes between 9000 to 20000 ft, aircraft faces the impact of droplets located on upper troposphere and cirrus clouds [87]. The standard speed of aircraft is measured to be around 60-150 m/s at the time of impact. These particles are very small, and their diameter is typically in the range of 1 µm to 500 µm, and are 10 to 1000 times smaller than rain drops. Smaller droplets have smaller inertia, and are more influenced by the airflow around the aircraft. However, smaller droplets tend to freeze faster and hence, the aircraft safety is more likely altered by the impact of small-sized cloud droplets. To determine the size and the terminal velocity of impact, a set of Discrete Phase Model (DPM) simulation was performed to model the cloud-sized particles (1-50 µm) toward a substrate with an average velocity of 90 m/s. It was found that the 20 µm droplet was the smallest cloud-sized particle which had the inertia to reach the surface of the airfoil. More interestingly, despite the high velocity of the aircraft, it was observed that all 20 µm cloud particles were impacting on the airfoil with the normal velocity of 1.4-1.6 m/s. Therefore, in order to replicate the most striking condition, the impact of a 20 µm micro-droplet with the impact velocity of 1.6 m/s were selected as the main focus of study. Furthermore, scales and dimensions of the superhydrophobic surface morphology presented in this thesis, are intended to be small enough to repel a 20 µm droplet and large enough to be able to fabricate with the current fabrication techniques.

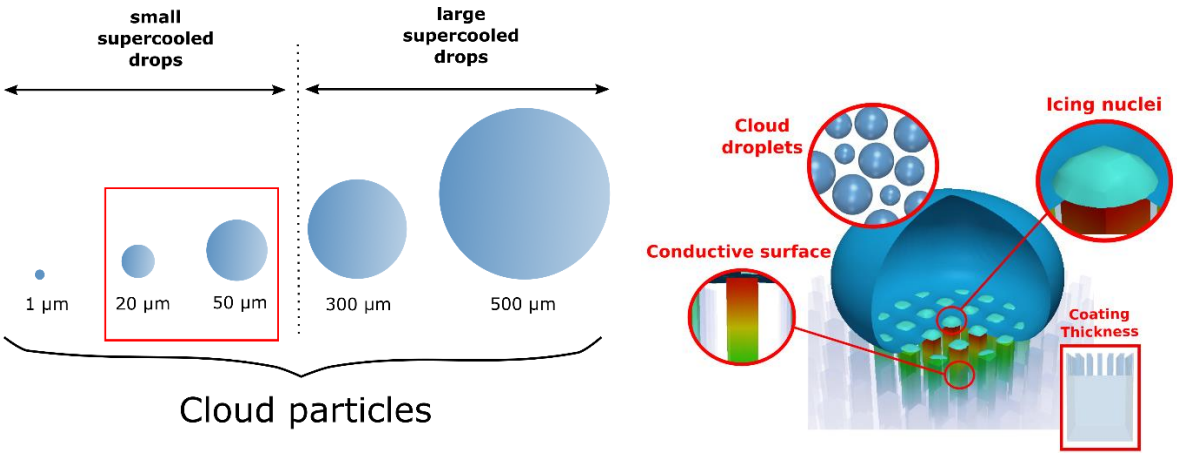

Figure 1-14: Size distribution of cloud particles (left), and superhydrophobic surface (right).

Chapter 2

Numerical Analysis of Micro-Droplet Dynamics on Superhydrophobic Surface

2.1 Abstract

Artificial ultra-hydrophobic and super-hydrophobic surfaces are typically fabricated by modifying the surface roughness of hydrophobic surfaces. These surfaces exhibit apparent contact angles greater than 150° degrees and very small hysteresis contact angle. In this paper, numerical modelling of roughness topography is performed through a series of microarrays to explore the direct effect of arrays and their post-spacing lengths on the micro-droplet penetration depth, restitution coefficient, as well as the maximum wetting diameter. The volume of fluid (VOF) method coupled with a dynamic contact angle model is used to model the impact of the micro-droplet. Two sets of simulations were performed in this study; first, a comparative study on a set of patterned surfaces with constant arrays width (W) but different pitch length (L), and second, pitch length was kept constant, while the arrays width were changed. To replicate a non-repellent hydrophobic surface, the intrinsic contact angle of 111° is applied to all surfaces. A droplet size of 20 μm is opted to simulate the impact of the cloud-sized particles with the impact velocity of 1.6 m/s. By direct modelling of the roughness topography along with an appropriate dynamic contact angle model, the simulation successfully captured the presence of air pockets underneath the micro-droplet inside micro-grooves. In addition to that, an analytical model was derived based on the concept of energy balance assuming disk-shape of the bulk in the maximum spreading phase.

As per results, maximum spreading length, penetration depth and detachment of droplet was captured using the numerical model, and they were found to be in good agreement with the data obtained from the analytical model.

2.2 Introduction

Surfaces with designed microscopic roughness possess remarkable non-wetting properties, and extensive attention is drawn recently by the micro and nanotechnology research communities [12], [96], [97] into the development of the materials, aiming at finding new ways of controlling solid surface-fluid interface properties. Although according to Young's equation, a flat surface with a contact angle approaching 180° could theoretically be possible, no physical evidence has been reported that demonstrates this situation. Theoretical models describing the influence of surface roughening concerning the wetting properties of the surface have been introduced earlier either following the (i) Wenzel [16], or (ii) Cassie-Baxter [17] models. In Wenzel model it is assumed that the liquid impales the roughness elements, and follows the surface topography, resulting in higher surface wettability due to the increase in contact area [16]:

$$\cos\theta_w = r\cos\theta_S \tag{2-1}$$

where r is the surface roughness or the ratio of the actual area of the solid/liquid interface to the normally projected area, while $\cos\theta_E$ is the equilibrium or static contact angle.

In the Cassie-Baxter model [17], air entrapped beneath the droplet inside the groove features form a composite hydrophobic surface, holding the droplet on the tip of the pillars and resulting in a larger contact angle,

$$\cos\theta_c = -1 + f(\cos\theta_S + 1) \quad (2\text{-}2)$$

where *f* is the solid-liquid fraction which is the ratio of the actual surface area over the projected surface area.

A large number of experiments and theoretical investigations on droplets-surface interaction have been reported. However, they are based on a smooth substrate with intrinsic contact angle [98], [99]. For very small size droplets (typically in the order of few microns), the outcome of the impact on a textured surface is different from that on a smooth surface, due to the impact force, the liquid penetrates the micro-cavities, and exhibits a different wetting scenario on a textured surface.

Deng et al. [47] discussed different types of pressures and wetting states experienced by the impacting droplets on the textured surface. However, as his experiment was conducted for droplet size of 1mm, there is no evidence indicating that the dynamic of droplet would be the same for micron size drops when the size of the droplet is almost comparable to the scale of the pillars. Unfortunately, due to some uncertain factors, such as penetration depth, the geometrical configuration of the recoiling droplet and the complicated viscous dissipation rate, a direct theoretical and experimental investigation of the bounding behavior of the droplet on a textured surface is difficult. Therefore, it is expected that the numerical simulation can overcome these difficulties and provide more detailed information regarding the effect of roughness topography on the dynamic of micro-droplet and the dissipated kinetic energy of a droplet during recoiling stage.

2.3 Methodology

2.3.1 Numerical Approach

The Navier Stokes equation expressing flow distribution of the liquid and the gas, coupled with the Volume of Fluid (VOF) method for tracking the interface between the liquid and the gas are solved numerically using finite volume methodology. In VOF model [100] tracking of the interface is modeled by solving continuity equation for one of the two phases in each computational cell at every time step. The governing equations for the mass and momentum balance in each fluid phase and on the interface can be expressed as,

$$\nabla \vec{V} = 0 \tag{2-3}$$

$$\frac{\partial \rho \vec{V}}{\partial t} + \nabla . \left(\rho \vec{V} \vec{V}\right) = -\nabla p + \nabla . \left(\mu . \nabla \vec{V}\right) + \left(\nabla \vec{V}\right) . \nabla \mu - g . x \nabla \rho + F_b \, , \tag{2-4}$$

where, t, is time, $\vec{V}$, is the velocity vector, F_b is the body force, and α is the volume fraction which is used to calculate the viscosity μ, and density ρ, as weighted averages based on the distribution of the liquid fraction,

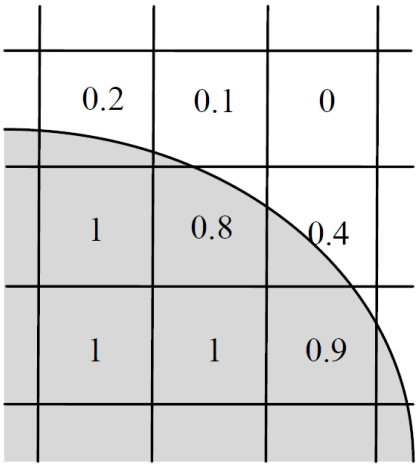

Figure 2-1: Schematic of VOF tracer in every computational cell

$$\rho = \alpha\rho_l + (1-\alpha)\rho_g, \tag{2-5}$$

$$\mu = \alpha\mu_l + (1-\alpha)\mu_g \tag{2-6}$$

where the subscripts l and g denote the liquid and gas phases, respectively. In VOF method the phase fraction scalers function α, admit values between 0 and 1, where α = 1 corresponds liquid phase, and α = 0 for gases, and $0 < \alpha < 1$ is where the interface is located. As the interface evolves with the motion of fluid, it is essential that α satisfies the conservation equation,

$$\frac{\partial\alpha}{\partial t} + (\vec{V}\nabla)\alpha + \nabla.\left(\vec{V}_r\alpha(1-\alpha)\right) = 0, \tag{2-7}$$

where $\vec{V}_r$ is the vector of relative velocity, designated as the compression velocity introduced by Rusche [101] to facilitate a sharp interface between phases,

$$\vec{V}_r = \vec{n}\max\left[Co\frac{|\emptyset|}{|S_f|}, \max\left(\frac{|\emptyset|}{|S_f|}\right)\right] \tag{2-8}$$

where $Co, n, \emptyset$ and S_f, are the compression coefficient, unit normal flux, face volume flux and cell face area vector respectively. The interface unit normal $\vec{n}$ is computed by taking the gradient of smoothed volume fraction α at the cell faces.

$$\vec{n} = \frac{\nabla\alpha}{|\nabla\alpha| + \delta}, \tag{2-9}$$

where δ is a small number in order to stabilize the calculation outside the transition region where $\nabla\alpha \to 0$. In this study, $\delta = 10^{-8}$ is used for the entire simulations. The main benefit of such formulation is in the possibility of capturing the sharp interface region. The continuum surface force method [69] is used to model surface tension as a body force F_b that acts only on interfacial cells,

$$\vec{F}_b = \sigma_d k \nabla \alpha, \tag{2-10}$$

where σ_d is the surface tension, and k is the mean curvature of the free surface, calculated by,

$$k = -\nabla . \left(\frac{\nabla \alpha}{|\nabla \alpha|} \right). \tag{2-11}$$

The pressure-Implicit with splitting operators (PISO) scheme in transient flow is used for the pressure-velocity coupling. The wettability effects at the substrate are taken into account by using the dynamic contact angle which is assumed to be a function of the contact line velocity. The Kistler's correlation [102] is used to calculate the dynamic contact angle in each time step,

$$\theta_d = f_H [Ca + f_H^{-1}(\theta_A , \theta_S, \theta_R)] , \tag{2-12}$$

where, f_H is the Hoffman's function and is defined as,

$$f_H = \cos^{-1} \left\{ 1 - 2 \tanh \left[5.16 \left[\frac{x}{1 + 1.31 x^{0.99}} \right]^{0.706} \right] \right\} . \tag{2-13}$$

in the above equation, the equilibrium contact angle θ_S is replaced by either the advancing contact angle, θ_A, or the receding contact angle, θ_R, depending on the direction of the velocity vector at the contact line or the static contact angle, θ_S, if the contact line velocity is zero. It is worth mentioning that the no-slip models such as Kistler's correlation [102] have been extensively used to investigate droplet dynamics [103], [104]. In addition, it was shown that this model is capable to capture the relevant physics of droplet-substrate interaction and provides good agreement with experiment.

2.3.2 Geometrical Configurations and Meshing

The computational domain size of 0.034 × 0.034 × 0.040 mm is used for the 3D simulation of the textured surface (Fig 2.1) with *W, L*, *H,* and *G* correspond to pillars width, the pitch between two adjacent pillars, the height of the pillars, and the spacing between pillars respectively.

A mesh independence test is performed for all textured models. The domain is discretized by about 3.3 million, 7.8 million, and 15.6 million hexahedral mesh with local refinement beneath the droplet and the interfacial cells. As the change of interface evolution in 7.8 million and 15.6 million mesh was minimal, the domain composed of 7.8 million mesh is applied for this study. The cells are refined so to have 120 cells per diameter of the droplet before impingement. Two sets of studies were conducted. i) the effect of pillars width on hydrodynamic of the micro-droplet ii) the effect of surface pattern pitch on hydrodynamic of the micro-droplet.

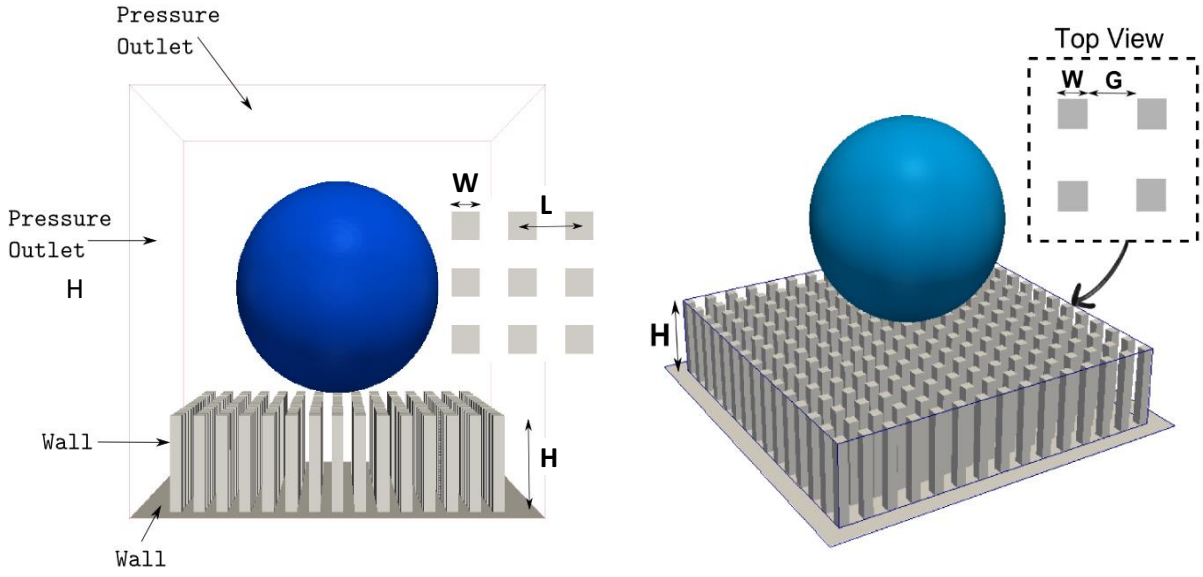

Figure 2-2: 3D computational domain, droplet, and textured surface

2.4 Mathematical Model

The mathematical model is based on the mass-energy balance before impact and at the instant of maximum spreading diameter,

$$E_{K,1} + E_{S,1} = E_{K,2} + E_{S,2} + \Phi_1 + \Phi_2 \tag{2-14}$$

where $E_{K,1}, E_{S,1}$ are the kinetic and surface energies of droplet before impact, $E_{K,2}, E_{S,2}$, are the kinetic and surface energies of droplet at the instant of maximum spreading diameter, and $\Phi_1 + \Phi_2$, are the total viscous dissipation composed of the dissipation due to the contact of the liquid droplet with the pillars head, and the pillars side walls;

$$E_{k,1} = \frac{\pi}{12}\rho D_0^3 V^2 \tag{2-15}$$

$$E_{s,1} = \pi D_0^2 \gamma \tag{2-16}$$

$$E_{K,2} = 0 \tag{2-17}$$

The total surface energy in the maximum spreading stage ($E_{S,2}$) is constructed from the liquid-gas, solid-liquid and solid-gas surface energies. Using disc shape assumption of micro-droplet in the maximum spreading phase, the liquid gas energy can be approximated as the summation of the top area of the disk, disk side walls, and the area penetrated between the pillars forming a spherical cap shown in Figure 2-3,

$$\text{Top surface energy} \approx \frac{\pi}{4} D_m^2 \sigma_{LG} \tag{2-18}$$

$$\text{Sidewall energy} \approx \pi D_m \sigma_{LG} H_1 \tag{2-19}$$

$$\text{Bottom/penetrated spherical cap energy} \approx 2\pi R_L H_2 (1 - f_s)\sigma_{LG} \tag{2-20}$$

Where σ_{LG} is the surface tension, D_m is the maximum spreading diameter, R_L, is the radius of curvature which can be approximated as $0.5D_c/\cos\alpha$, and f_s is the solid fraction (A_{solid}/A_{cell}).

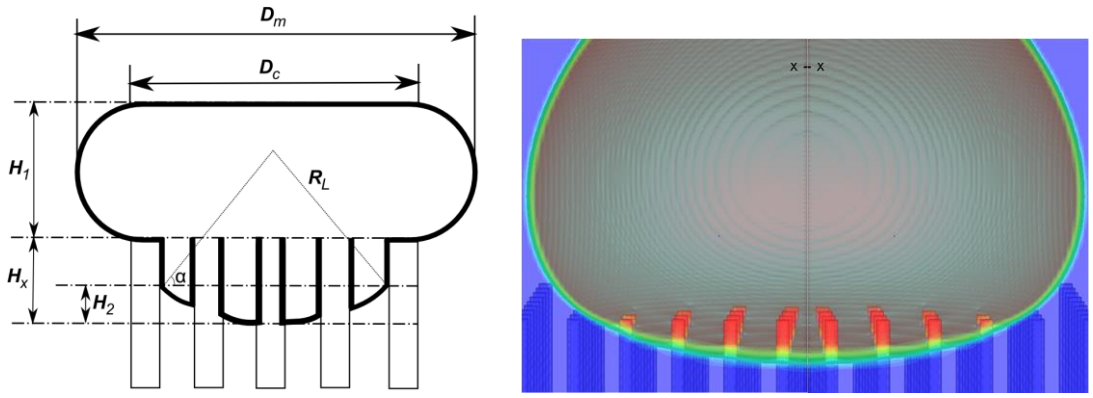

Figure 2-3: Schematic presentation of penetrated droplet interface during the spreading stage.

$$\Pi = \frac{WL(H_x - H_2)}{L^2} \tag{2-21}$$

$$\Lambda = \frac{WLH_2}{L^2} \tag{2-22}$$

$$k = \frac{2\pi R_L H_2}{\pi D_c H_2 + \frac{\pi}{4} D_c^2} \tag{2-23}$$

where Π, Λ, k are the coefficients to find the solid-liquid contact area, and H_x is the penetration depth. The liquid-gas surface energy penetrated inside the pillars can be determined as follows,

$$E_{SL} = \frac{\pi}{4} D_c^2 (f_s + \Pi + k.\Lambda)(\sigma_{SL} + \sigma_{SG}) \tag{2-24}$$

In addition, penetration depth can be approximated using Hagen-Poiseuille's law [105], [106] as follows,

$$H_x = \sqrt{\left(P_{wetting} - P_{antiwetting}\right).\frac{\overline{dx}^2}{32\mu}\frac{D_0}{V}} \tag{2-25}$$

where the dynamic pressure (P_D) and water hammer pressure (P_{WH}) are the wetting pressures, whereas capillary pressure (P_C)[107], the anti-wetting pressure,

$$P_{water\ Hammer} = 0.2\rho CV \tag{2-26}$$

$$P_{dynamic} = \frac{1}{2} m \vartheta^2 \tag{2-27}$$

$$P_{capilary} = \left(\frac{-4 \cos \theta_a}{\left(1 + \frac{L}{W}\right) - 1} \right) \frac{\sigma_{LG}}{W} \tag{2-28}$$

The viscous dissipation due to contact of the liquid drop with the pillars head is approximated using the model of Passandideh-Fard [48] as follow,

$$\Phi_1 = \frac{\pi}{8} \mu V D_m^2 \sqrt{Re} \times f_s \tag{2-29}$$

In addition to that, the viscous dissipation as the result of penetrated liquid in contact with side walls can be approximated by Ishino's model,

$$\Phi_2 = \frac{\pi^2 \mu V D_C^4}{6[ln(P/L)] D_0} \frac{H}{L^2} \tag{2-30}$$

2.5 Results and Discussion

All simulations are resembling the impact scenario of the micro-droplet (20 μm) initialized slightly above the surface with an initial velocity of 1.6 m/s. Since the Bond number (i.e., the ratio of gravitational force to surface force) is much smaller than the critical Bond number, gravity has been neglected in this study. The dominant forces controlling hydrodynamic of the micro-droplet penetration into the micro-cavities are the viscous and interfacial forces, which are included in the capillary number and continuum surface force models [69].

2.5.1 Comparison with Mathematical Model

A three-dimensional numerical and analytical model validation of the micro-droplet hydrodynamics on textured superhydrophobic surface was carried out. Impact of the micro-droplet

onto a textured surface composed of squared-textures and square patterns with 1 μm pillars width and varying spacing length was examined. The dependence of the maximum spreading factor (i.e., the ratio of the maximum spreading length to the maximum contact length) to the change of spacing factor (width to spacing ratio) in a partially penetrated state obtained from the two models were compared. From Figure 2-4, it is apparent that the data obtained from the two models are reasonably in close agreement in finding the optimum spreading factor. The single most striking observation to emerge from comparing these two graphs was that both models reported the least spreading factor occurs at a width to spacing legth of 1.5. In other words, for the current configuration, width to spacing length of 1.5 signifies the optimum non-wetting behaviour of the surface. From this point, a similar ascending trend for smaller and larger spacing lengths were observed. When the ratio of spacing factor increases or decreases, the micro-droplet forms a spherical cap as opposed to a spherical shape at the width to spacing of 1.5. comparing two graphs at width to spreading 1.5 and beyond, it has been observed that both graphs diverge at with to spreading length of 2 and then they start converging for the second time. This can be due to the number of assumptions used in the analytical model including the use of Hagen Peuossille equation which is was defined for the flow inside a pipe and the simple disc shape assumption of the droplet in the maximum spreading stage which is no more valid as the width to spacing ratio increases. However, the present results provide evidence that the simulation could adequately predict the hydrodynamic (spreading factor) of the impinging droplet on the micro-structured superhydrophobic surface, hence it can be used as a tool to simulate the micro-droplet impact under varied conditions on a textured surface.

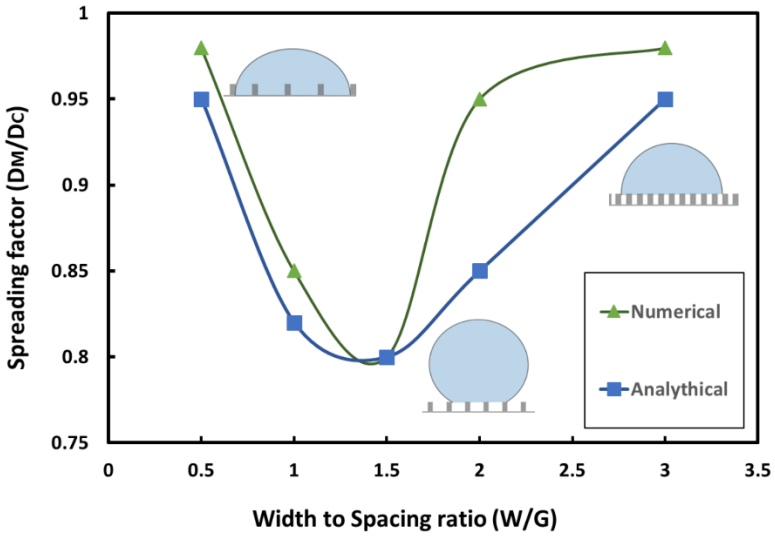

Figure 2-4: Spreading factor vs. width to spacing ratio of the surfaces of constant arrays width.

2.5.2 Effect of pillars width on droplet hydrodynamics

The effect of pillars width was examined by considering the impact the micro-droplet onto a series of pillars with varying width size within constant pattern pitch (the distance between two adjacent pillars) in the atmospheric condition. Figure 2-5 illustrates the time-lapse sequence of the droplet impingement on a (a) smooth substrate, (b) textured surface with pillars width of 0.5 µm, and (c) textured surface with pillars width of 1 µm, respectively. As shown in Figure 2-5.a the droplet does not rebound on the substrate (with no physical roughness) likely because of the large area in contact with the droplet results in higher dissipation of the kinetic energy. However, depending on the topographical configuration of the textures (physical roughness) shown in Figure 2-5.b and Figure 2-5.c, detachment was captured on these surfaces. It was revealed that the solid fraction (roughness) in contact with the micro-droplet has a considerable influence on the penetration depth of the micro-droplet and this behavior was captured using the current model. In these simulations, since the pitch length (L) was kept constant, the pitch effect on hydrodynamic of the droplet, as an important parameter is not individually evaluated. Figure 2-5.b shows the larger spacing between

the arrays, allow the droplet to penetrate easier into the valleys, and due to the effect of surface tension, the penetrated volume tends to form a spherical cap.

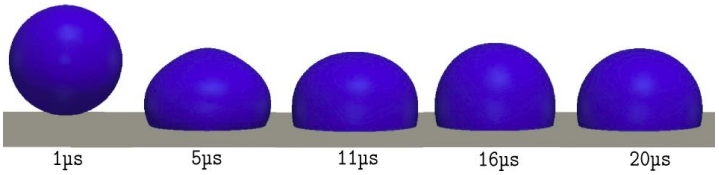

(a)

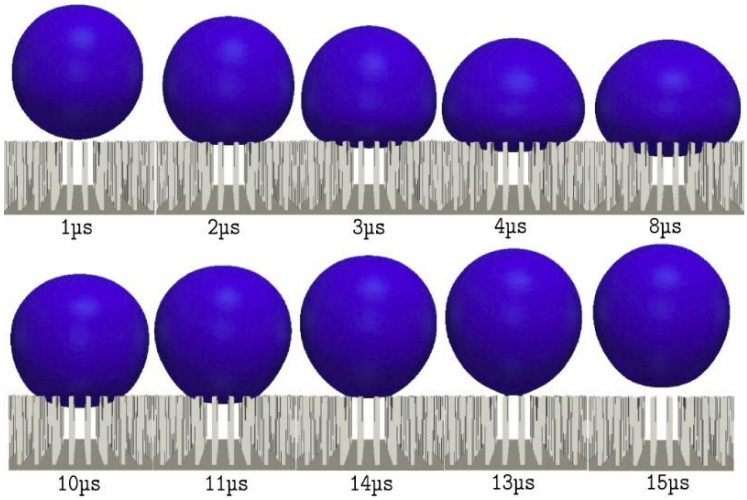

(b)

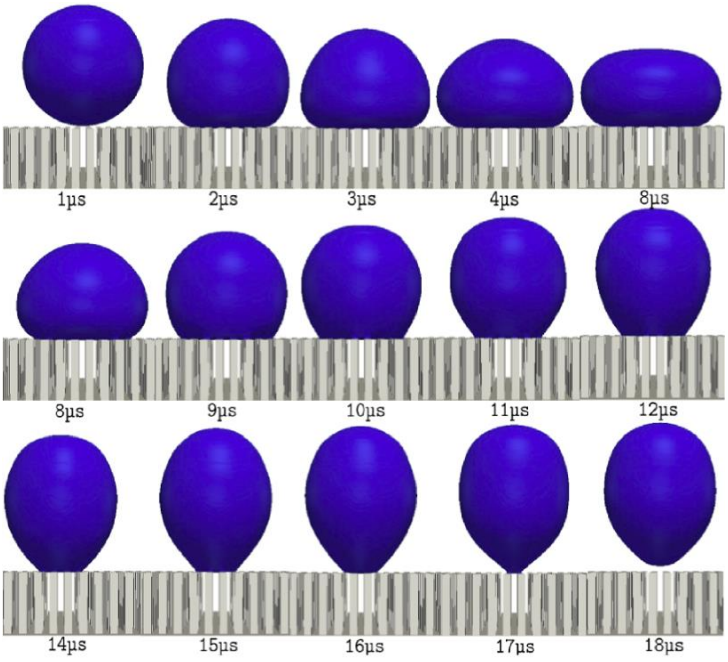

(c)

Figure 2-5: Micro-droplet impact on a) smooth surface, b) textured surface with $L = 2\mu m$, $W = 0.5\mu m$ and c) textured surface with $L = 2\mu m$, $W = 1\mu m$, all having the intrinsic contact angle of 111°.

Figure 2-6 provides a quantitative comparison between the microdroplets spreading factor, as a function of time. It shows that droplet impingmement on the surface with the least pillar width (W) significantly affect droplet dynamics regarding both the spreading diameter and the contact time. Increasing the projected solid fraction by two times results in reducing contact time about 20%, and the maximum spreading diameter approximately increases by 15%. Due to the smaller projected solid fraction in Figure 2-5.b, the droplet bounces off before it penetrates the surface roughness. It can be concluded that smaller solid fraction, induces higher penetration depth of the droplet, as well as the higher wetting area of the surface.

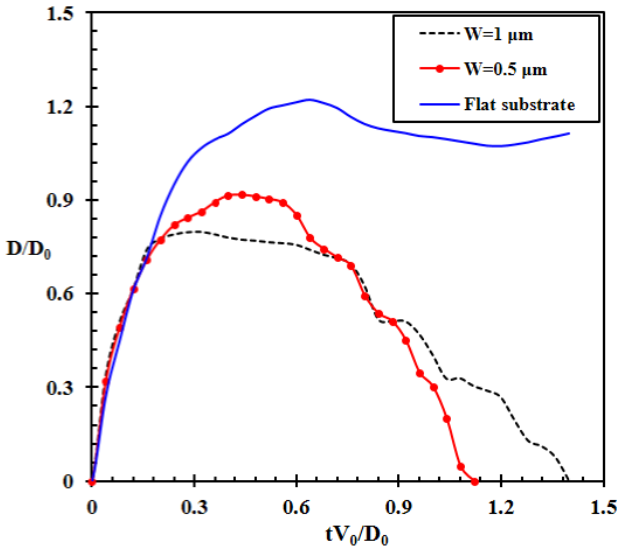

Figure 2-6: Numerical results of the 20 µm microdroplet spreading factor evolution at 1.6 m/s on both smooth and textured surfaces θ_e=111°.

2.5.3 Effect of pitch length on droplet hydrodynamics

The simulation time and the spreading diameter are normalized and non-dimensionalized with inertia and the diameter of the micro-droplet. Figure 2-8 shows the numerical results for microdroplet spreading factor (D/D_0) with respect to dimensionless time (tV_0/D_0) onto different textured surfaces. Based on preliminary examination of the impact on the smooth surface (without physical roughness), the droplet did not rebound on the smooth hydrophobic surface. The same outcome is observed for the textured surface with pillars width (W) of 1 μm and post spacing length (G) of 0.5 μm, which resulted in higher spreading diameter. However, the droplet bounced off the surface by increasing the spacing between two pillars to 1 μm due to decreasing the solid area in contact with liquid droplet. The spreading diameter started decaying as the spacing length increases. However, this trend changes for surfaces with a spacing length of 2 μm and larger. For larger spacing length, the droplet penetrates between the micro-grooves, and a higher solid area comes in contact with the droplet. In addition, this can be justified with the smaller effect of capillary pressure which is known to have anti-wetting property in the system. Since capillary pressure is inversely proportional to the ratio of width to spacing length [107], therefore the droplet penetrates as the result of smaller capillary force to avoid penetration of the droplet along the pillars.

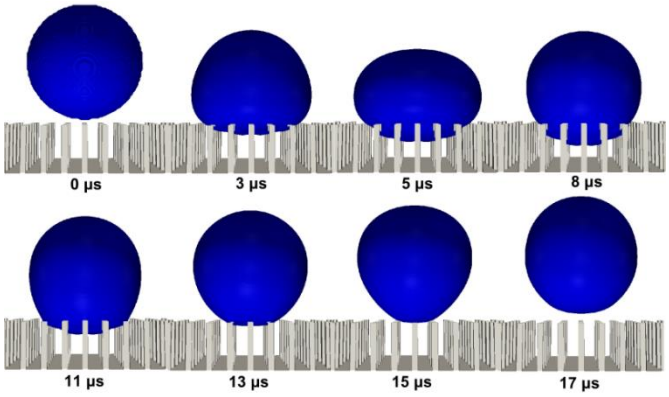

(a)

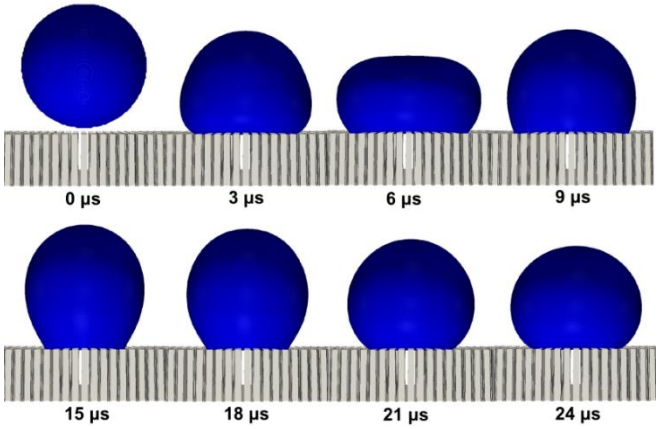

(b)

Figure 2-7: Micro-droplet impact on flat and textured surface with intrinsic contact angle 111°.

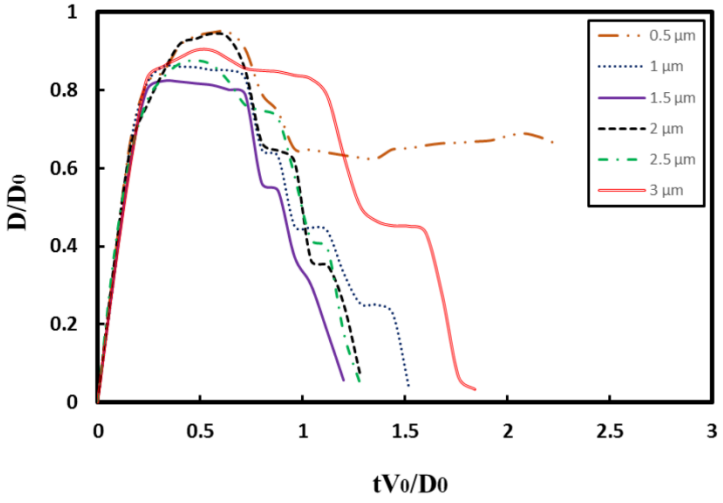

Figure 2-8: Spreading factor evolution of micro-droplet at 1.6 m/s impact velocity ($\theta_E = 111°$) for different spacing sizes.

2.5.4 Effect of Post-Spacing on droplet hydrodynamics

Restitution coefficient is calculated as the ratio of droplet jumping velocity to impact velocity (V_{juming}/V_0) which normally ranges from 0 to 1. This coefficient is always less than one due to the initial kinetic energy being lost by the viscous effect during spreading and recoiling phases. A

smaller restitution coefficient is the result of higher viscous effect and vice versa. Figure 2-9 shows the change of restitution coefficient based on different spacing length. The minimum dissipation of the Kinetic energy occurred on the surface with spacing length of 1.5 µm. This finding highlights that the ratio of capillary pressure (antiwetting pressure) to dynamic pressure and water hammer pressure (wetting pressures) at this point is maximum.

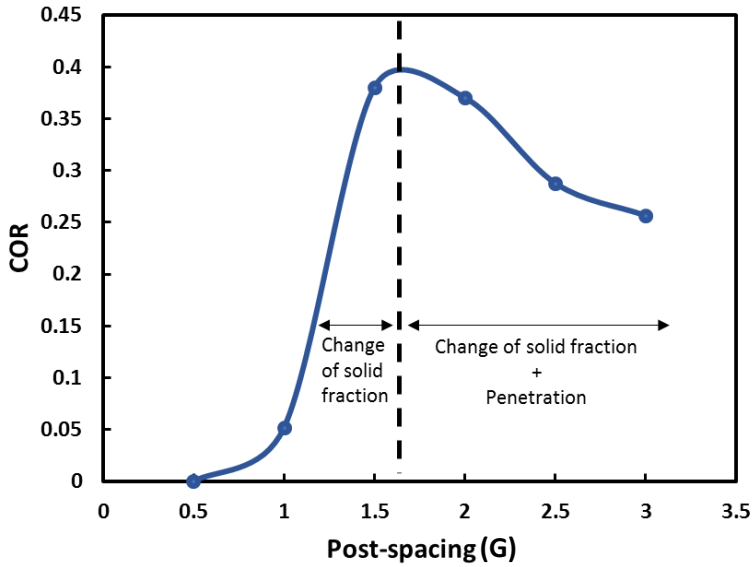

Figure 2-9: Numerical results of 20 µm droplet COR (Coefficient of Restitution) for different microstructured surfaces subjected to different spacing lengths

The contact time is defined as the time it takes for a droplet to touch the surface until it first bounces off from the surface. Different parameters affect the contact time of a droplet, such as viscous dissipation rate, surface topography, relative viscosity and relative density of liquid-gas, etc. Figure 2-10 shows the effect of the width to the spacing ratio (*W/G*) of the textured surface on the contact time of a 20 µm droplet impact. The smallest contact time was obtained from the impact of the micro-drop onto a micro-arrayed surface with 1.5 µm spacing length. Smaller and greater

spacing lengths lead to higher contact time. However, the trend for larger spacing length is not as steep as the smaller lengths, and this is because of the penetration of droplet for larger spacing.

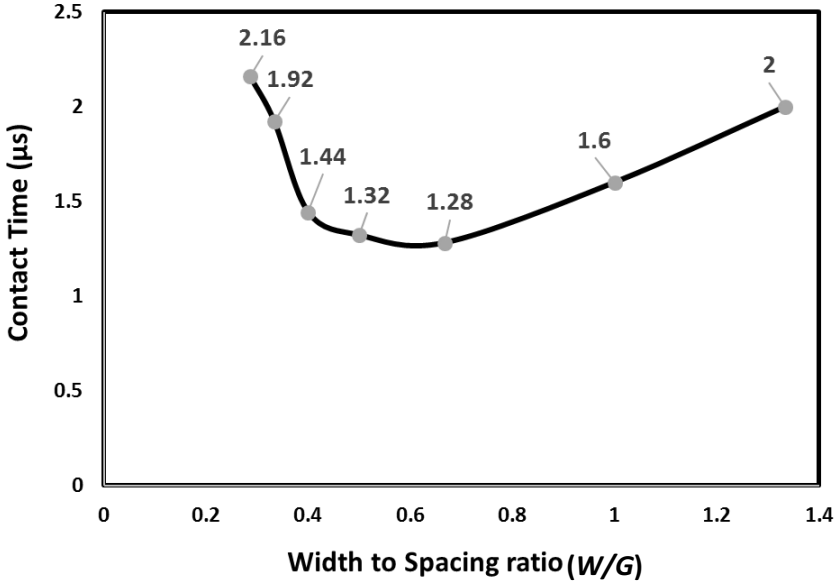

Figure 2-10: Numerical results of the 20 µm droplet contact time onto different textured surfaces for various width to spacing ratios (W/G) on surface with constant pillars width

2.5.5 Effect of Impact location on Contact Time

Experimentally it is no possible to determine the exact location of impingement, especially for droplets within 20-100 µm size range. Therefore a quantitative study was carried out to examine contact time for different possible impact locations on the textured surfaces (Figure 2-11). Black dots in this figure represents the location of the impact that is set in the simulation. Based on the results, the maximum contact time Δt_{max} is observed when the droplet impacts at the gap centers between the pillars, and the least contact time, Δt_{min}, when the droplet hits the center of a pillar top. Nevertheless, contact time was changed only by 3% in total. Although the effect of the impact point on the contact time may not be significant for a single droplet, such effect may become very important when dealing with the impact of a spray on textured surfaces, as required by many industrial applications.

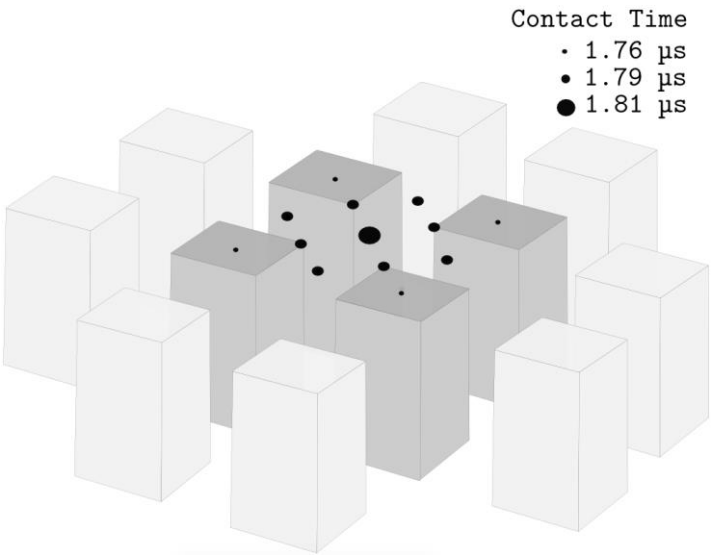

Figure 2-11: Contact time at different impact locations.

2.6 Conclusions

The numerical simulation of the impact of a 20 µm droplet onto a series of roughened surfaces is performed using a volume of fluid method. Despite non-repelling property of the surface, the droplet starts rebounding from the substrate at some point by including surface roughness and changing the surface topography configurations. By controlling the physical property of roughness, we were able to obtain the optimum surface configuration where the non-wetting behavior is significant. As per results, the maximum jumping velocity, as well as the minimum contact time, was obtained on the surface with squared arrays of nearly 1.5 µm spacing length when the pitch was kept constant, and the spacing of 0.7 when the pillars width was kept constant. The simulation successfully captured the effect of the air beneath the droplet inside microgrooves, which increased the apparent contact angle, and reduced surface energy level. The arrays post-spacing length and pillars width are found to control both the contact time and the maximum spreading diameter of the micro-droplet, making it an attractive design parameter for super-hydrophobic textured surfaces. In addition to the simulations, an analytical model was derived to

predict the spreading length of the droplet on the micro-structured superhydrophobic surface. Data obtained from the analytical model was in good agreement with the simulation results. Both models agreed on the parabolic behavior of contact time with respect to the gradual change of surface roughness dependent variables.

Chapter 3

Coalescence-Induced Jumping of Micro-Droplets on Heterogeneous Superhydrophobic Surfaces

3.1 Abstract

The phenomenon of droplets coalescence-induced self-propelled jumping on homogeneous and heterogeneous superhydrophobic surfaces was numerically modeled using the volume of fluid (VOF) method coupled with a dynamic contact angle model. The heterogeneity of the surface was directly modeled as a series of micro-patterned pillars. To resolve the influence of air around droplet and between the pillars, extensive simulations were performed for different droplets sizes on a textured surface. Parallel computations with the OpenMP algorithm were used to accelerate computation speed to meet the convergence criteria. The composition of the air-solid surface underneath droplet facilitated capturing the transition from a no-slip/no-penetration to a partial-slip with penetration as the contact line at triple point started moving to the air pockets. The wettability effect from the nanoscopic roughness and the coating was included in the model by using the intrinsic contact angle obtained from a previously published study. As the coalescence started, the radial velocity of the coalescing liquid bridge was partially reverted to the upward direction due to the counter-action of the surface. However, we found that the velocity varied with the size of the droplets. Part of the droplet kinetic energy was dissipated as the merged droplet

started penetrating into the cavities. This was due to a different area in contact between the liquid and solid and, consequently, a higher viscous dissipation rate in the system. We showed that the effect of surface roughness is strongly significant when the size of the micro-droplet is comparable with the size of the roughness features. In addition, the relevance of droplet size to surface roughness (critical relative roughness) was numerically quantified. We also found that regardless of the viscous cut-off radius, as the relative roughness approached the value of 44, the direct inclusion of surface topography was crucial in the modelling of the droplet-surface interaction. Finally, we validated our model against existing experimental data in the literature, verifying the effect of relative roughness on the jumping velocity of a merged droplet.

Keywords: Volume of Fluid, Superhydrophobic, micro-droplet, self-repellent surface, dynamic contact angle model.

3.2 Introduction

The self-propelled jumping of droplets is a phenomenon with a number of potential applications, such as self-cleaning [108], anti-icing [109], anti-dew [110], and condensation heat transfers enhancement [111]. The instantaneous rebounding of merged droplets on the superhydrophobic surface after coalescence is due to an excess of kinetic energy obtained from the difference in total surface energy levels [110]. This behavior has been quantitatively studied based on the capillary length [112]. For droplets smaller than capillary length ($\lambda_c = \sqrt{\frac{\sigma}{\rho g}}$), influence of the gravitational force can be neglected. Meanwhile, for droplets larger than capillary length, self-jumping has not been observed, due to viscous effects and the domination of the gravitational force [112], [113].

When two micro-droplets coalesce, the merged droplet self-propels and jumps off the surface [114], [115]. This process can be described by the Ohnesorge number (*Oh*) which indicates the ratio of viscous to surface forces for two identical droplets ($Oh = \frac{\mu_d}{\sqrt{\rho_d \sigma r_0}}$), and can determine the viscous cut-off threshold. Boreyko et al.,[116] determined the viscous cut-off size at $Oh = 0.3$ from their experiment. For *Oh* smaller than the viscous cut-off radius, droplet coalescence results in jumping of the merged droplet. As the Ohnesorge number increases toward unity, the viscous effects dominate during the coalescence which slows down the dynamics, and consequently, there is insufficient energy available for the self-propelled behavior [114], [115]. Boreyko and Chen [116] were the first to report their experimental observation of self-repellent water droplets on a superhydrophobic surface. They measured the jumping velocity for droplets of sizes ranging from 16 to 300 μm and reported that the jumping velocity (V_j) follows an inertia–capillary scaling law [116],

$$V_j \sim V_{ic} = \sqrt{\frac{6\sigma_d}{\rho_d} \frac{r_1^2 + r_2^2 - (r_1^3 + r_2^3)^{2/3}}{r_1^3 + r_2^3}}. \tag{3-1}$$

where V_{ic} is the inertial-capillary velocity, σ_d is the surface tension, ρ_d is the density of the droplet, and r_0 is the initial droplet size (i.e., before coalescence). Their results showed that the jumping velocity increases with size, reaches a maximum, and then decreases with further increase in size.

Much work has been dedicated to studying the mechanism of coalescence-induced jumping of microdroplets on superhydrophobic surfaces using energy balance approach to predict the jumping velocity of coalesced droplet [117], [118]. When two droplets of radius r_0 coalesce (Figure 3-1), the equilibrium radius of the merged droplet is $2^{1/3} r_0$ with a mass of $m = \frac{8}{3}\rho\pi {r_0}^3$. Due to reduction in the overall surface area, there is a release of surface energy $\Delta\delta = 4\sigma\pi {r_0}^2(2 - \sqrt[3]{2})$ or

$0.37{r_0}^2$ for water. This release of surface energy provides just enough energy for the droplet to jump off the surface.

For micro-droplets of equal radius, i.e., $r_1 = r_2 = r_0$, the inertial capillary velocity (3-1) reduces to,

$$V_{ic} = \sqrt{\frac{\sigma_d}{\rho_d r_0}}, \tag{3-2}$$

and the merging time scale becomes,

$$t_{ic} \approx \sqrt{\frac{\rho_d r_0^3}{\sigma_d}}. \tag{3-3}$$

If no energy dissipates during the coalescence, while the entire surface energy transforms into translational kinetic energy, the droplet will have a jumping velocity of $\sqrt{2\Delta E_s/m} = 1.11V_{ic}$.

This approach becomes challenging when the effect of droplet adhesion with the surface comes into account, and even more so if the coalescence occurs on a roughened surface (e.g., superhydrophobic) (Figure 3-1). In this figure, a twin droplet with a radius of r_0 coalescing to form a larger droplet with a radius of R onto a smooth and a rough surface. As a result of coalescence, the merged droplet self-clean the surface without the interference of any external forces. A direct theoretical investigation of the jumping behavior of the coalesced droplet on a rough surface is difficult because of some uncertain factors, such as the unknown penetrating depth of the coalescing droplets, the complicated viscous dissipation during coalescence and retraction stage, and the complicated geometric configuration of the liquid interface.

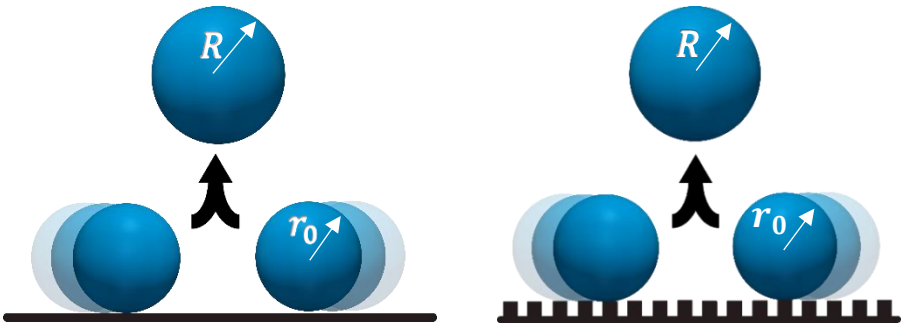

(a) (b)

Figure 3-1: Schematic of two droplets (r_0) is coalescing and the jumping droplet (R) on two surfaces: a) Homogeneous surface, b) Micro-structured or heterogeneous surface.

The initial location of the coalescing droplets with respect to each other have been an interesting and extensive topic in the literature. Baroudi et al. [119] compared the simulated results for two droplets separated by a small finite distance, and two droplets connected by a small finite contact. For initially connected drops, they observed the slower initial growth of the bridge radius. Narhe et al. [120] compared the experimental data obtained from droplet deposition technique and condensation technique to induce the onset of coalescence. The dynamics of coalescence induced with syringe deposition found to be faster by an order of magnitude. However, the oscillation induced by the syringe during deposition pulls the contact line at the time of coalescence. This means that the contact line motion studies carried with the traditional technique were not accurate because of uncontrollable oscillation of the droplet interface.

There has been much research dedicated to numerical modelling of large droplets coalescing in sessile and dynamic conditions. Farhangi et al. [121] examined the impact and coalescence induced jumping of two droplets on a superhydrophobic surface. They showed that the falling liquid droplet with a small amount of kinetic energy could clean the surface. Moghtadernejad et

al.[122] numerically simulated shear driven droplets and coalescence on a superhydrophobic surface. In their model, the low-pressure zone behind the droplet caused the second droplet to be dragged toward the first droplet which initiated the onset of coalescence and eventually self-jumping on the surface.

Study of micro-droplets with solid surface interaction is relatively new, and not many numerical studies have been carried to understand the effects of surface roughness on the dynamics of micro-droplets. This is likely due to the complexity of the roughness topography and the high computational cost of these simulations. Most of the studies in the literature were performed on smooth surfaces in which a liquid-solid contact angle is imposed as a boundary condition depending on the wetting property of the surface. This assumption neglects the effect of entrapped air underneath droplet, partial penetration of the droplet, and the changes in the geometrical configuration of the droplet due to the contact with surface irregularities when the size is comparable to the size of roughness.

In the study of micron-size droplets coalescence, Liu et al. [117] recently simulated the coalescence of two identical droplets on a smooth surface with a 180° equilibrium contact angle using the 3D phase field method limited to density ratios smaller than 100. One of the main drawbacks of equilibrium contact angle (180°) modelling is the assumed zero adhesion force between droplet and surface. This causes the estimated jumping velocities to be somewhat higher than that in the experiments.

Peng et al. [123] used the 3D Lattice Boltzmann method (LBM) to analyze the dynamics of coalescence and simulated the jumping height of the micro-droplets with different surface wettabilities. They revealed that if the size of the droplet is small, only 25% of the energy released by the droplet coalescence is converted to the effective kinetic energy in the vertical direction. In

addition, they showed that the air has little effect on jumping height of the coalesced droplet due to the droplet's velocity and radius.

Recently, Liu et al. [124] used a 2D LBM model based on the pseudo-potential approach proposed by Shan and Chen [125], with a modification of the real gas equation of state to simulate the jumping of a micro-droplet on a microstructured surface. However, in their two-dimensional model, the lower portion of the droplet was not allowed to fall freely into the micro-grooves, as the air was trapped in the gaps with no way to escape.

Liu et al. [117] used an LBM model based on Navier-Stokes diffuse interface model (NS-DIM) to capture the evolution of two droplets during the coalescence for droplets ranging from 3 nm–150 μm. Although their prediction indicated good agreement with the experimental, they ignored the effect of surface adhesion in their models.

Farokhirad et al. [126] performed a 3D LBM study and applied the method proposed by Lee et al. [127] to explore the evolution of two identical micro-droplets during the coalescence and jumping processes, where inertia is dominant over viscosity. They compared their results with a previously published experimental data which was performed on a superhydrophobic surface composed of micro/nano roughnesses. However, they ignored the effect of modified adhesion (i.e., hierarchical roughness) and the penetration of micro-droplet between cavities in their model. Their results were in good agreement with the experimental data for small size droplets, but it was limited only to the jumping velocity of the merged droplet.

Although numerous investigations have been conducted to understand the effect of surface roughness and wettability on the droplet dynamics, there has been limited attempts to investigate

the effect of hierarchical roughness (composed of micro/nano-scale roughness typical of those in superhydrophobic surfaces) on the dynamics of micron-sized droplets. In this study, to analyze this effect, the micro-topography is directly modeled, and the effect of lateral roughness levels (nano-topology) is included in the form of an appropriate contact angle.

3.3 Methodology

3.3.1 Numerical model

All numerical simulations were performed using Open Source Field Operation And Manipulation (OpenFOAM) C++ libraries, a free-source CFD-toolbox developed by OpenCFD [128]. The code is based on the finite-volume numerical method with the co-located variable arrangement for solving systems of transient transport equations on arbitrary unstructured meshes in three-dimensional space. The overall solution strategy is based on the Pressure Implicit with Splitting of Operators (PISO) algorithm. Time derivative terms are discretized using an implicit Euler scheme. The source and transient terms are discretized using the midpoint rule, and for the evaluation of gradients, a linear face interpolation is used. The discretization of the of convective terms is based on high-resolution differencing scheme.

The volume of fluid (VOF) [100] interface capturing method is used to investigate the self-propelled jumping behavior of micro-droplets after coalescence on homogeneous or heterogeneous superhydrophobic surfaces. In the VOF method, tracking of the liquid-air interface is modeled by solving the continuity equation for one of the two phases in each computational cell at every time step. The governing equations for continuity and momentum are,

$$\nabla\vec{V}=0, \tag{3-4}$$

$$\frac{\partial\rho\vec{V}}{\partial t}+\nabla.\left(\rho\vec{V}\vec{V}\right)=-\nabla p+\nabla.\left(\mu.\nabla\vec{V}\right)+\left(\nabla\vec{V}\right).\nabla\mu-g.x\nabla\rho+F_b \tag{3-5}$$

where t is time, $\vec{V}$ is the velocity vector, x is the coordinate vector and F_b is the body force. The volume fraction is presented by α, which is used to calculate the viscosity, μ, and density, ρ, as weighted averages based on the distribution of the liquid fraction,

$$\rho=\alpha\rho_d+(1-\alpha)\rho_g, \quad \& \quad \mu=\alpha\mu_d+(1-\alpha)\mu_g, \tag{3-6}$$

where the subscripts d and g denote the liquid droplet and the gas phases, respectively. In the VOF method, the phase fraction scalers function (α) takes a value between 0 and 1, where $\alpha = 1$ corresponds to the liquid phase, $\alpha = 0$ to the gas phase, and $0 < \alpha < 1$ corresponds to where the interface is located. In numerical simulations of free surface flows using VOF model, it is crucial to assure boundedness and conservativeness of the phase fraction. In flows with high density ratios, small errors in volume fraction may lead to significant errors in calculations of physical properties. Therefore, accurate calculation of the phase fraction distribution is vital for a proper evaluation of surface curvature, which is required for the determination of surface tension force and the corresponding pressure gradient across the free surface. It should be mentioned that the accuracy of interface reconstruction depends on mesh resolution. As the interface evolves with the motion of fluid, it is essential that the volume tracer satisfies the advection equation,

$$\frac{\partial\alpha}{\partial t}+(\vec{V}\nabla)\alpha+\nabla.\left(\vec{V}_r\alpha(1-\alpha)\right)=0, \tag{3-7}$$

where $\vec{V}_r$ is the vector of relative velocity, designated as the compression velocity term introduced by Rusche [101] to facilitate a sharp interface between phases,

$$\vec{V}_r = \vec{n} \min\left[C_\alpha \frac{\varphi}{|S_f|}, max \frac{\varphi}{|S_f|}\right], \tag{3-8}$$

where φ, S_f, C_α and $\vec{n}$ are the face volume flux, cell face area vector, compression coefficient, and face unit normal flux, respectively. The face unit normal also is defined by the below equation where C_α is an adjustable factor used to adjust the amount of compression. We used $C_\alpha = 1.5$ which was also shown by Rusche [101] to provide a sharp interface between phases. The interface unit normal $\vec{n}$ is computed by taking the gradient of the smoothed volume fraction α at the cell faces,

$$\vec{n} = \frac{\nabla\alpha}{|\nabla\alpha| + \delta}, \tag{3-9}$$

where δ, is a small number in order to stabilize the calculation in regions outside the transition region (where $|\nabla\alpha| \rightarrow 0$). In this study, $\delta = 10^{-8}$ was used for all simulations.

The main benefit of such formulation is the possibility of capturing the interface region much more sharply in comparison to the classical VOF approach. Numerical diffusion can be controlled and minimized through the discretization of the compression term, thus allowing sharp interface resolution.

The continuum surface force model [129] is used to model surface tension as the main body force $\vec{F}_b$ that acts only on interfacial cells,

$$\vec{F}_b = \sigma_d k \nabla\alpha, \tag{3-10}$$

where k is the mean curvature of the free surface, calculated by,

$$\vec{k} = -\nabla.\left(\frac{\nabla\alpha}{|\nabla\alpha|}\right). \tag{3-11}$$

3.3.2 Non-dimensional analysis and physical properties

All physical quantities were non-dimensionalized as shown in Table 3-1,

Table 3-1: Dimensionless parameters used in this study

normalized penetration depth	non-dimensional jumping velocity	non-dimensional timescale	non-dimensional pressure
$H^* = \left(\frac{\delta_p}{H}\right)$	$v^* = \frac{v(t)}{\sqrt{\frac{\delta_d}{\rho_d r_0}}}$	$t^* = \frac{t}{\sqrt{\frac{\rho_d r_0^3}{\sigma_d}}}$	$P^* = \frac{P r_0}{\sigma_d}$

In the table above, δ_p is the physical penetration depth of a droplet, H is height of the pillars, r_0 is radius of the liquid droplets before they coalesce, ρ_d and σ_d are the density and the surface tension of the liquid droplet, respectively. Since the jumping droplets are smaller than the capillary length ($\lambda_c = \sqrt{\frac{\sigma_d}{\rho_d g}} = 0.0027$), the gravitational force is neglected in the model [130].

The physical properties of droplet and gas were assumed to be the literature values at 20 °C (TABLE I), to simulate fluid properties during the superhydrophobic condensation experiments [131].

Table 3-2: The fluid properties of both air and water at 20℃ [14]

T $(°C)$	σ_d (N/m)	μ_d $(Pa.s)$	μ_g $(Pa.s)$	μ_d/μ_g	ρ_d (kg/m^3)	ρ_g (kg/m^3)	ρ_d/ρ_g
20	0.072	1.071×10^3	0.018×10^3	58.8	998	1.190	841

The vertical velocity of the merged droplet resulting from the coalescence of two individual droplets was measured numerically as the vertical component velocity at the center-of-mass of the droplet,

$$v_y(t) = \frac{\int_{\emptyset} \alpha v_y \, d\emptyset}{\int_{\emptyset} \alpha \, d\emptyset} \tag{3-12}$$

where $\emptyset$ represents whole computational domain, v_y is the vertical direction perpendicular to the substrate, and α is the VOF scalar tracer that localizes the calculation of the droplet or iso-surface.

Additionally, the average surface roughness can be determine using the following equation,

$$R_a = \frac{1}{L}\int_0^L |f(x)|dx \tag{3-13}$$

Where L is the evaluation length and $f(x)$ is the surface topography height function.

3.3.3 Computational domain

The computational domain size of 350 (μm) × 250 (μm) × 350 (μm) was used for the 3D simulation of two merging droplets on a heterogeneous superhydrophobic surface as shown in Figure 3-2. As the coalescence of the micro-droplets occur in an open system, the top and side surfaces of the computational domain were considered to carry no gradient effect of pressure and velocity. The side walls extended far enough $(Domain_{width} \geq 8r_0)$ from the location of coalescence to ensure that the imposed pressure boundary conditions would have a minimal effect on the dynamics of the coalescence. Further inhomogeneity, surface irregularities, and bubble entrapment inside the droplets before coalescence were neglected in this study. The surface bottom (homogeneous model) and the surface of the micro-pillars (heterogeneous) were considered as no-slip walls.

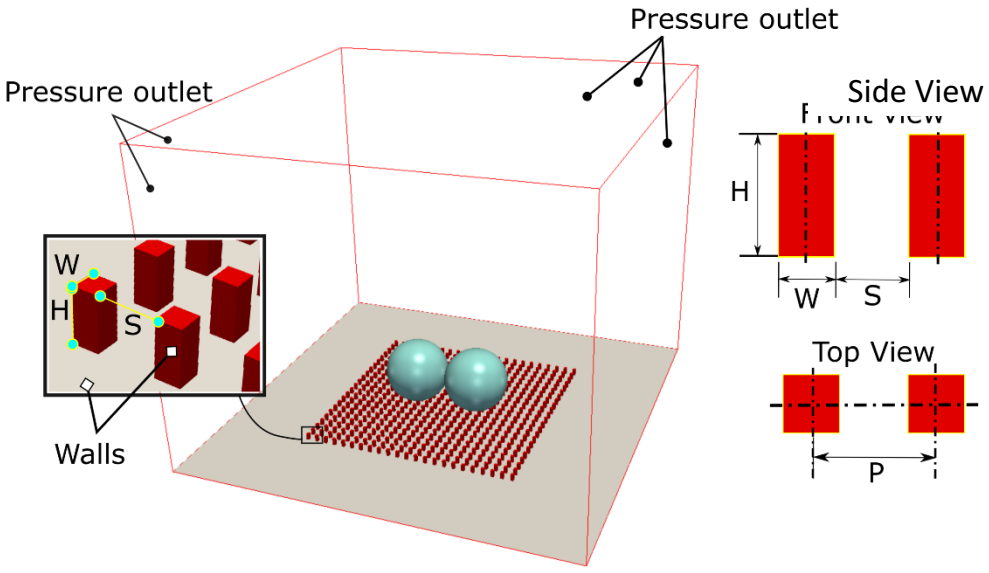

Figure 3-2: 3D computational domain for droplets with their interface touching before the onset of coalescence.

For the homogeneous superhydrophobic surface, the surface was assumed to be a smooth object with no surface irregularities. All features of the superhydrophobic surface including physical and chemical properties of the surface were included in the form of an intrinsic contact angle (Table 3). According to Young, it is theoretically possible for a surface to have a contact angle of 180°, but no physical evidence has been reported to demonstrate this situation. Therefore, a high static contact angle near 180° was selected for the simulations for the homogeneous surface. However, a large static contact angle does not necessarily mean an easy removal from the surface, since the hysteresis of the surface can be large. Therefore, the static, advancing and receding contact angles of, 177°, 176°, and 178° respectively were used in order to model a highly repellent surface.

On the other hand, the experimental surface was composed of two-tier surface roughness, a Hexadecatheniol coating on carbon nanotubes which were deposited on silicon micro-pillars. The

effects of roughness (Figure 3-3) on the droplets is analyzed by using the relative roughness ($\boldsymbol{\varepsilon}$), which relates the initial droplet's diameter to the average roughness of the surface.

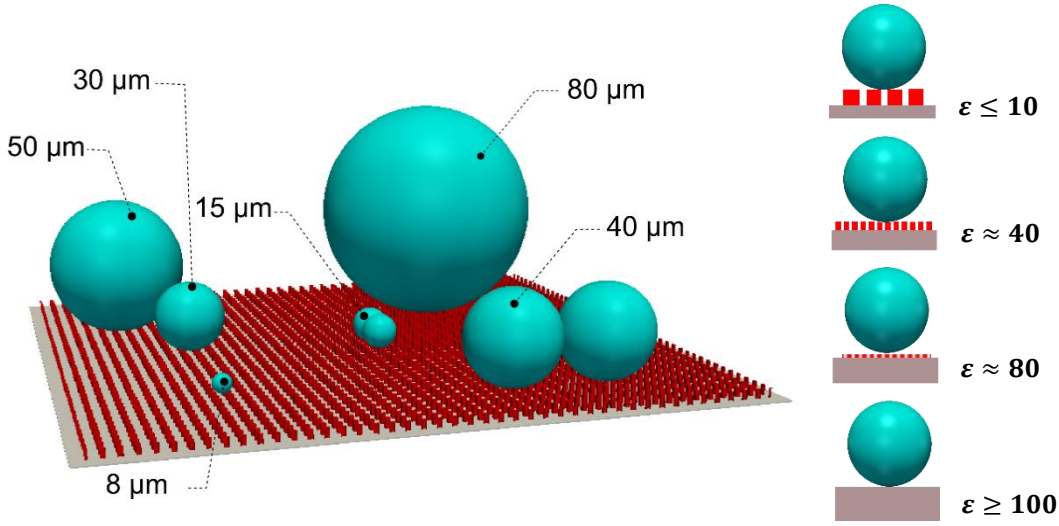

Figure 3-3: Representation of micro-droplets at different radius sitting onto the textured surface, and relative roughness $\left(\varepsilon = \frac{Droplet\ Diameter}{Average\ Surface\ Roughness}\right)$.

In order to model the heterogeneous surface, the roughness associated with the micro-silicon pillars ($10 < \varepsilon < 100$) was directly modeled as a series of micro-pillars (Table 3). The combined effect of the Hexadecatheniol coating as well as the roughness associated with the carbon nanotubes ($\varepsilon \gg 100$) was included by the choice of the Kistler's dynamic contact angle model [102] imposed over the outer surface of the micro-pillars (Figure 3-4).

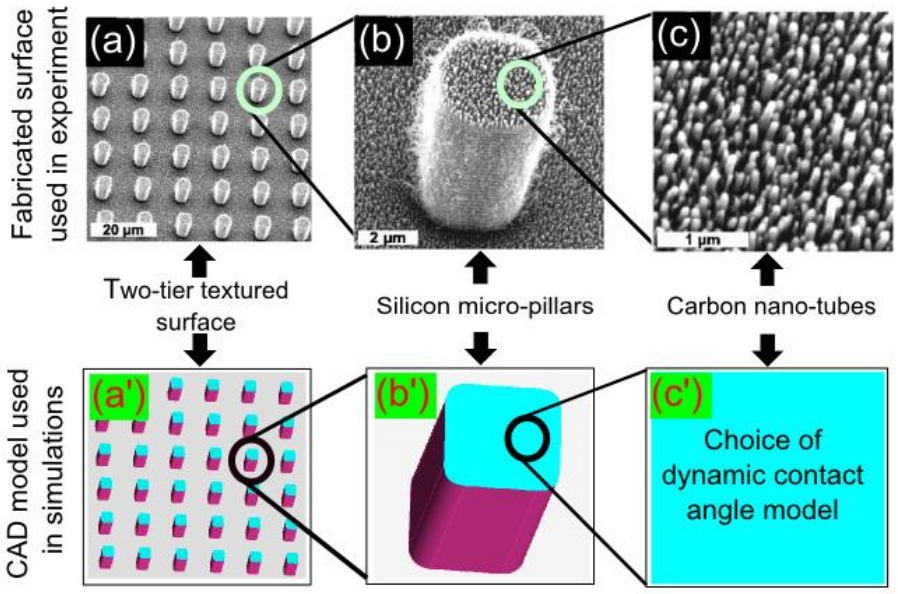

Figure 3-4: Two-tier roughness with coated carbon nanotubes deposited on silicon micro-pillars fabricated surface used in the experiment [131] and the 3D CAD model that is employed in simulations.

The surface is a square pattern of square pillars with height (H), width (W), and pitch (L) of 8 μm, 3.7 μm and, 12 μm, respectively.

Table 3-3: Parameters of micro- and nano-textures on a two-tier roughened surface. The physical dimensions of the pillars (W) assuming a squared cross section, pitch (L), height (H), solid fraction (f), surface roughness (R_a), and critical contact angle.

Structure	W (μm)	L (μm)	H (μm)	f	R_a
Micro level	3.7	12	8	0.095	1.8
Nano level	0.06	0.12	0.4	0.25	7.7

The contact angle measured in the experiment [131] corresponds to the apparent contact angle of a droplet sitting on a deposited carbon nano-tubes which are coated with Hexadecatheniol. The fraction of solid surface in contact with liquid (f) in Cassie state is calculated from, $f = W^2/L^2$,

and the roughness ratio of total surface area in contact with liquid over the projected area in Wenzel state, $R_a = (L + 4WH)/L^2$.

Table 3-4: Contact angles of the surface used in the simulation

	θ_S	θ_A	θ_R
Homogeneous	177˚	178˚	176˚
Heterogeneous	105˚ - 110˚	116˚	100˚

θ_S is the static or apparent contact angle.

θ_A is the advancing contact angle.

θ_R is the receding contact angle.

3.3.4 Dynamic contact angle model

For a perfectly wetting surface, equilibrium or static contact angle is nearly zero ($\theta_S \approx 0$). However, for a partially wetting surface, the choice of an appropriate contact angle model is not simple. Despite all the efforts in numerical modelling of wetting process, the existing models often fail to correctly predict the result of the experiments. This is due to the difficulties associated with the motion of contact line. Modelling of contact angle which is in the form of a boundary condition, determines the shape of the free surface and the dynamic of contact line. There is an extensive theoretical and empirical study of contact line motion in the literature. In both models, it is common to relate the dynamic contact angle (θ_D) to the capillary number Ca and the static contact angle (θ_S), i.e. $\theta_d = \mathcal{F}(Ca, \theta_0)$ where $Ca = \frac{\mu_d |V_{cl}|}{\sigma_d}$, and Ca is the capillary number, $|V_{cl}|$ is the contact line velocity between the solid and liquid. Apart from the parameters in the equation, there are other parameters such as surface roughness, the surface inhomogeneity, existence of surfactant, polymers, coatings, and so on [132] that influence the dynamic contact angle [102], [133]. Therefore, selection of a universal relation for the dynamic contact angle is almost impossible.

In the previous studies of coalescence-induced jumping of micro-droplets on a solid surface, the static or equilibrium contact angle was used as for dynamic contact angle ($\theta_D = \theta_S$), which is the simplest of all models from an implementation point of view. The drawback of this model is that the dynamic contact angle is fixed to the equilibrium value during the computations, which corresponds to a zero-adhesion force between the droplet and surface. On the other side, real surfaces are never atomically smooth. The presence of roughness hinders the motion of droplet by pinning the contact line. If a force is applied to the liquid droplet, the droplet will not immediately move, but rather deform showing advancing and receding contact angles. Therefore, the equilibrium contact angle is not a good representation of the droplet–surface interaction during the dynamic, especially for micron size droplets.

In this study, the wettability of the surface was accounted for by using the dynamic contact angle model of Kistler [102]. Therefore, the surface adhesion was replicated by the contact angle hysteresis based on the values of surface energies through the Kistler's dynamic contact angle model. The Kistler's model is a modification of Hoffman's function to calculate the contact angle in each time step,

$$\theta_d = f_H[Ca + f_H^{-1}(\theta_A, \theta_S, \theta_R)], \tag{3-14}$$

where f_H is the Hoffman's function and is defined as,

$$f_H = \cos^{-1}\left\{1 - 2\tanh\left[5.16\left[\frac{x}{1 + 1.31x^{0.99}}\right]^{0.706}\right]\right\}. \tag{3-15}$$

In the above equation, the equilibrium contact angle θ_S can be replaced by either the advancing contact angle θ_A, or the receding contact angle θ_R depending on the direction of the velocity vector at the contact line. It is noteworthy that a no-slip model such as Kistler's model [102] has been

extensively used to investigate droplet dynamics. The dynamic contact angle models of Kistler tries to deal with the difference observed in experiments between the dynamic contact angle (at microscopic length scale) and the apparent contact angle (at macroscopic length scale) within the inner region near the triple line point. In addition, it has been shown that this model is capable of capturing the relevant physics of droplet–substrate interaction in a good agreement with experiments [95], [104], [134].

3.3.5 Grid dependency

To ensure that results are independent of domain resolution, the computational domain was discretized into three different sizes: 6 million, 15 million, and 30 million hexahedral computational elements, each with local refinement around the droplet and the interfacial cells.

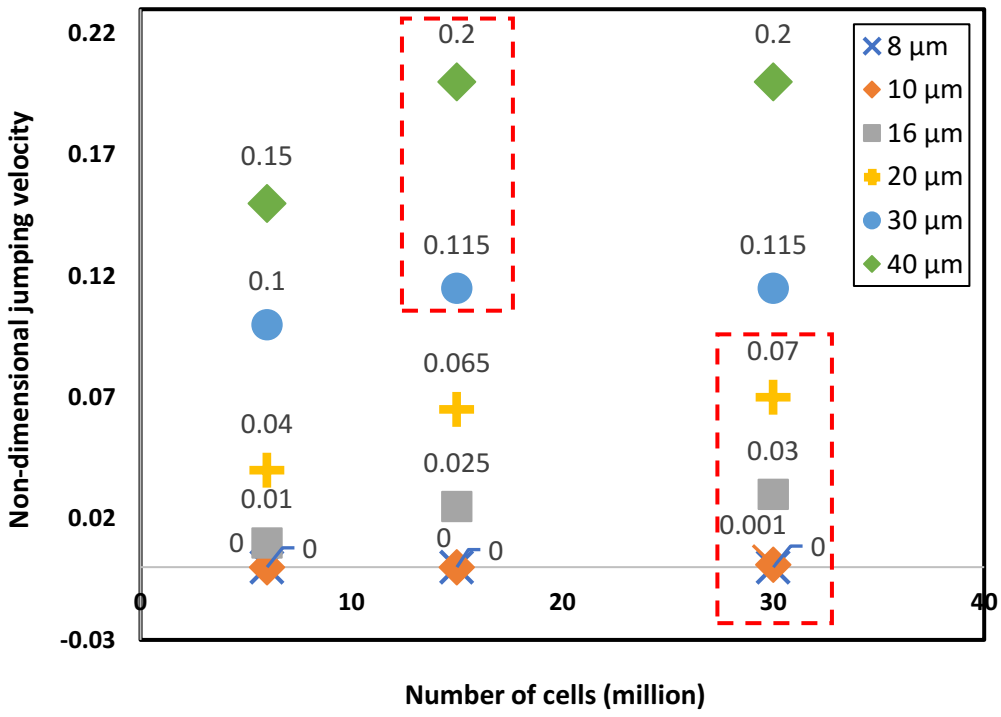

Figure 3-5: Grid dependency test for various droplet size is based on the convergence of jumping velocity. Data points in the red box indicating the grid sizes that are subject to study for each droplet size.

The mesh resolution test was performed based on the jumping velocities of the merged droplet onto the textured surface. This led to a minimum of 60 cells per droplet diameter. For droplets larger than 30 μm, as the difference in the jumping velocities with the cases of 15 million and 30 million cells was minimal, the domain composed of 15 million was used in this study. However, for droplets smaller than 30 μm, in order to maintain a minimum of 60 cells per diameter, the total mesh size was increased to 30 million to reduce the convergence time. Because of some numerical limitations, in order to minimize the degree of cells non-orthogonality, the rounded corners of the pillars are sharpened to form a square array.

3.4 Numerical Results and Discussion

In the coalescence process, two droplets merge, oscillate and eventually reach an equilibrium condition after a few oscillations. If there were no viscous effects on the liquid interface, the droplets would continue oscillating; however, due to the effects of liquid and gas viscosity and friction with the solid surface, the kinetic energy of the droplet will eventually dissipate.

According to Liu et al. [117] the jumping process of the micro-droplet due to coalescence can be divided into four stages: 1) Formation and gradual expansion of the liquid bridge before the two droplets reach their first pseudo-equilibrium state, 2) Acceleration of merged droplet as a result of non-wetting surface counteraction, 3) Merged droplet leaving the surface, 4) Deceleration of the jumping droplet in the air due to air friction. These stages are shown in Figure 3-6. In this study, the first three steps will be of great interest, which focuses on the interactions between the micro-droplet and the solid surface.

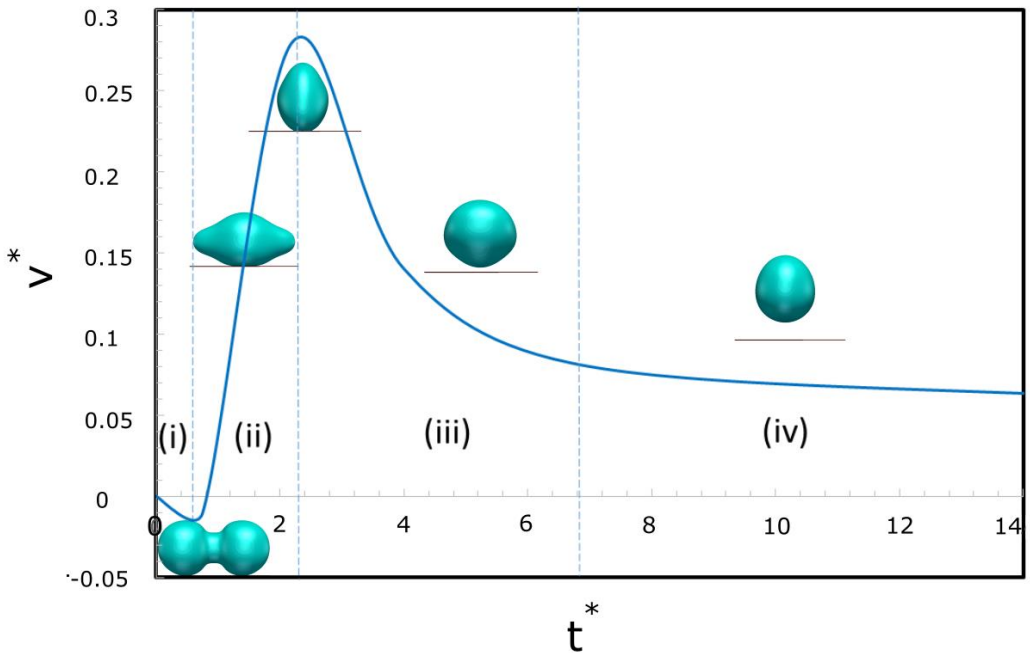

Figure 3-6: Time evolution of the droplet vertical velocity during the coalescence process.

3.4.1 Homogeneous superhydrophobic surface

To numerically model a superhydrophobic surface, simplification of the surface's physical features is the most common approach. In this method, the effects of both physical and chemical properties are merged as one physical contact angle to represent the wettability of the surface. Hence, the wettability of the surface is numerically implemented as a boundary condition in the neighboring cells to the walls, where the adhesive force between the liquid and solid is defined. This technique has been proven to provide accurate results in describing the temporal evolution of the large droplets. In this study, we started by simulating the coalescence of two micro-droplets on a homogeneous (smooth) superhydrophobic surface surrounded by air.

Figure 3-7 shows the time-lapse evolution of two merging micro-droplets ($R = 80\ \mu m$) on a homogeneous superhydrophobic surface. At $t^* = 0$ the micro-droplets were placed next to each

other with their edges overlapping, triggering the onset of coalescence. At the beginning of coalescence, a tiny liquid bridge between two droplets started to form. The expansion of the liquid bridge was driven by the surface tension and follows the scaling law [135], [136]. Because of the high inertia of the liquid bridge, an instantaneous Pseudo-levitation of the droplet was captured at $t^* = 0.6$ until the liquid bridge fully expands and reach the surface. While the liquid bridge was forming, the downward motion of the liquid was converted to upward motion due to counter action with the surface, causing the jump. In the meantime, the small adhesion force between the two-media facilitated the jumping process for the micro-droplet. Finally, the merged micro-droplet jumped off the surface at $t^* = 3.1$. Using this approach, the coalescence of two micro-droplets was successfully modeled. However, the main drawback of this approach was the exclusion of surface roughness from the computational domain. In addition, this assumption ignored the penetration of the liquid droplet into the cavities, and eventually the change of interface evolution when the size of the droplet is similar to the size of roughness.

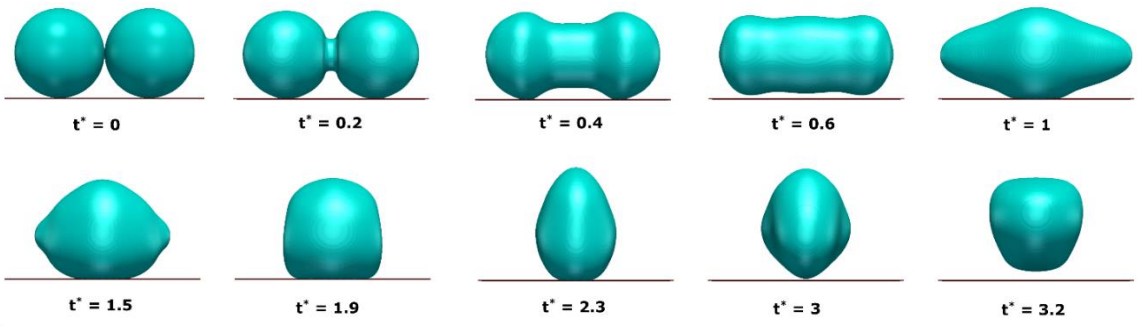

Figure 3-7: Time-lapse evolution of two identical $R = 80\ \mu m$ micro-droplets on homogeneous superhydrophobic surface ($\theta_s = 177°, \theta_A = 178,\ \theta_R = 176$).

The jumping velocity of the merged droplet on the homogeneous superhydrophobic surface is validated using the experimental data of Boreyko and Chen [116] and compared with the numerical simulations performed by Farrokhirad et al. [126], and Liu et al. [117]. Figure 3-8 shows the

simulation results for the jumping velocity of the merged droplet conducted by LBM [126], NS-DIM [117], and the present model (VOF), alongside the experimental data [116]. According to the experiment, the jumping velocity should follow the capillary inertia scaling $r_0{}^{-1/2}$ a prediction that was confirmed in this study. For droplets larger than $R = 40\ \mu m$, the three models have reported a nearly constant non-dimensional jumping velocity $V^* = \frac{v(t)}{V_j}$.

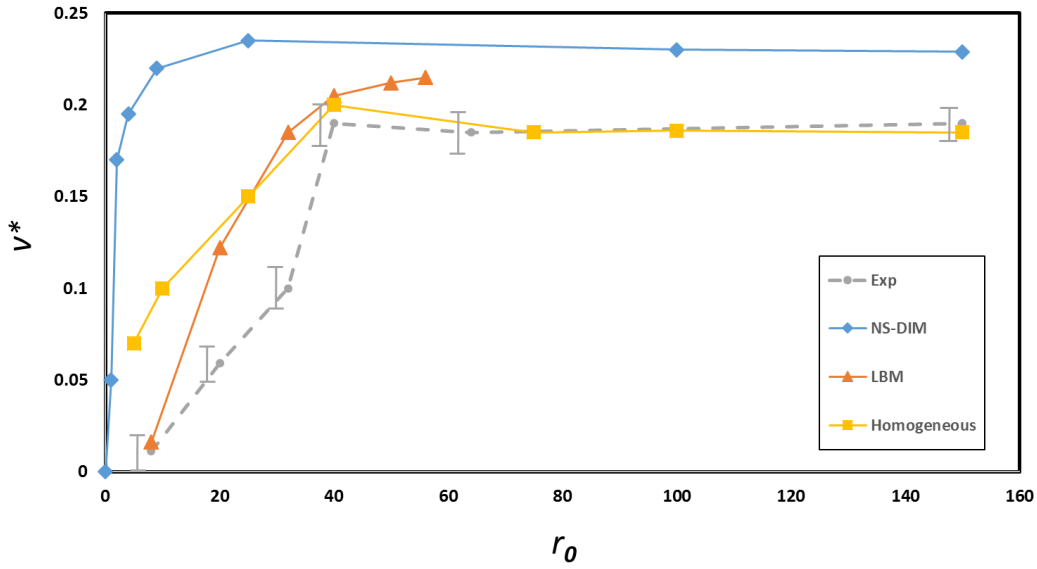

Figure 3-8: Comparison of jumping velocities for a merged micro-droplet(s) of different sizes from the numerical simulations of the present model on a homogeneous superhydrophobic surface with LBM [126], NS-DIM [117], and the experiment[9].

However, the results of the current model on a homogeneous surface were closer to the experimental data, than the other models since a constant non-dimensional jumping velocity of 0.2 was obtained. The numerical results of the homogeneous model for droplets smaller than $r_0 = 40\ \mu m$ did not match with the experiment (Figure 3-8). This deviation was even more for smaller droplets. For droplets smaller than 40 μm, the LBM [126] model provided a better match with the experiment in terms of jumping velocity of the merged droplet. However, the surface in all these studies was assumed to be smooth with no irregularity, hence, penetration of the liquid droplet into

the cavities was neglected. Consequently, this results in inappropriate calculation of the adhesion force between the surface and the liquid droplet.

3.4.2 Heterogeneous superhydrophobic surface

Besides an inaccurate measurement of adhesion force [135], [137], the topography of a surface can change the dynamics of a micro-droplet on said surfaces, especially when the size of the droplet is comparable with the size of roughness features. Therefore, heterogeneous modelling of the surface becomes necessary, to determine the force acting on the interfacial region. For heterogeneous surface, the homogeneous model was modified in the following way: 1) The combined effect of chemical coating and the carbon nanotubes were added in the form of a contact angle acting as a boundary condition, 2) All physical properties associated with the silicon micro-pillars were directly modelled, and 3) The high contact angle was replaced with the intrinsic contact angle of the surface material in contact with the micro-droplet measured in the experiment, and it was imposed on the outer surface of the micropillars. In this model, the coalescence between the two micro-droplets took place on a surface composed of solid and air layers.

Figure 3-9 and Figure 3-10 show the comparison between the time-lapse evolution of two identical micro-droplets coalescing ($r_0 = 20\,\mu m$) on a homogeneous or heterogeneous superhydrophobic surfaces. A similar mechanism was observed on both surfaces: formation of the liquid bridge, radial expansion of the bridge, and eventually the two droplets merge and formed a larger droplet. The differences were most noticeable when the downward motion of the liquid bridge started pushing the surface. In this case, as the air is free to move through the passages, it led the micro-droplet penetrate into the valleys.

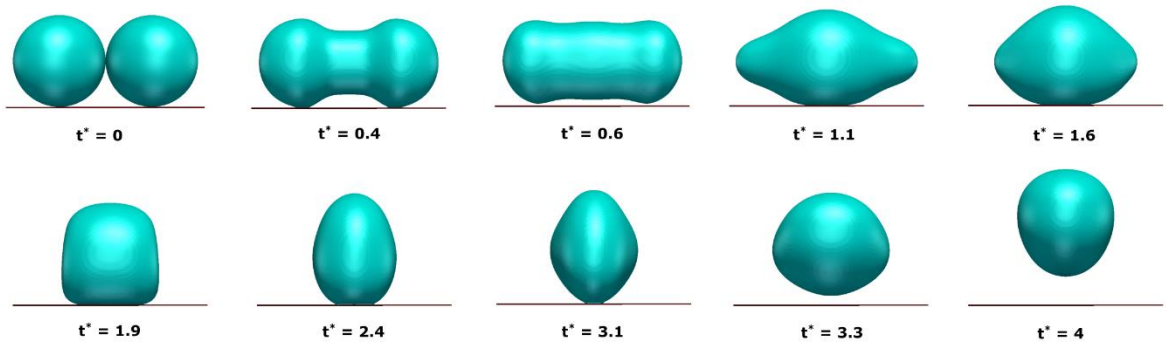

Figure 3-9: Time-lapse evolution of the coalescence of two micro-droplets (r_0 = 20 μm) on a homogeneous superhydrophobic surface.

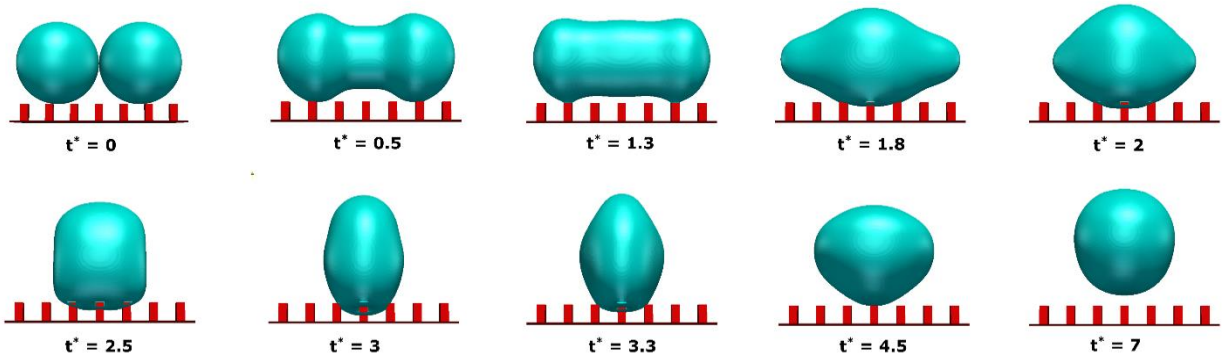

Figure 3-10: Time-lapse evolution of the coalescence of two micro-droplets (r_0 = 20 μm) on heterogeneous superhydrophobic surface.

When the merging micro-droplet was encroaching on the cavities in the textured surface, the capillary effect resists against penetration of the micro-droplet into the valleys. As shown in figures above, there was a change in the geometric evolution of the liquid interface as the droplet passed the first pseudo-equilibrium (zero absolute velocity) while it was preparing to jump on the homogeneous surface at $t^* = 1.9$, versus $t^* = 2.5$ onto heterogeneous surface. Although the spreading length was same in two cases, but penetration of the micro-droplet into cavities caused a significant delay in the initiation of the jumping process. Examining the data at $t^* = 3.3$ for the two models (Figure 3-9 and Figure 3-10), the micro-droplet was about to jump in the

heterogeneous model, but had already jumped from the homogeneous superhydrophobic surface. Because it took longer for the droplet to detach from the heterogeneous surface, more energy was dissipated, and a smaller jumping inertia was preserved to cause the jumping.

In order to trace the evolution of the interface during penetration, we clipped out a fraction of the liquid interface in the isometric view of the liquid interface underneath droplet, inside the cavities (Figure 3-11).

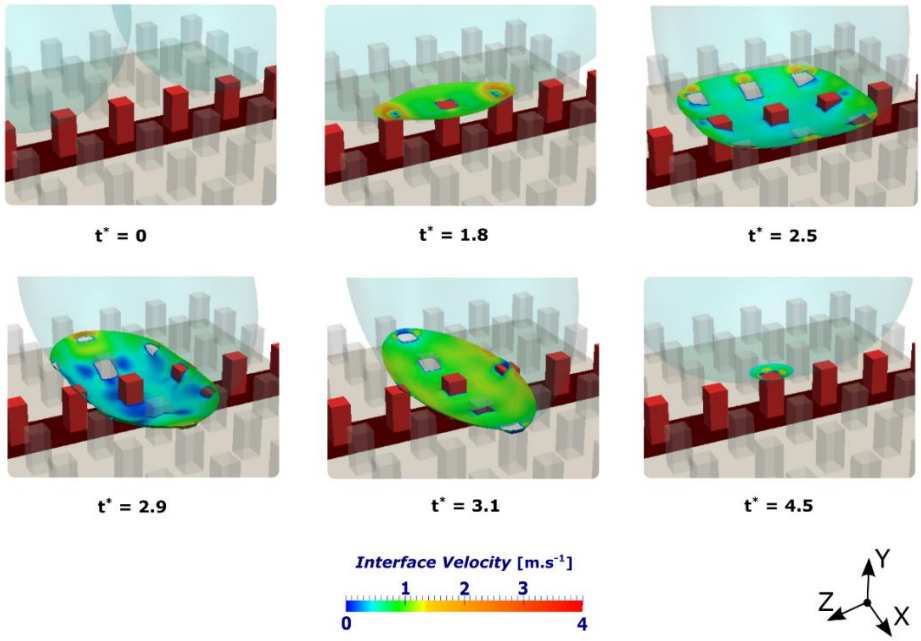

Figure 3-11: Time evolution of the liquid interface inside the cavities during the coalescence of two identical micro-droplets ($r_0 = 20\ \mu m$).

To better visualize the penetration, the strip of pillars is colored red in Figure 3-11. Two pseudo-equilibrium stages along the X and Z axes at $t^* = 2.9$ and $t^* = 4.5$, respectively, occurred before the micro-droplet completely jumped off the surface. The maximum penetration of the droplet occurred at the earliest stage of the first pseudo-equilibrium ($t^* = 2.9$) when the liquid bridge was fully formed. Due to the effect of surface tension, the liquid interface maintained its uniformity in curvature along the interface at the maximum penetration stage. The second pseudo-equilibrium

stage was at the time just before the micro-droplet jumped off the surface. Comparing the energy balance before and after the coalescence revealed that the jumping process was initiated when the released surface energy would be sufficient to overcome the total viscous effects. In addition to the dominant effect of viscosity to the surface tension for droplets above viscous cut-off threshold, we found that penetration of droplets into the cavities can further dissipate energy of the micro-droplet jumping.

In order to understand the dynamic of the air underneath the micro-droplet, a 3D rectangular section of the air domain was extracted (air pocket) for examination in the model. This pocket covered a periodic volume of space in which air passed through. Figure 3-12 shows the flow of air inside the pocket while it deformed as the result of coalescence at different time steps. The geometrical change of the air pocket is shown on top of each time step. The upper surface of the pocket was subjected to the curvature of the micro-droplet and mapped the pressure as droplet penetrated into the cavities and pressurized the air. In the earliest stages of the coalescence ($t^* = 0.5 - t^* = 1.8$), when the liquid bridge was forming, the outward motion of the air through four passages was observed.

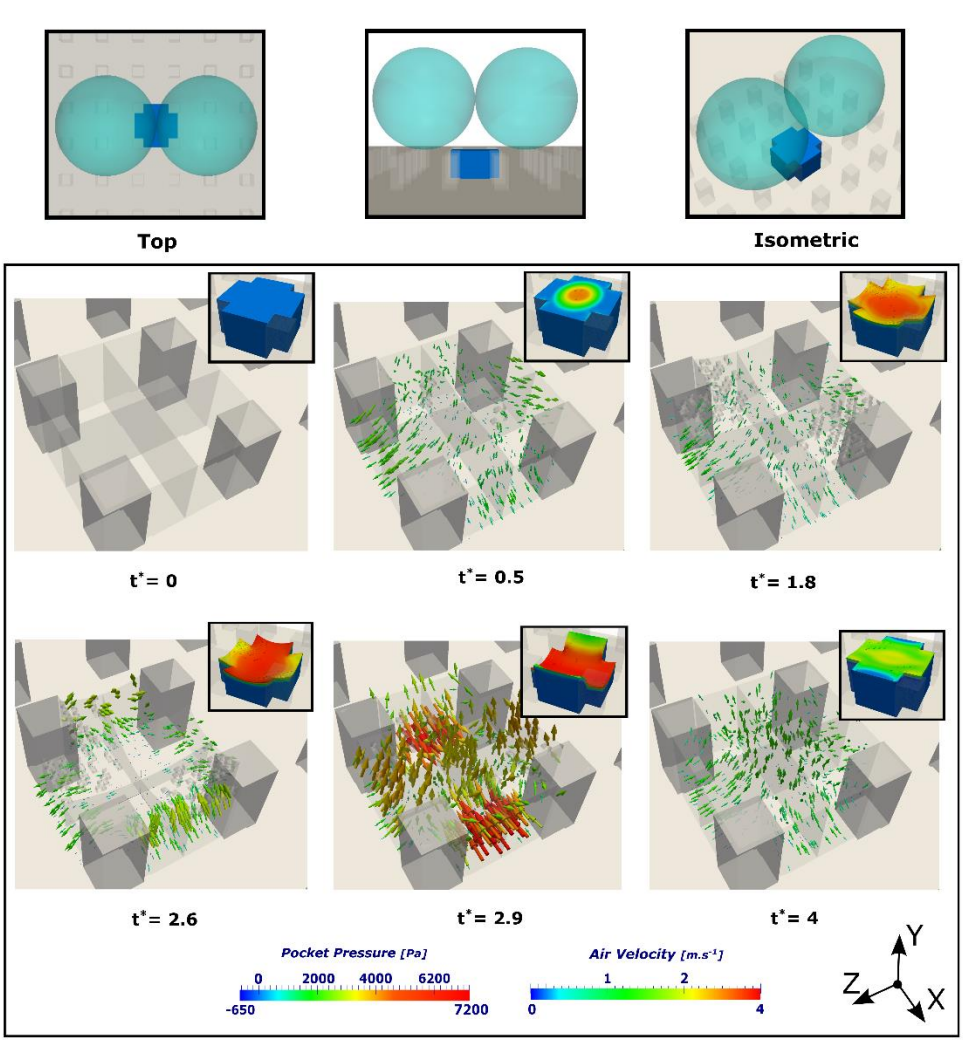

Figure 3-12: The evolution of the air pocket indicating the micro-droplet ($R = 20\ \mu m$) interface pressure on upper surface of the pocket shown in small boxes. Air velocity vectors inside the pockets at each time step are shown during the coalescence.

As the micro-droplet began penetrating the space between the pillars, the outward movement of air in the X direction changed to inward flow ($t^* = 2.5$). Due to the effects of surface tension, there is an axis switching from the X to the Z direction. This caused the motion of the air to remain inward in one direction and outward in the opposite direction during this time. At $t^* = 2.9$, the droplet reached its maximum spreading length in the X direction and formed a disk-shaped cusp

between the pillars. At this moment, the air attained its highest velocity in the X direction. At $t^* = 4$, the droplet was off the pocket, and the air pocket formed a square box.

Figure 3-13 shows the liquid interface and the interface normal velocity vectors (r_0 = 20 μm) at different time steps. At $t^* = 0.2$, we observed both upward and downward motion of the liquid bridge as it started expanding. The radial velocity of the bridge was the same below and above the droplet in the earlier stages of the bridge expansion. At $t^* = 1.8$, the downward velocity started decaying and changed its direction. Smaller sized droplets resulted in higher penetration of the micro-droplets into the cavities, which delayed the process. At $t^* = 2.2$, the formation of the liquid bridge was completed, and all of the surface energy was converted into translational kinetic energy which was partially dissipated due to viscous effects. At this time, the interface of two droplets moved inward with the maximum velocity of 2 $m.s^{-1}$.

Additionally, when the droplet reaches the maximum spreading length, it formed a disk shape ($t^* = 2.8$), and the interface velocity vectors pointed upward, which was an indication of the micro-droplet's impending jump.

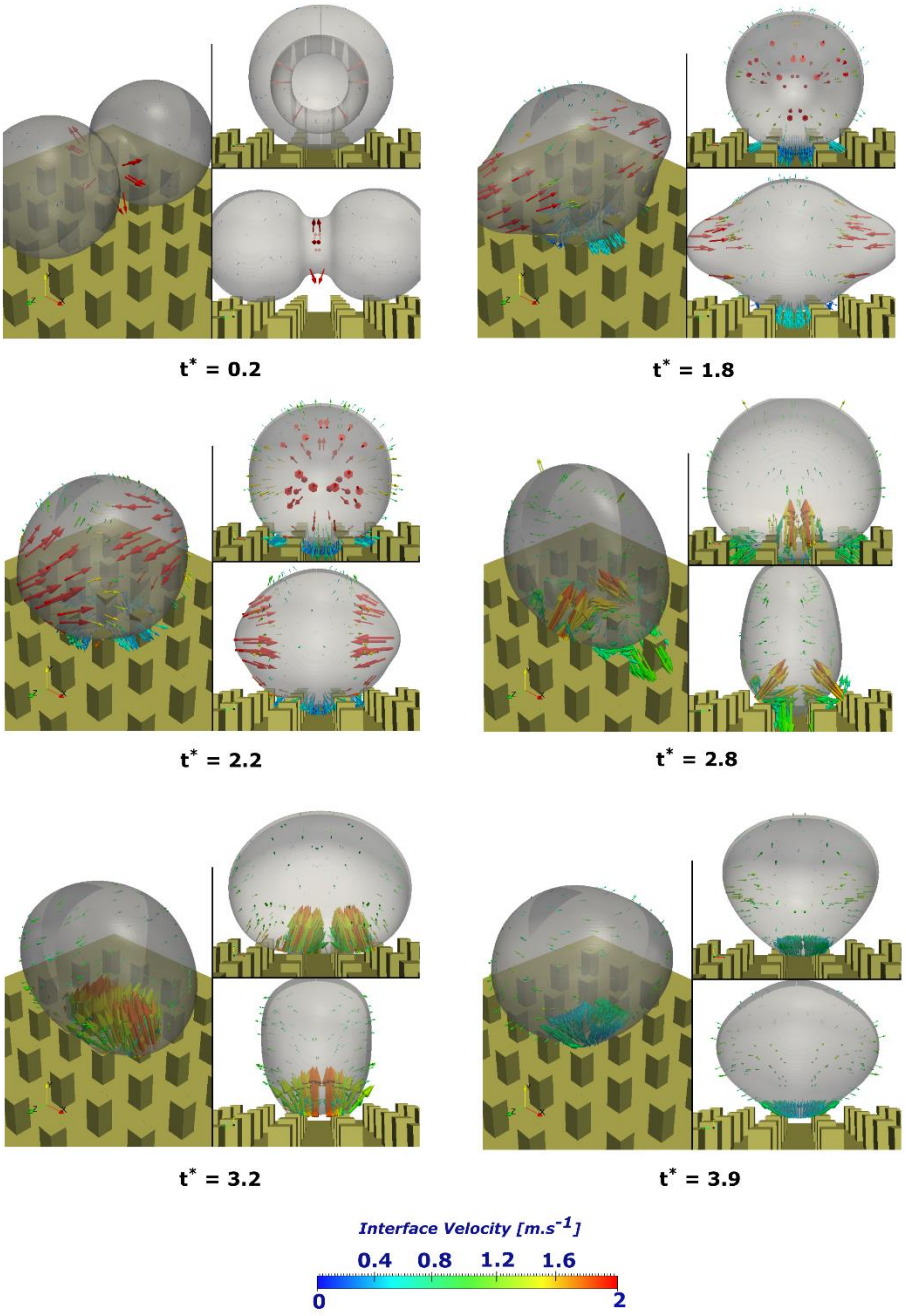

Figure 3-13: Interface velocity vectors of two merging microdroplets at different time steps ($R = 20\mu m$).

To validate the results, the non-dimensional jumping velocities of the merged micro-droplet on the heterogeneous superhydrophobic surface in the viscous and inertia dominated regimes were compared to the numerical results obtained on a homogeneous surface and also to experiment evidence[9].

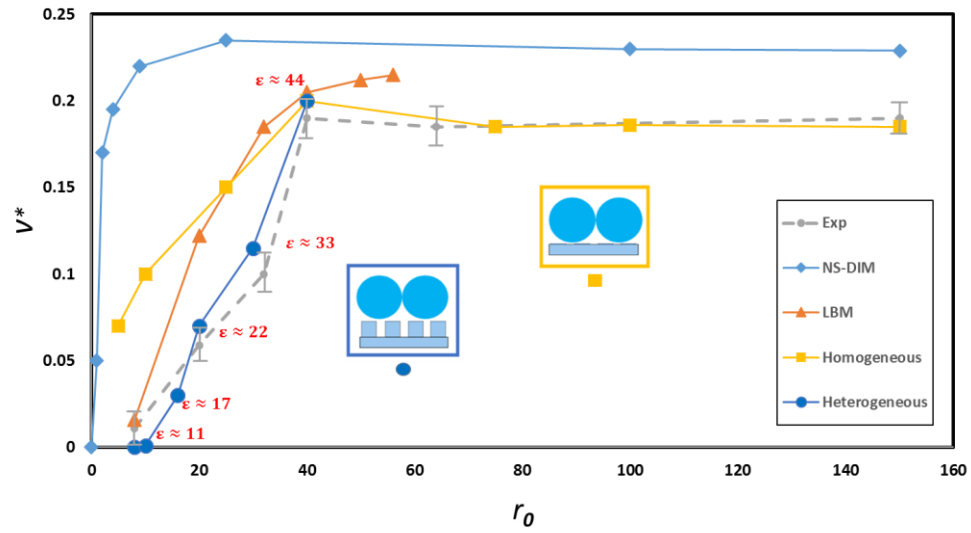

Figure 3-14: Comparison of jumping velocities of merged droplets in the present numerical simulation of coalescence-induced jumping on heterogeneous and homogeneous superhydrophobic surfaces with LBM [126], NS-DIM [117], and experiment [116].

As shown in Figure 3-14, the over-estimated jumping inertia of the merged drop on a homogeneous surface was not observed on the heterogeneous surface due to the presence of pillars. At $\varepsilon = 44$, both models converged to the same non-dimensional jumping velocity ($V^* \approx 0.2$). As the relative roughness fell below $\varepsilon = 44$, the two surfaces resulted in different degrees of deviation from the experiment. Due to the dominant effects of viscosity above the viscous cut-off, the jumping velocity of the coalescing droplets starts decaying. However, the jumping velocity was found to be relatively smaller on heterogeneous surfaces compared to that on homogeneous surfaces because of the interaction the droplet had with the surface cavities. This interaction can be strongly dissipative [27], [138] when the size of the droplet was similar to the size of roughness.

As shown in Figure 3-14, the numerical data from the heterogeneous model and the experimental results were similar at $\varepsilon = 22$. For lower radii, the jumping velocity decreased and fell below the velocities from the experimental data. The smallest jumping velocity obtained from the heterogeneous model was for the case of $\varepsilon = 11$ with a dimensionless jumping velocity of

0.008, which was less than half of that of the experimental results [116]. For smaller relative roughnesses (e.g., $\varepsilon = 8$), no droplet jumping was observed. This under-prediction of jumping velocity could be attributed to the presence of rather large roughness on the side walls of the pillars compared to the top surface, as shown in Figure 3-4. This can result in different wettabilities for the top and side surfaces, which was not considered in this study. Moreover, in order to preserve the structured mesh, the rounded corners of the micro-pillars were sharpened in the simulations, which could be a source of the deviation in the results for smaller size droplets.

To further understand and better quantify the effect of surface roughness on the dynamics of coalescence, we calculated the droplet volume fraction (%) that remained above the surface of the pillars during the coalescence (Figure 3-15.a). According to the data, the maximum penetration was encountered for $\varepsilon = 11$ with almost 8% of the initial volume penetrating into the cavities. Figure 3-15.b shows the maximum penetration depth of the micro-droplet versus the relative roughness. Three distinct regions were observed for this range of data: 1) The sticky region, where the coalesced micro-droplet remained on the surface due to the dominant effect of viscosity, 2) region with small inertia, where there was longer non-dimensional contact time and a smaller non-dimensional jumping velocity, and 3) region with a constant non-dimensional jumping velocity that can be approximated by the inertia scaling law.

The two possible mechanisms in penetration are the sag and de-pinning mechanisms [137], [139]. In the sag mechanism, the triple point is pinned at the pillar edges with a particular contact angle and a sagging interface above the air pockets. The depinning mechanism is when the contact angle exceeds the advancing contact angle, and the contact line slides downwards causing penetration. For cases below $\varepsilon = 44$, the dissipation of energy is associated with both the sag and de-pinning mechanisms. As shown in the Figure 3-15.b, the maximum volume penetration was

encountered for $\varepsilon = 11$ with approximately 8% of the liquid droplet volume inside the cavities. The penetration increased as the relative roughness decreased. However, for the relative roughness of $\varepsilon = 11$, no further penetration was observed. Lower still, the maximum penetration volume decreased to 7.5% for $\varepsilon = 8.8$.

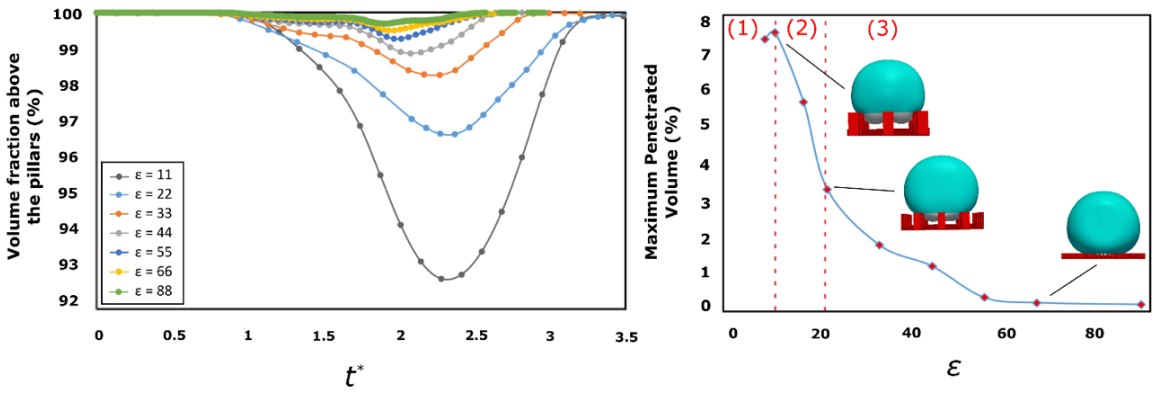

Figure 3-15 : (a) Time dependence of the droplet volume fraction (%) remaining on the surface during the coalescence, (b) Maximum penetration volume with respect to the relative roughness.

Another quantitative measure of the droplet–surface interaction is the maximum penetration depth of the micro-droplet into the cavities (H^*), measured from the pillar tip to the bottom of the penetrated liquid interface, as shown in Figure 3-16. Experimental measurement of the penetration depth via experimental study is not possible, but obtaining data from the simulations can give insight into this phenomenon. We observed that a gradual increase of penetration depth occurred with a reduction in the size of the micro-droplets up to $\varepsilon = 22$. However, the maximum penetration depth started decreasing again likely due to the ratio of pillar top area to the droplet size. Comparing the data for $\varepsilon = 11$ in Figure 3-15.b and Figure 3-16 shows that although the droplet had the maximum penetrated volume into the cavities, this does not necessarily represent the maximum penetration depth. As shown in Figure 3-16, the maximum penetration depth was obtained for $\varepsilon = 22$, which resulted in a relatively larger area in contact with the solid parts of the

surface (pillar walls and tops) and more than 90% penetration depth along the direction of the pillars. As the size of the droplet increased, the penetration dramatically decreased to the point that penetration was negligible for $\varepsilon = 66$.

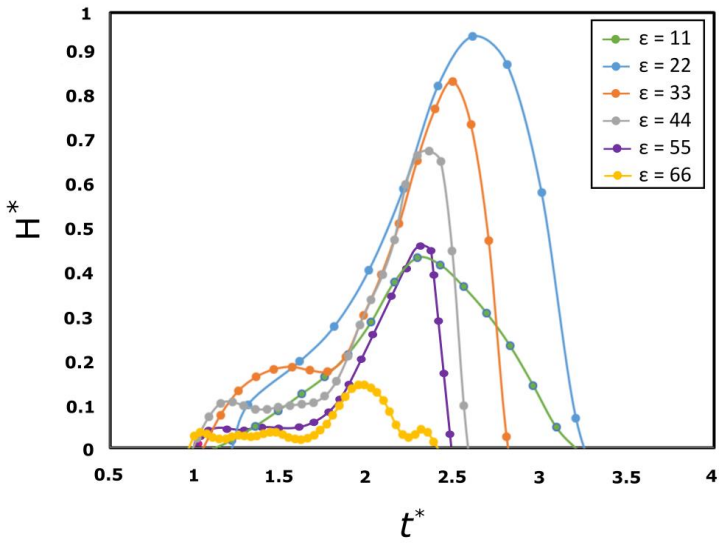

Figure 3-16: Time dependence of droplet normalized penetration depth for different relative roughness.

Figure 3-17 is a modification of Figure 3-4 after including the effect of surface roughness on the vertical velocity of the micro-droplet in the simulation. The cross signs at the end of each graph indicate the point in time when the droplet detached from the surface. The magnitude of the downward velocity of the merging micro-droplet increased as the size of the droplets become smaller. For droplets in the inertia-dominated regime ($\varepsilon = 55$ and $\varepsilon = 66$), the graphs were overlapping, showing similar non-dimensional jumping times and velocities. For $\varepsilon = 44$, a minor difference at the end of the graph was observed. As the droplet penetrated more during the coalescence, there was a lower center-of-mass velocity and consequently a smaller jumping velocity. This difference became more significant for cases with smaller relative roughnesses. In addition, there was an increasing temporal delay (Δt) for case with a relative roughness smaller than 55, causing the overall time duration of the coalescence followed by self-propelled jumping

to be higher. As the relative roughness decreased, it allowed the droplet to penetrate more into the valleys. A higher solid fraction in contact with the liquid dropled dissipated more of the energy and consequently took longer for the droplet to change its downward motion to the upward direction.

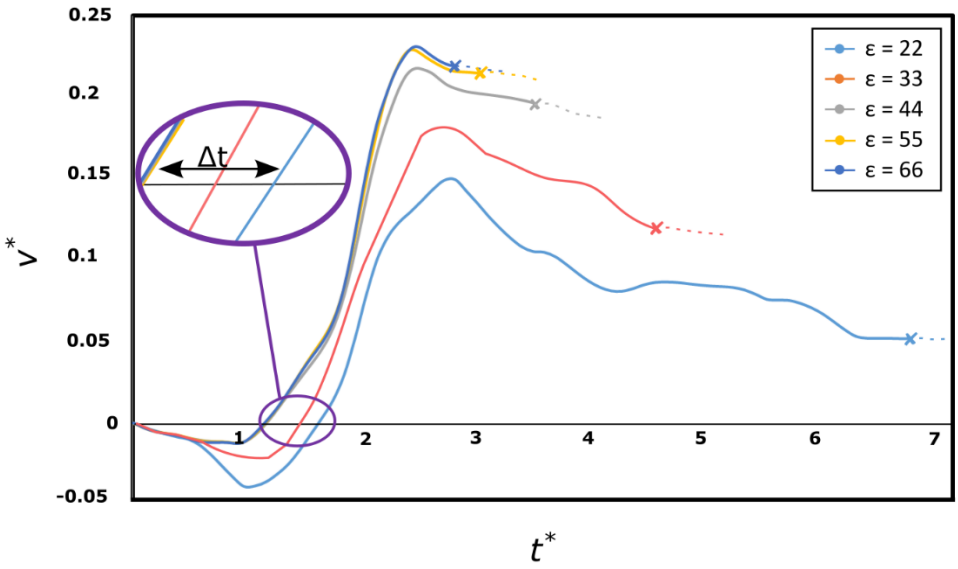

Figure 3-17: Time dependence of droplet vertical velocity for different relative roughnesses, with the cross signs indicating the jumping instant of the merged droplet.

For ε =44,55 and 66, the droplet left the surface at the same non-dimensional time and with the same non-dimensional jumping velocity ($V^* \approx 0.2$). As the size of micro-droplet decreased, the detachment from the surface took longer due to the larger viscous effects and deeper penetration into the surface cavities. For a relative roughness greater than 44, similar temporal behaviour was observed. For smaller relative roughness, the differences arose in the retraction stage after $t^* \approx 2.5$, when the micro-droplet started preparing to jump. For the case of $\varepsilon = 22$, the onset of jumping was significantly delayed comparing to the larger relative roughnesses ($\varepsilon = 44$) and previously revealed studies on smooth surface [117], [126]. This behaviour was mainly associated with the size of the droplet with respect to the size of the micro-pillars.

In this study, the two droplets were initially situated to be tangential to each other and tangential to the supporting surface composed of solid–air layers. Therefore, a quantitative diagram was constructed (Figures 3-18 and 3-19) as the result of examining the effect of initial location of the micro-droplets in a plane parallel to the surface on the jumping velocity of the merged micro-droplet. For each droplet size, multiple simulations were performed, which varied by the initial location of the merging micro-droplets (shown with red circles). The initialization of two micro-droplets was controlled in such a way that the tangent point of the interface of the two droplets lay at different locations with respect to the pillars. This way, the maximum and minimum jumping velocities were obtained at various relative roughnesses. Figure 3-18, shows the coalescence of two droplets on the heterogeneous surface when the initial location of the droplets was shifted by a quarter of the distance from the spacing between two adjacent pillars.

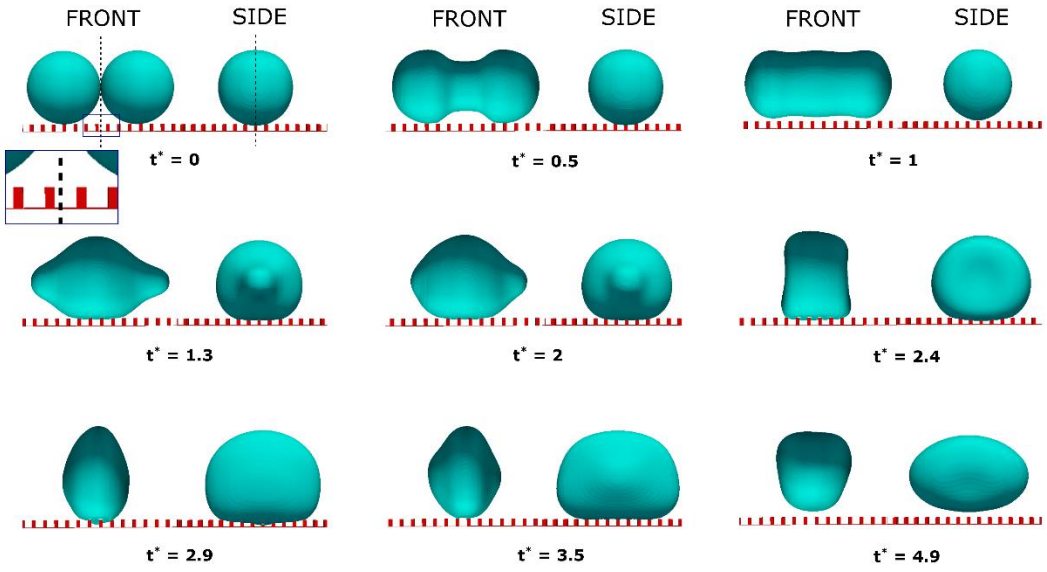

Figure 3-18: The coalescence of a twin micro-droplets (r_0 = 30 μm) for non-symmetrical initialization.

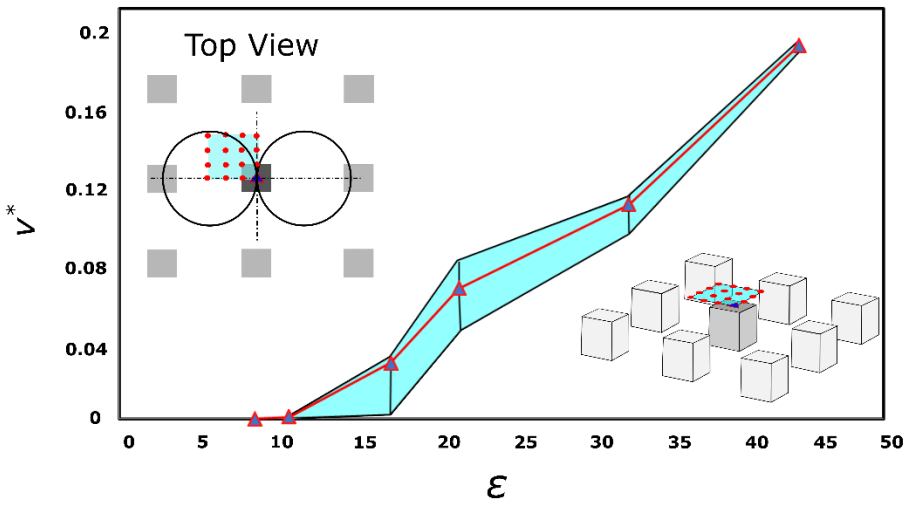

Figure 3-19: Variation of jumping velocity with the initial location of the two droplets on the textured surface, and the red dots are the location of the tangent point.

The blue shaded area in Figure 3-19 shows the non-dimensional jumping velocity for different locations over one period. The bold red line is the computationally obtained jumping velocity of the merged droplet, assuming the tangent point was located on the top center of a pillar. It is of note that the occurrence of coalescence in a symmetric condition (center of a pillar or spacing) does not necessarily provide the largest jumping velocity. As the size of the droplet increased, the difference between the maximum and minimum jumping velocities decreases. Similar behavior can be seen as the size of the droplet reduced below $20\,\mu m$ ($\varepsilon = 22$). For droplets larger than $20\,\mu m$ ($\varepsilon = 22$), the blue area decreased in size, and the variation in velocity approached unity, indicating that the change of the vertical velocity was independent of coalescence location. On the other hand, for droplets smaller than $\varepsilon = 22$, the change of jumping velocity was significantly higher, which showed the dramatic change of the jumping velocity as a function of coalescence location. This highlights the importance of coalescence location in this size range. In addition, for cases smaller than $\varepsilon = 16$ both jumping and sticky scenarios depending on the initial location of droplets were observed. It was found that for small relative roughness approximately

$\varepsilon < 16$, the outcome of the coalescence could be highly dependent on the initial location of the merging micro-droplets.

3.5 Summary and Conclusions

The process of droplet coalescence-induced jumping on homogeneous and heterogeneous superhydrophobic surfaces were modeled and analyzed using the 3D volume of fluid technique. In order to model the process of coalescence, a twin droplet were placed next to each other with their interfaces overlapping, which triggered the onset of their coalescence. It was shown that the model is capable of capturing the physics associated with the dynamics of the two micro-droplet coalescence showing self-jumping on superhydrophobic surfaces. This was done through accurate modelling of the micro-droplet interface curvature, the interface force calculations, and resolving the effect of air beneath the droplet on the heterogeneous superhydrophobic surface.

For modelling of the homogeneous superhydrophobic surface, a large static contact angle (176^o) for small wettability, and small hysteresis contact angle (2^o) for maximum mobility (i.e., adhesion) was used. A non-dimensional jumping velocity of 0.2 was obtained in the capillary-inertia dominated regime, which was in good agreement with the existing experimental data. However, the results were contradicted by the experiment [116] for droplet sizes in the viscous dominated regime. The source of this discrepancy was found to be from when the size of the droplet was comparable to the size of the surface roughness, which may result in penetration of the micro-droplet into the cavities, and it was not considered in the homogeneous surface model. It is clear that hierarchical micro/nano-heterogeneity is essential to demonstrate superhydrophobicity. Hence, the micro-topology was directly modeled as a series of micro-pillars resembling the substrate used in an experiment [116], and the effect of nano-topology was added

in the simulation using a dynamic contact angle model. Instead of a high static contact angle, the intrinsic contact angle of the material in contact with the micro-droplet was imposed on the outer surface of the micropillars. It was found that the over-predicted jumping velocity obtained from the homogeneous surface model was significantly damped and matched with the experiment on the heterogeneous superhydrophobic surface. Meanwhile, direct modelling of surface heterogeneity (i.e., solid–air composition) aimed at capturing the transition from a no-slip/ no-penetration condition to partial-slip with penetration at the walls when the triple points move over the air pockets.

In addition, the relevance of droplet size to the average surface roughness (relative roughness) was numerically quantified. The critical relative roughness of 44 found to be a threshold above which the smooth (i.e., homogeneous) surface assumption of the superhydrophobic surface may lead to a good agreement with the experimental data. However, for the cases below the critical relative roughness, the micro-droplets start penetrating into the spacing between the pillars. The penetration resulted in higher interaction with the surface cavities, longer contact time, and further dissipation of the jumping energy of the coalescing micro-droplet. A quantitative diagram was constructed to examine the change in initial location of the micro-droplets on the variation of the jumping velocity. It was found that as the relative roughness falls below the critical relative roughness, the initial location of the coalescing droplets can significantly change the outcome of coalescence. For droplets in size range of 10-15 μm, depending on their initial location in a plane parallel to the surface, both sticky and jumping mechanisms were observed after coalescence. It was apparent from the results that the direct modelling of surface roughness becomes crucial for the cases smaller than the critical relative roughness.

Chapter 4

Numerical Study of The Effect of Surface Wettability on Performance of the Spray Cooling Process

4.1 Abstract

The process of cooling caused by a water droplet contacting a surface has been extensively reported in the literature; however, the effect of surface wettability on the outcome of the cooling rate has yet to be analyzed. Due to optical limitations inside a liquid droplet, a three-dimensional (3D) computational fluid dynamics (CFD) model, including coupling between multiphase flow and the conjugated heat transfer module was developed to simulate the impact, spreading and transient heat transfer between a cold-water droplet and a heated surface. The total heat transfer results were calculated for both superhydrophobic and hydrophilic surfaces. The Navier-Stokes equation expressing the flow distribution of the liquid and the gas, coupled with the volume of fluid (VOF) method for tracking the liquid interface, was solved numerically using the finite volume methodology. The grid dependency test was examined for the 3D model, even though the convergence of the results was not exact. The 2 *mm* diameter water droplet with the Weber numbers 7, 25 and 62, which correspond to non-splashing regimes, were impinged onto two different surfaces. We showed that spray cooling on a superhydrophobic substrate was capable of improving the efficiency of the cooling process up to 40% compared to that of a hydrophilic

surface. Additionally, the critical Weber regime was obtained for the optimal heat transfer between the droplet and the two substrates.

Keywords: Cooling process, Superhydrophobic, Hydrophilic, Droplet impact

4.2 Introduction

The impingement of spraying cold drops onto heated dry walls and the associated heat transfer mechanism occurs in many engineering applications such as spray drying [140], internal combustion engines [141], spray coating [142], and spray cooling processes [143]. Spray cooling is a technique of increasing interest for cooling of electronic and mechanical elements and is characterized by a high rate of heat transfer, uniformity of heat removal, and small droplet impact velocity. In spray cooling process, a spray of small droplets on a heated surface is performed to remove significant amounts of energy by taking advantage of substantial convective heat transport through impinging droplets [140]. The ability of the liquid coolant to change phase in constant temperature, and at the same time, to dissipate heat in the form of latent heat makes the cooling process very interesting.

The fluid dynamics of impinging drops and the liquid film formation is complicated and requires fundamental study. In addition, the mechanism by which heat is removed during spraying is poorly understood, and because of its dependence on many parameters that are not easily varied dependently, predictive capabilities are quite limited.

In order to overcome complications mentioned above (droplet coalescence, liquid thin film formation, or phase change due to evaporation), a fundamental study of the spraying process, which is the impact of a single droplet onto a heated surface under non-fragmentation Weber threshold is carried out. Experimentally, it is shown that hydrophobic surfaces would have a higher

potential for removing thermal energy when are subjected to cooling spray, but not many detailed studies were carried for better understanding the mechanics associated with this phenomena.

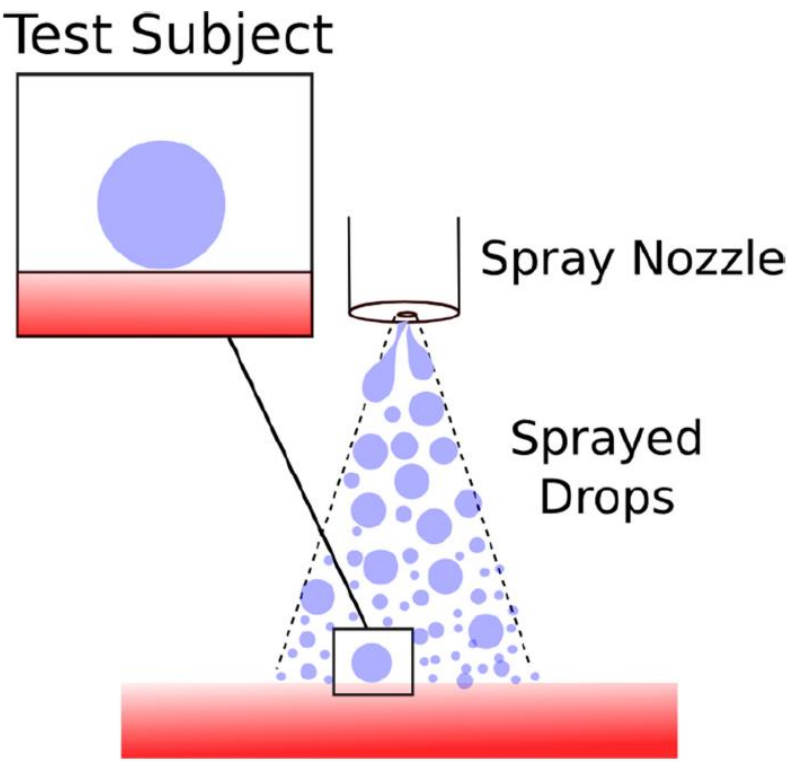

Figure 4-1: Schematic of sprayed drops in spray cooling process.

The primary objective of this study is to simulate the impact of a cold-water droplet on two preheated Aluminum substrates with infinitely thin hydrophilic and superhydrophobic coating through conjugated temperature gradient platform. We simulated 2.0 mm cold-water droplet as it impinges on the heated substrate, and measured the amount of thermal energy absorbed by the droplet after impact. The initial substrate temperature was set at 360°K; slightly below the boiling temperature to avoid complications associated with the evaporation or phase change. Impact velocities ranged from 0.5 to 1.5 $m.s$-1 to prevent fragmentation as the result of the impact. Fluid

flow and heat transfer during droplet impact were modeled using the Volume of Fluid (VOF) method.

4.3 Methodology

In this paper, a three-dimensional (3D), multi-region conjugate heat transfer module is developed to analyze the mechanism in which heat is transferred between solid and fluid. Separate governing equations for each region are solved depending on their phase and the boundary interface.

4.3.1 Governing Equations

In the fluid region, the Navier-Stokes equation expressing the flow distribution of the liquid and the gas, coupled with the Volume of Fluid (VOF) method for tracking the interface between the liquid and the gas is solved numerically using finite volume methodology. In VOF method [100], tracking of the interface is modeled by solving continuity equation for one of the two phases in each computational cell at every time step. The governing equations for the mass, momentum and energy balance in each fluid phase and on the interface, can be expressed as,

$$\nabla \vec{V} = 0 \tag{4-1}$$

$$\frac{\partial \rho \vec{V}}{\partial t} + \nabla . \left(\rho \vec{V} \vec{V}\right) = -\nabla p + \nabla . \left(\mu . \nabla \vec{V}\right) + \left(\nabla \vec{V}\right) . \nabla \mu - g . x \nabla \rho + F_b \, , \tag{4-2}$$

$$\frac{\partial \rho C_p T}{\partial T} + \vec{V} \nabla . \left(\rho C_p T\right) = \nabla . (k \nabla T) \tag{4-3}$$

where T is temperature, t is time, $\vec{V}$ is the velocity vector, p is the pressure, F_b is the body force, and a is the volume fraction which is used to calculate the viscosity (μ), density (ρ), heat capacity *(Cp)* and thermal conductivity (k) as weighted averages based on the distribution of α,

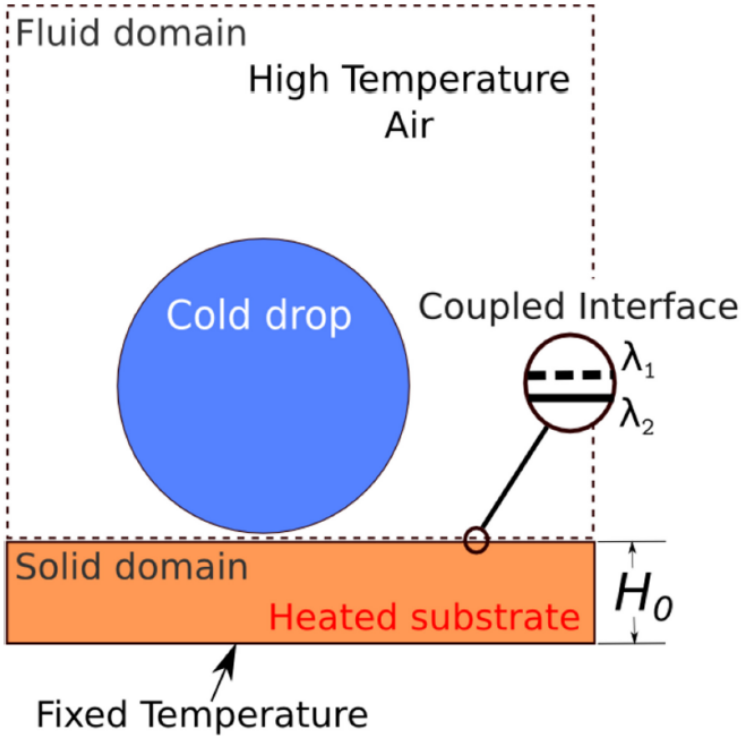

Figure 4-2: 3D computational domain, cold droplet, and the H_0=3 *mm* the thickness of the heated aluminum substrate. λ_1 & λ_2 are the coupling interfaces.

$$\rho = \alpha\rho_d + (1-\alpha)\rho_g, \tag{4-4}$$

$$\mu = \alpha\mu_l + (1-\alpha)\mu_g \tag{4-5}$$

$$k = \alpha k_l + (1-\alpha)k_g \tag{4-6}$$

$$\rho C_p = \alpha\rho_l C_{pd} + (1-\alpha)\rho_g C_{pg} \tag{4-7}$$

where the subscripts *l* and *g* denote the liquid and gas phases, respectively. In VOF method, the phase fraction scalers tracer α takes values between 0 and 1. When a cell is empty with no traced fluid inside, the value of *a* is zero; when the cell is full, *a* is equal to 1; and when there is a fluid interface in the cell, $0 < \alpha < 1$. As the interface deforms with time, the evolution of fluid is governed by the transport equation,

$$\frac{\partial \alpha}{\partial t} + (\vec{V}\nabla)\alpha + \nabla.\left(\vec{V}_r \alpha(1-\alpha)\right) = 0, \tag{4-8}$$

where $\vec{V}_r$ is the vector of relative velocity, designated as the compression velocity introduced by Rusche [101] to facilitate a sharp interface between phases,

$$\vec{V}_r = \vec{n}\max\left[Ca\frac{|\emptyset|}{|S_f|}, \max\left(\frac{|\emptyset|}{|S_f|}\right)\right] \tag{4-9}$$

where $Ca, n, \emptyset$ and S_f, are the compression coefficient, unit normal flux, face volume flux and cell face area vector respectively. The interface unit normal $\vec{n}$ is computed by taking the gradient of smoothed volume fraction α at the cell faces.

$$\vec{n} = \frac{\nabla\alpha}{|\nabla\alpha| + \delta}, \tag{4-10}$$

where δ is a small number in order to stabilize the calculation in regions outside the transition region where $\nabla\alpha \to 0$. In this study, $\delta = 10^{-8}$ is used for the entire simulations. The main benefit of such formulation is in the possibility of capturing the sharp interface region. The continuum surface force method [69] is used to model surface tension as a body force F_b that acts only on interfacial cells,

$$\vec{F}_b = \sigma_d k \nabla\alpha, \tag{4-11}$$

where σ_d is the surface tension, and k is the mean curvature of the free surface, calculated by,

$$k = -\nabla.\left(\frac{\nabla\alpha}{|\nabla\alpha|}\right). \tag{4-12}$$

The pressure-Implicit with splitting operators (PISO) scheme in transient flow is used for the pressure-velocity coupling. The wettability effects at the substrate are taken into account by using

the dynamic contact angle which is assumed to be a function of the contact line velocity. The Kistler's correlation [102] is used to calculate the dynamic contact angle in each time step,

$$\theta_d = f_H[Ca + f_H^{-1}(\theta_A, \theta_s, \theta_R)], \tag{4-131}$$

where, f_H is the Hoffman function and is defined as,

$$f_H = \cos^{-1}\left\{1 - 2\tanh\left[5.16\left[\frac{x}{1+1.31x^{0.99}}\right]^{0.706}\right]\right\}. \tag{4-14}$$

in the above equation, the equilibrium contact angle s is replaced by either the advancing contact angle, θ_A, or the receding contact angle, θ_R, depending on the direction of the velocity vector at the contact line or the static contact angle, θ_s, if the contact line velocity is zero. It is worth mentioning that the no-slip models such as Kistler's correlation [102] have been extensively used to investigate droplet dynamics [103], [104]. In addition, it was shown that this model is capable to capture the relevant physics of droplet-substrate interaction and provides good agreement with experiment [144].

The heat transfer in the solid substrate can be modeled by solving the Laplace equation for the pure conductive heat transfer in a solid substrate:

$$\rho_s C_{ps} \frac{\partial T_s}{\partial t} = \vec{V}.(k_w \vec{\nabla} T_s) \tag{4-15}$$

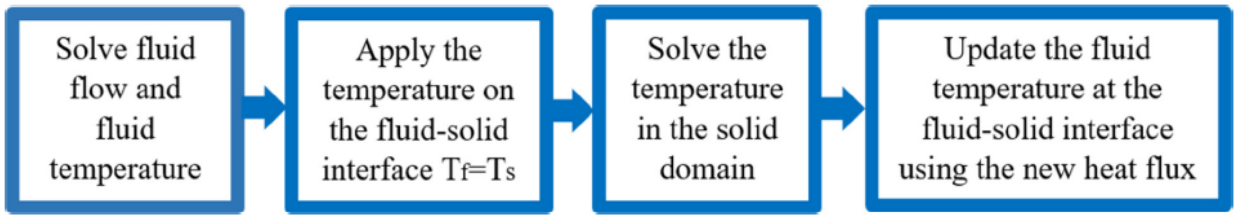

Figure 4-3: Iterative solution procedure of domains coupling.

Table 4-1: Material properties

	$\rho\left(\frac{kg}{m^3}\right)$	$K\left(\frac{kg.m}{s^3.T}\right)$	$C_p\left(\frac{m^2}{s^2.T}\right)$	$v\left(\frac{m^2}{s}\right)$
Air	1	0.02	1,000	1.78×10^{-5}
Water	1,000	0.6	4,200	1.0×10^{-6}
Alumin	2,700	205	900	-

The lower surface of the substrate is subjected to fixed temperature boundary condition (360°K). The substrate density, thermal conductivity, and heat capacity are given in Table 1.

4.3.2 Regions Coupling

There are two approaches for solving multi-region problems; monolithic and partitioned. The monolithic approach seeks to define a series of partial differential equations (PDEs) that govern the entire fluid and solid domain and then discretize the entire domain. While theoretically simple, this approach is difficult to implement due to the difference in the mathematical and numerical properties of the two domains. On the other hand, the partitioned approach seeks to utilize existing fluid and solid solutions and couple these solvers at the interface of the two domains. The fluid solver uses a separate set of equations, variables, and mesh than the solid solver. The coupling happens at the boundary (λ_1 & λ_2) where the temperature of the fluid updates the boundary of the solid which is then solved for to determine the gradient temperature at the interface boundary. This updated boundary is then used to solve the fluid domain. As this method solves different sets of matrices, parallelism of the computation is more efficient. In this paper, the portioned coupling method was used to couple solid and fluid domains. Considering the governing equations for each domain, the temperature and heat fluxes should be equal at the interface,

$$T_f = T_s$$
$$k_f \nabla T_f = k_s \nabla T_s \quad (4\text{-}16)$$

where, T_f and T_s are the temperatures of fluid and solid domains, respectively. Boundary conditions are applied on boundary patches. Each domain solving module is placed inside a separate loop to meet the coupled convergence through a global iterative process.

Validation of the solver is performed using one-dimensional, steady state situation where heat is transferred between gas and wall to ensure the calculation of the coupled interface is correct [145]. It is a wall, with hot and warm air flowing next to it, which results in a temperature gradient in the wall. In a 1D problem, heat transfer occurs only in one direction. The results obtained from the model and the analytical study were in close agreement with less than 1% divergent.

4.3.3 Geometrical Configurations and Meshing

The computational domain size of 16 mm × 20 mm × 14 mm is used for the 3D simulation of the impinging droplet onto a heated substrate. The domain is discretized by about 1 million, 2 million, and 3.5 million Hexahedral mesh with adaptive refinement at the interfacial cells. The mesh dependency test is performed based on the jumping velocity of a droplet on a superhydrophobic surface. As the change of droplet jumping velocity in 3.5 million and 2 million mesh was minimal, the domain composed of 2 million mesh is applied in this study. The cells are refined so to have 60 cells per diameter of the droplet before impingement. The substrate thickness of 3 mm is extracted from the domain. The exterior surface of the solid region that is in common with fluid is coated with hydrophilic (θ_s =15°) and superhydrophobic (θ_s =180°) materials. The material properties of the substrate are given in Table 1.

4.4 Results and Discussion

In order to study the effect of surface wettability on the transient heat transfer and total heat transfer between the droplet and the surface, the impingement of water droplets onto two surfaces with different surface wettability was carried out.

Figure 4-4 shows the time lapse of the droplet dynamics during the impingement on infinitely thin superhydrophobic and hydrophilic coatings on aluminum substrates. As it was reported before and confirmed in this study, the hydrodynamics of the liquid drop changed according to the wettability of the surface. Because of the extremely low-surface energy of the superhydrophobic coating, the droplet detached in a certain amount of time after impingement, which is called droplet "contact time" [146]. According to Richard et al. [146], contact time is not a function of impact velocity. Instead, it is a strong function of the surface energy, the liquid density, the droplet size, and the liquid surface energy. For the sake of simplicity in the analysis, the physical times of all simulations were bounded according to the droplet contact time on the superhydrophobic surface. Previous research showed that the contact time does not depend on the Weber number [11]. For droplets as large as 2 *mm* in diameter, the contact time scaled with the inertia-capillary timescale $\left(\tau = \sqrt{\frac{\rho R^3}{\sigma}}\right)$ and for high deformation impact (non-splashing regime) on a superhydrophobic surface, the contact time was approximated as $t_c = 2.3R$.

As shown in Figure 4-4.a, the droplet spread on the hydrophilic substrate and covered a higher surface area compared to the same size droplet impinging on the superhydrophobic surface. According to the law of conductive heat transfer, higher surface area contact should result in a higher heat transfer rate between the two media.

On the superhydrophobic surface, the droplet spread up to its maximum spreading diameter. At the same time, the kinetic energy of the impact transformed into surface energy in the form of potential energy. At some point, the droplet releases the excess of potential energy and starts recoiling. Once the recoiling stage is over, the droplet completely rebound and detach from the substrate. The temperature of the droplet and surface changes according to the heat transfer rate between the two media during the contact event.

In order to measure and compare the total heat transfer between the hydrophobic and hydrophilic aluminum surfaces, the total energy of the droplet before and after impact was calculated for both surfaces (Figure 4-5). Interestingly, the total energy transferred to the superhydrophobic surface was higher than that transferred to the hydrophilic surface, despite the smaller contact area during the impingement event.

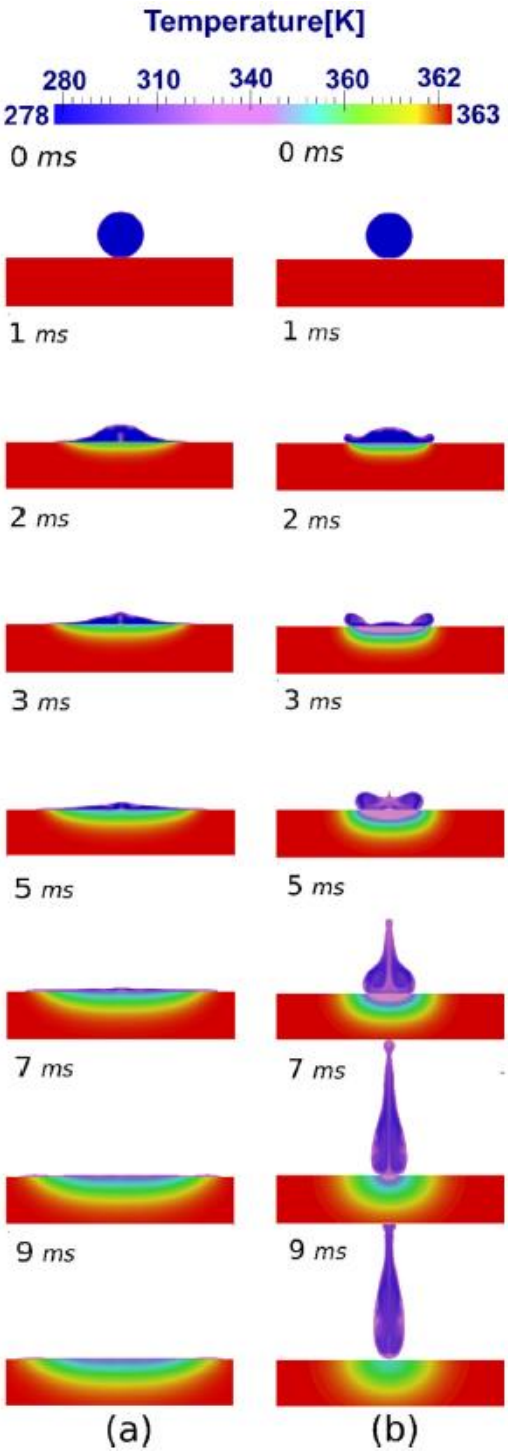

Figure 4-4: Impact of 2 *mm* water droplet on (a) hydrophilic and (b) superhydrophobic heated aluminum substrate, $\boldsymbol{V_d}$ = 1 m.s^{-1}.

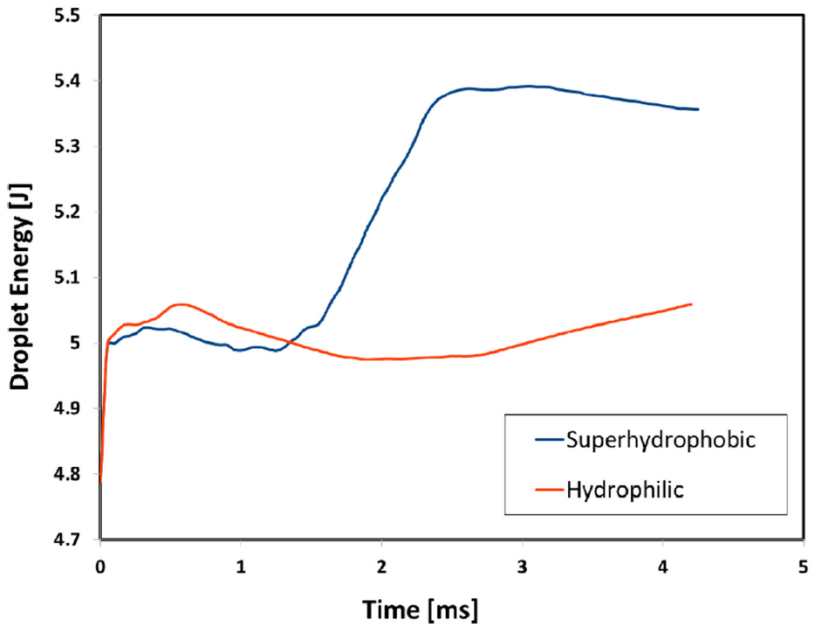

Figure 4-5: Energy transfer between the droplet and the substrates, $\boldsymbol{V_d}$ = 1 m.s^{-1}.

We observed intense mixing on the periphery of the droplet lamella on the superhydrophobic surface during its maximum spreading stage (Figure 4-6), which resulted in a higher heat transfer rate between the droplet and the heated aluminum substrate. The surface heated the lower volume of droplet lamella that was initially in contact with the heated aluminum, and, due to a high mixing intensity, the upper and bottom volumes recirculate until a thermal equilibrium condition was nearly met when the droplet detached from the substrate.

The dynamics of the droplet on the hydrophilic surface was different. The mixing associated with the recoiling stage was not observed in the droplet lamella. The droplet spread and the upper volume of the droplet temperature was raised gradually due to convective heat transfer with air and conduction inside the droplet. Figure 4-7 shows the total energy enhanced by the droplet at the time of detachment for various Weber numbers by changing the terminal velocity of the impact.

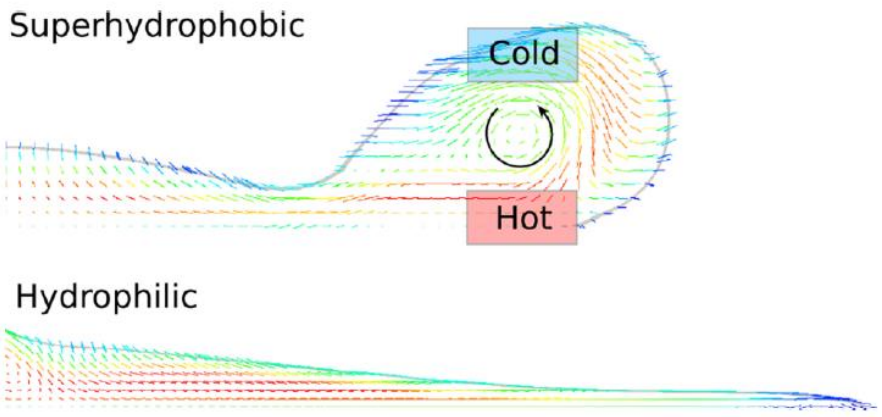

Figure 4-6: High-intensity mixing of liquid lamella and higher heat transfer rate of superhydrophobic comparing hydrophilic surface, $\boldsymbol{V_d}$ = 1 m.s^{-1}.

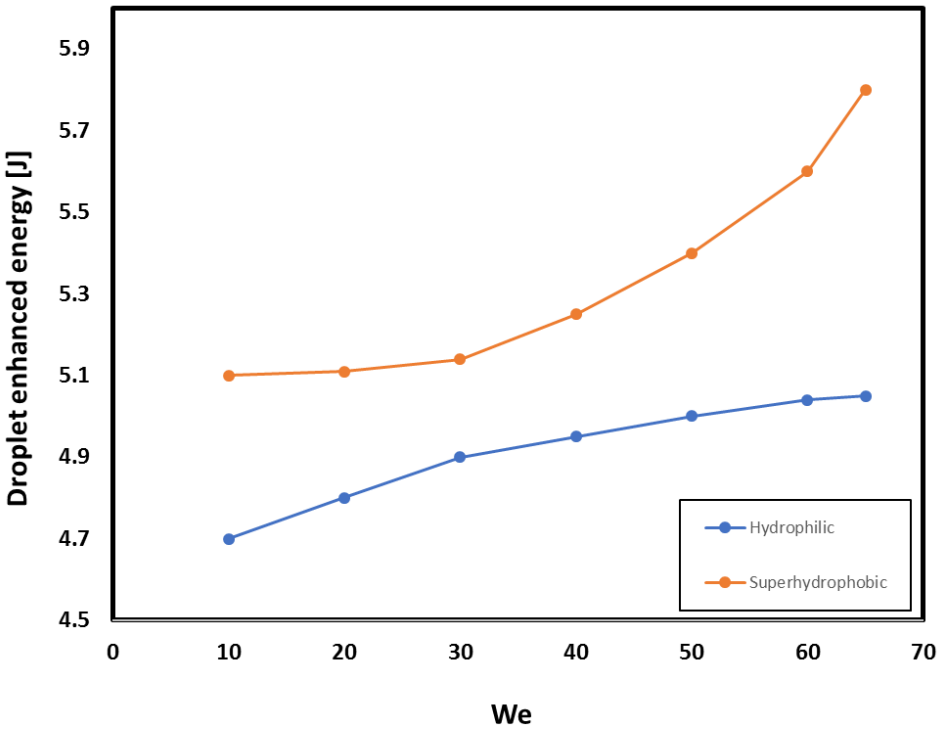

Figure 4-7: The thermal energy of 2 *mm* droplet at the time of detachment for different Weber numbers.

Although the Weber number was reported not to change the contact time of the droplet on the superhydrophobic substrate, We found that it can have a significant effect on the mixing intensity,

and consequently, the amount of heat transferred to the solid substrate and the liquid droplet. As the dimensionless Weber number was increased, the droplet obtained more thermal energy from the surface. The total amount of absorbed energy was greater on the superhydrophobic surface than on the hydrophilic surface. The best cooling performance in the non-fragmentation regime was observed on the superhydrophobic surface for the Weber number near the fragmentation threshold.

4.5 Conclusions

The conjugate temperature gradient multi-phase model was developed to simulate the impact of a cold-water droplet on a heated aluminum substrate with infinitely thin coatings. We showed that the spray cooling effect on the superhydrophobic substrate improved the efficiency of the process up to 40% compared with spray cooling on a hydrophilic surface. This efficiency increase was associated with a high mixing intensity of the liquid inside the droplet lamella, which increased the heat transfer rate with the substrate. Additionally, we found that the Weber number has a significant impact on the cooling rate of the surface.

Chapter 5

Icephobic Performance of Superhydrophobic Coatings: A Numerical Analysis

5.1 Abstract

Understanding the mechanism of cloud-sized particles impact and freezing is crucial to find viable solutions to prevent ice accumulation on critical aerodynamic surfaces such as aircraft wing or nacelle. It has been reported that superhydrophobic surfaces (SHS) have promising anti-icing properties due to their excellent water-repellent characteristics. However, the anti-icing performance of such surfaces has not been fully understood. A multi-region multiphase flow solver including phase change has been employed to model the icing of a micro-droplet as it impinges on a superhydrophobic substrate with a given thickness, texture, and solid material thermal properties. The Navier-Stokes equation expressing the flow distribution of the liquid and the gas, coupled with the volume of fluid (VOF) method for tracking the liquid-gas interface, was solved numerically using the finite volume methodology. The superhydrophobic morphology is modeled through series of micro-structured arrays with squared cross-sectional pillars. As such, the thermal contact resistance is directly modeled by the inclusion of air pockets underneath the micro-droplet. Consequently, the direct effect of surface topology and thermal properties on droplet maximum spreading diameter, penetration to the surface asperities, contact time, and the freezing onset have been investigated.

5.2 Introduction

Water droplet freezing has received increased attention in numerous fields more specifically in the aviation industry to analyze the ice accretion mechanism due to the impact and solidification of cloud droplets. The resulting in-flight icing can take place on an aircraft wing, tail, engine or instruments leading to decrease the aerodynamic performance which could result in a lack of control or loss of thrust and constitute a major safety and security issue. Hence, Understanding the physics governing the process of water droplet freezing on various surfaces would be necessary to develop more efficient anti and de-icing solution. Assuming a similar surface energy characteristics of ice and water, it has been a standard approach to correlate the surface hydrophobicity to the ice adhesion. Consequently, Superhydrophobic surfaces (SHSs) have been considered as suitable icephobic candidates for their extraordinary capability of reducing adhesion with water [7], [147], [147]–[149] by minimizing droplet contact time and consequently reduce or eliminate ice formation [150], [151]. Even though many experimental [36], [152], [153], numerical [63], [154] and analythical [89] studies have focused on the impact and freezing of milliliter size droplets on superhydrophobic surfaces, less is known to investigate the behavior of micro-drops on such surfaces and to consider the direct effect of surface asperities in their models. Because of the smaller mass of micro-droplets, freezing occurs in much shorter time which can deteriorate ice-phobicity of the surface faster. It has been found that there are several parameters directly or indirectly control the ice-phobicity of a surface. For instance, in rapid cooling process Qing Xu et al. [155] found that the material properties of the substrate may change the retraction time and the spreading diameter of the retracting droplet. Huang et al. [156] studied freezing of water droplets on the copper surface for a broad range of surface temperatures. They showed that freezing time

significantly changed by the wettability and the temperature of the surface. Since the freezing of water droplets is a heat transfer driven process, several numerical simulations have been carried out [63], [157]. Blake et al. [158] studied the conduction of the heat inside a millimeter-size droplet when the surface was subjected to a constant surface temperature. However, the constant temperature boundary condition in their model cause the droplet to solidify faster than actual droplets. Schremb et al. [159] recently presented a computational model based on a volume of fluid method for a non-isothermal two-phase flow applying for the simulation of water droplet impingement on a dry cold surface. It was shown that the amount of heat transferred between the fluid and the wall is affected by the contact time and the area available for heat transfer, which is determined by the impact conditions. In addition, reducing roughness can increase the free energy barrier for heterogeneous nucleation which results in significant freezing delay. Hao et al. [160] focused on the freezing delay and the freezing time of sessile droplet on smooth, micro-structured and micro/nanostructured surfaces. Their experimental data and theoretical analysis showed that the surface roughness plays a crucial role in nucleation time. In addition, they found that smooth surfaces with roughness smaller than the size of the critical ice nuclei have a larger freezing delay than superhydrophobic surfaces with hierarchical structures. Visser et al. [161] studied water microdroplet impact at velocities ranging from 1 to 100 m/s on the smooth solid surface for droplet diameters ranging from 12 to 100 μm which can cover the transition between surface tension and viscosity-dominated spreading of the droplet. They illustrated the importance of thin boundary layer over the surface in which majority of viscous dissipation occurs. The timescale for micro-droplet impact spreading on the superhydrophobic surface is very short, on the order of microseconds which makes it difficult to visualize experimentally. Moreover, because of the optical limitation inside the droplet, experimental analysis of small micro-droplets (i.e., diameter

range between 40-100 µm) impact on rough surfaces is complicated to control. In addition, understanding the effect of surface topology and thermal properties of the substrate are of utmost importance for fabrication of functional ice-phobic surfaces. Therefore, in this study, we employed a 3D computational analysis to evaluate the effect of two different substrate materials accompanied with surface roughness on the freezing process of 30µm droplets impingement.

5.2.1 Framework

The objective of this study is to develop a three-dimensional conjugate heat transfer (CHT) module based on OpenFOAM platform, to simulate the complicated thermal process of a cloud-sized droplet icing phenomena on superhydrophobic surfaces. This procedure is based on a continuous exchange of boundary conditions at fluid/solid including water-solid and air-solid interfaces. It couples together the Navier-Stokes flow solver, the Eulerian droplet impingement module, a liquid to solid phase change module and the solid conduction module simultaneously.

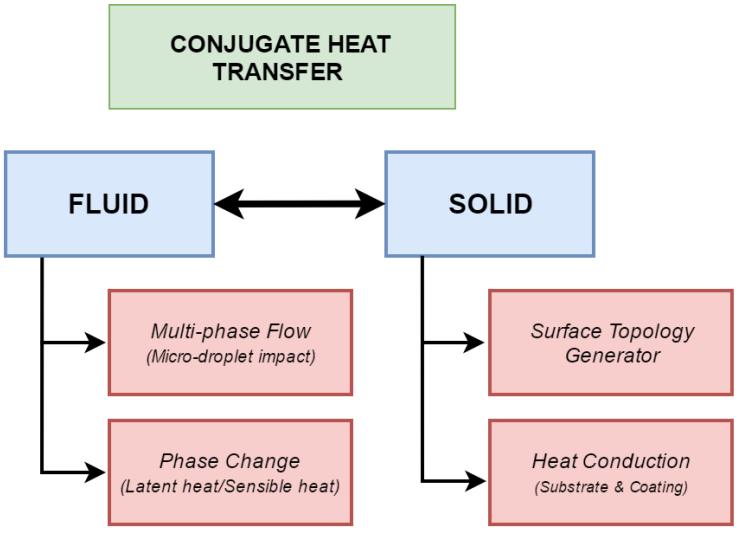

Figure 5-1: Hierarchical overview of the implemented solver

The conjugate heat transfer method iteratively solves the thermal interactions between fluid and solid domains. The coupled method can directly calculate the heat transfer loads at fluid-solid interfaces instead of using empirical correlations, and its results are more accurate than empirical methods if the flow field is refined enough.

5.2.2 Governing equations

The model is formulated to simulate the impact of a micro-droplet on a superhydrophobic substrate at the instant the droplet comes into contact with the surface and proceeding until the onset of freezing is captured. Formulation of transport equations for incompressible, laminar flow of Newtonian fluids, phase change, and conjugate heat transfer with the solid surface are as described in the following section.

Continuity equation

In the freezing of a micro-droplet, mass transfer from one phase to another is a local phenomenon and does not change the global continuity equation,

$$\frac{\partial \rho}{\partial t} + \vec{\nabla}.\left(\rho \vec{V}\right) = 0 \qquad (5\text{-}1)$$

Energy Equation

The heat transfer between water, ice, gas and the substrate is addressed using an energy conservation equation based on the enthalpy formulation as follow,

$$\frac{\partial \rho H}{\partial t} + \vec{\nabla}.\left(\rho \vec{V} H\right) = \vec{\nabla}.\left[\vec{\nabla}(kT)\right] \qquad (5\text{-}2)$$

where ρ is the density, k the thermal conductivity, V0 and ΔT are the characteristic velocity and temperature, respectively. Since the Eckert number ($Ec = V_0^2/C_p\Delta T << 1$), representing the ratio between the kinetic energy to the enthalpy is too small, the viscous dissipation is neglected. The enthalpy of the material is computed as the sum of the sensible heat (h) and the latent heat (ΔH),

$$H = \underbrace{h_{ref} + \int_{Tref}^{T} C_p dT}_{h} + \underbrace{\alpha\gamma L_f}_{\Delta H}, \tag{5-3}$$

where, h_{ref} is the reference enthalpy which is zero for pure water, T_{ref} , the reference temperature when the phase change starts. In order to account for phase change during the freezing, the specific sensible enthalpy is extended by the latent heat of fusion L_f . This latent heat should be multiplied by the liquid-solid fraction, γ, within the computational cells and this fraction satisfies:

$$\gamma = \begin{cases} 0 & ice \\ 1 & water \end{cases} \tag{5-42}$$

Therefore, the energy equation can be formulated in terms of the temperature by inserting in Eq.2,

$$\frac{\partial(\rho C_p T)}{\partial t} + \vec{\nabla}.(\rho C_p \vec{V} T) = \vec{\nabla}.\left[\vec{\nabla}(kT)\right] \underbrace{-L\left[\frac{\partial \rho\gamma}{\partial t} + \vec{\nabla}.\left(\rho\vec{V}\gamma\right)\right]}_{S_H} \tag{5-5}$$

where, S_H is a source term accounting for the phase change. There is a special treatment to be performed when solving the enthalpy formation (Eq.2) which requires a scheme for the enthalpy to be carried out at each outer iteration of the energy equation.4 This scheme is used to ensure boundness and convergence. In the present study, to avoid the classical numerical ad hoc treatment for solving the energy enthalpybased equation and due to the severe transition for water freezing, an approximate analytical function of the water-ice fraction is proposed and expressed as follows:

$$\gamma = \frac{1}{2}[1 + \tanh(k_l(T - T_{ref}))] \tag{5-6}$$

Where k_l is an adjusting parameter indicating the severity of phase transition. The liquid fraction in the freezing liquid dependenting on temperature indicates that phase change can occur in a very narrow temperature range as for water or any pure substance. Heat transfer within solid domain can be described by Fourier's law defining the conductive heat flux, q, proportional to the temperature gradient ($q = -k.\nabla T$). For a time-dependent problem, the temperature field in an immobile solid is governed by the following heat equation,

$$\rho_s C_{ps} \frac{\partial T_s}{\partial t} = \vec{\nabla}.(k_w \vec{\nabla} T_s) \tag{5-73}$$

Liquid Fraction Equation

The liquid-gas interface is implicitly determined by the field volume fraction for every computational cell. The advection of interface is based on an existing multiphase solver (interFoam) which utilizes Volume of Fluid (VOF) [100], an Eulerian interface capturing method. The transport equation accounting for the advection and compression of the interface is as follow,

$$\frac{\partial \alpha}{\partial t} + (\vec{V}\nabla)\alpha + \nabla.\left(\vec{V}_r \alpha(1-\alpha)\right) = 0, \tag{5-8}$$

where $\vec{V}_r$ is the vector of relative velocity, designated as the compression velocity introduced by Rusche [101] to facilitate a sharp interface between phases,

$$\vec{V}_r = \vec{n}\max\left[Ca\frac{|\emptyset|}{|S_f|}, \max\left(\frac{|\emptyset|}{|S_f|}\right)\right] \tag{5-9}$$

where $Ca, n, \emptyset$ and S_f, are the compression coefficient, unit normal flux, face volume flux and cell face area vector respectively. The interface unit normal $\vec{n}$ is computed by taking the gradient of smoothed volume fraction α at the cell faces.

$$\vec{n} = \frac{\nabla\alpha}{|\nabla\alpha| + \delta}, \tag{5-104}$$

where δ is a small number in order to stabilize the calculation in regions outside the transition region where $\nabla\alpha \to 0$. In this study, $\delta = 10^{-8}$ is used for the entire simulations. The main benefit of such formulation is in the possibility of capturing the sharp interface region. The continuum surface force method [69] is used to model surface tension as a body force F_b that acts only on interfacial cells,

$$\vec{F}_b = \sigma_d k \nabla\alpha, \tag{5-11}$$

where σ_d is the surface tension, and k is the mean curvature of the free surface, calculated by,

$$k = -\nabla.\left(\frac{\nabla\alpha}{|\nabla\alpha|}\right). \tag{5-12}$$

The physical properties of the liquid, gas, and ice such as viscosity, μ, thermal conductivity, k, heat capacity, Cp, and the density, ρ, of the mediums are calculated based on the weighted average of, α, in the computational domain,

$$\emptyset = \alpha(\gamma\emptyset_l + (1-\gamma)\emptyset_s) + (1-\alpha)\emptyset_g \quad where, \quad \emptyset \in \{k, C_p\} \tag{5-13}$$

$$\emptyset = \alpha\emptyset_l + (1-\alpha)\emptyset_g \quad where, \quad \emptyset \in \{\rho\} \tag{5-14}$$

where, the subscripts l and g denote the liquid and gas phases, respectively. In VOF method the phase fraction scalers tracer, α, takes values between 0 and 1. When a cell is empty with no traced fluid inside, the value of α is zero; when the cell is full, α is equal to 1; and when there is the liquid interface in the cell, $0 < \alpha < 1$.

Momentum Equation

The momentum equation expressing flow distribution of the liquid and the gas, coupled with the Volume of Fluid (VOF) method for tracking the interface between the liquid and the gas are solved numerically using the following equation,

$$\frac{\partial \rho \vec{V}}{\partial t} + \vec{\nabla}.(\rho \vec{V}\vec{V}) = -\vec{\nabla}p + \nabla.\left(\mu \nabla \vec{V}\right) + \vec{F}_b + \underbrace{\alpha\beta\vec{V}}_{S_V} \tag{5-15}$$

where, V is the velocity vector, p is the pressure, $\vec{F}_b$ is the body force, α is the volume fraction and S_v is the source term accounting for the viscosity change of the liquid droplet as it freezes. Carman-Kozney formulation used to adjust the coefficient β from zero for liquid to a large value as the liquid freezes,

$$\beta = \frac{\chi(1-\gamma)^2}{\gamma^3 + \epsilon} \tag{5-16}$$

where, ϵ is a small value to avoid division by zero.

5.2.3 Surface Wettability

The wettability or hydrophobicity effect at the substrate is taken into account by implementation of Kistler's dynamic contact angle model.13

$$\theta_d = f_H[Ca + f_H^{-1}(\theta_A, \theta_E, \theta_R)], \tag{5-17}$$

where, f_H is the Hoffman's function and is defined as,

$$f_H = \cos^{-1}\left\{1 - 2\tanh\left[5.16\left[\frac{x}{1 + 1.31x^{0.99}}\right]^{0.706}\right]\right\}. \tag{5-18}$$

in the above equation the equilibrium contact angle θ_E is replaced by either the advancing contact angle, θ_A, or the receding contact angle, θ_R, depending on the direction of the velocity vector at the contact line or the static contact angle, θ_E, if the contact line velocity is zero. It is worth mentioning that the no-slip models such as Kistler's correlation [102] have been extensively used to investigate droplet dynamics [103], [104]. In addition, it was shown that this model is capable to capture the relevant physics of droplet-substrate interaction and provides good agreement with experiment [144].

5.2.4 Geometrical Configuration and Meshing

The computational domain size of 100 μm × 100 μm × 400 μm is used for the 3D simulation of the impinging droplet onto a cold substrate with a given thickness. The mesh dependency test is performed based on the jumping velocity of a droplet on a superhydrophobic surface. The fluid domain is discretized by about 5 million, 8 million, and 12 million Hexahedral mesh with adaptive refinement at the interfacial cells. As the change of droplet jumping velocity in 8 million and 12 million mesh was minimal, the domain composed of 8 million fluid region mesh is applied for this study. According to Attarzadeh and Dolatabadi [144], for droplets smaller than 70 μm, direct modelling of surface roughness is crucial to simulate the dynamic of micro-droplet on a superhydrophobic surface. Superhydrophobicity is modeled as a series of micro-structured pillars with a square cross-section and squared patterns. The static, advancing and receding contact angles of 111°, 120°, and 86°, respectively are imposed over the surface of the pillars.

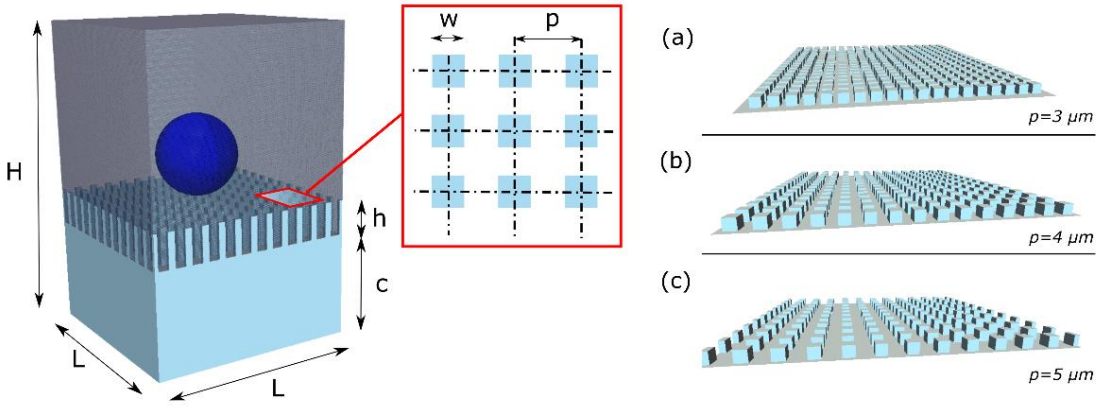

Figure 5-2: 3D computational domain with surface configurations (left), three coating morphologies used in this study (right), a) 2w3p, b) 2w4p, c) 2w5p

The substrate thickness of 30 μm is extracted from the domain. Series of hydrophobic pillars are implanted on top of the solid surface with 2 μm height, 2 μm width, and variying spacing between the pillars (1 μm, 2 μm, and 3 μm). The material properties of the substrate are given in Table 5-1.

5.3 Fluid-Solid Coupling

In this study, the partition method has been used to couple the temperature gradient between solid and fluid regions. Unlike the monolithic approach which uses a single matrix to solve the governing equation for both regions simultaneously, partitioned approach seeks to utilize existing fluid and solid solutions and couple these solvers at the interface of the two domains. The fluid solver uses a separate set of equations, variables, and mesh than the solid solver. The coupling happens at the boundary (λ_f, λ_s) where the temperature from the fluid updates the heat flux at the boundary of the solid which is then solved to determine gradient temperature at the interface

boundary (Neumann boundary condition). This updated boundary is then used as a Dirichlet boundary condition to solve the fluid domain. At the coupling interface λ the following condition must be satisfied,

$$\begin{cases} T_{\lambda \to f} = T_{\lambda \to s} = T_{\lambda} \\ k_f \left(\frac{\partial T_f}{\partial n_f} \right) = k_s \left(\frac{\partial T_s}{\partial n_s} \right) \end{cases} \quad (5\text{-}19)$$

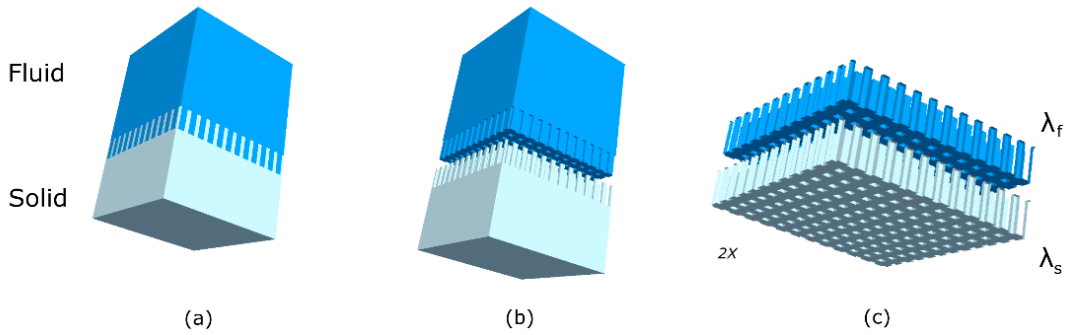

Figure 5-3: Geometrical configuration of the computational domain, a) fluid and solid b) fluid and solid separated, 3) fluid and solid coupling patches.

where the subscript *f* and *s* corresponds to the fluid and solid neighboring cells near the interface (λ).

Table 5-1: Material properties

	$\rho(\frac{kg}{m^3})$	$K(\frac{kg.m}{s^3.T})$	$C_p(\frac{m^2}{s^2.T})$	$\nu(\frac{m^2}{s})$
Air	1	0.02	1000	$1.78*10^{-5}$
Water	1000	0.6	4200	$1.0*10^{-6}$
TiO_2	4230	11	690	-
Al	2700	205	900	-

5.4 Results and Discussion

The effect of surface roughness on the dynamic and transient heat transfer of the micro-droplet with the solid surface has been examined. Figure 5-4 shows the impact of a room temperature micro-droplet on a textured (2w3p) superhydrophobic surface (TiO2, Al). The droplet and surface

are assumed to be in thermal equilibrium and above freezing temperature (T = 17°C). The droplet (D = 30 μm) was initialized close to the substrate at the instant of impact with 1.6 m.s −1 terminal velocity. The exposed area of the substrate is coated with a sub-micron thin layer of Stearic acid which has the intrinsic contact angles of θ_S = 110°, θ_A = 120°, θ_R = 86° which by nature is not water repellent. According to Cassie-Baxter model [17], physical roughness reduces energy barrier between the substrate and the droplet. Consequently, it was observed that the surface roughness increased the apparent contact angle to a value beyond 150°, and made the surface water repellent. Because of the substrate reduced surface energy, the droplet spread less compared to that on a smooth surface and was able to detach after 22 μs. Comparing the hydrodynamic of the droplet on textured substrates, it was revealed that the thermo-physical properties of the material had negligible impact on the maximum spreading length and penetration depth.

Figure 5-5 shows the impact of a room temperature micro-droplet on a −5 °C Aluminum, with the surface topography similar to that in Figure 5-4. Comparing two Figure 5-4 and Figure 5-5, it is evident that the dynamic of droplet changed after t = 13 μs. Because of the heat transfer between the droplet and the substrate, droplet showed no tendency to recoil and consequently remains on the surface. Figure 5-6 illustrates a similar impact scenario on Titanium dioxide (TiO2). Although the hydrodynamic of the droplet found to be same on Al and TiO2, a different outcome was observed. The difference arises when the droplet reaches its maximum spreading length, and due to an uneven exchange of heat between the surface and the droplet, it caused the droplet froze and stuck to the substrate.

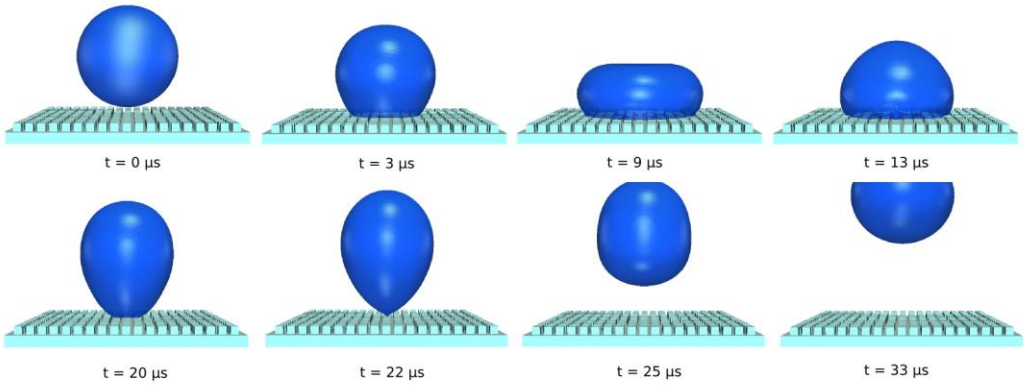

Figure 5-4: Time-lapse impact of a room temperature micro-droplet (V = 1.6 m/s) on textured (2wp3) superhydrophobic surface.

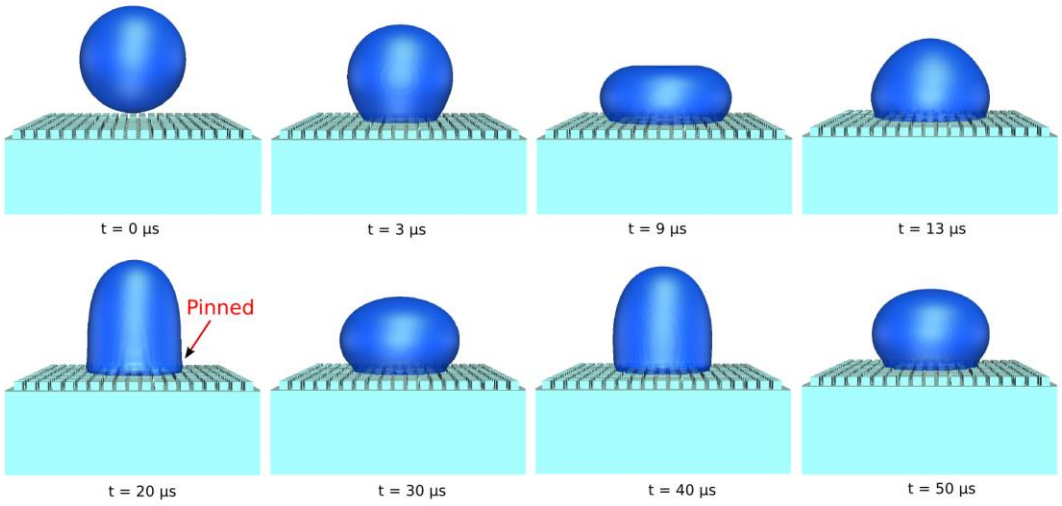

Figure 5-5: Time lapse impact of a micro-droplet impact (V = 1.6 m/s , T = 17 ˚C) onto a cold Al textured substrate (T = −5 ˚C).

Figure 5-7 illustrates the freezing mechanism inside the micro-droplet as it impinges on Al substrate. It has been demonstrated that there is an exchange of heat between the droplet and the substrate from the beginning of the impact (t = 2 µs). The figure illustrates temperature variation inside the solid substrate bulk and the droplet interface individually. At t = 5 µs the temperature of the peripheral edges of the liquid in contact with the substrate and the substrate are dropped to freezing, and the liquid latent heat starts to release. At this time, the temperature of the liquid

remains unchanged where the substrate heats up as the result of latent heat release until the phase change is completed. At t = 8 µs the entire latent energy of the liquid is released from the peripheral region of the liquid, and the formation of the ice nuclei becomes evident which are shown with white caps. For water, the ratio of latent heat to sensible heat is about an order of magnitude greater than other materials. This means that the discontinuity at the freezing front for water is much more severe when phase change starts. With the current methodology, the severity of the freezing front from water to ice has been well captured. At t = 20 µs the triple point is pinned on the surface and prevents droplet to complete its retraction stage. From this moment beyond, the droplet is stuck on the surface, and the ice layer keeps growing. The heat transfer rate on TiO2-2w3p was found to be less compared to that of Al which causes the droplet to bounce off before the entire energy of latent is released.

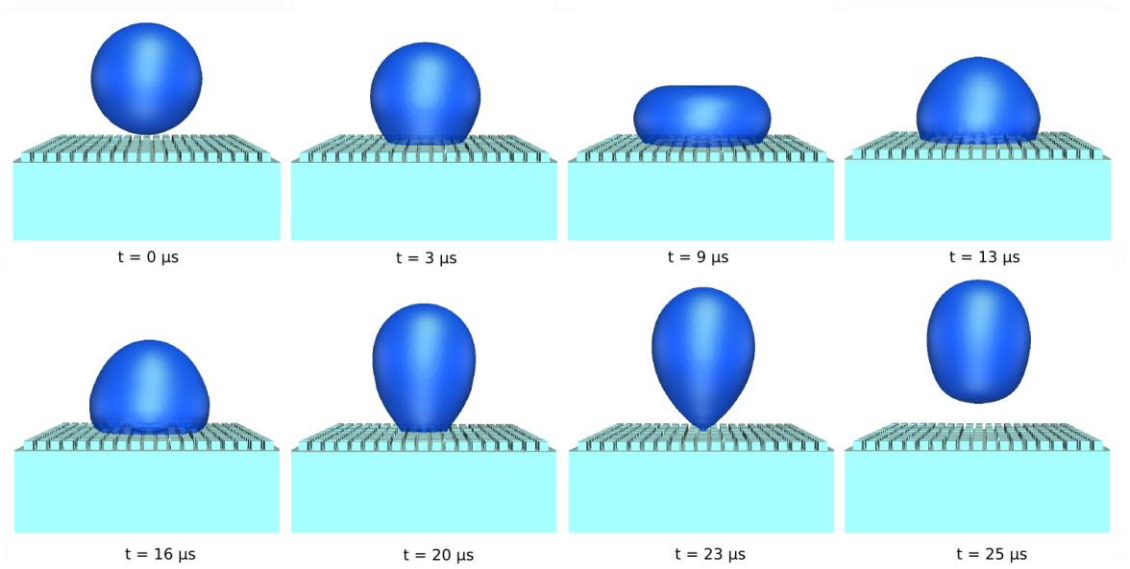

Figure 5-6: Time-lapse impact of a micro-droplet impact (V = 1.6 m/s, T = 17 ˚C) onto a cold TiO2 textured substrate (T = −5 ˚C).

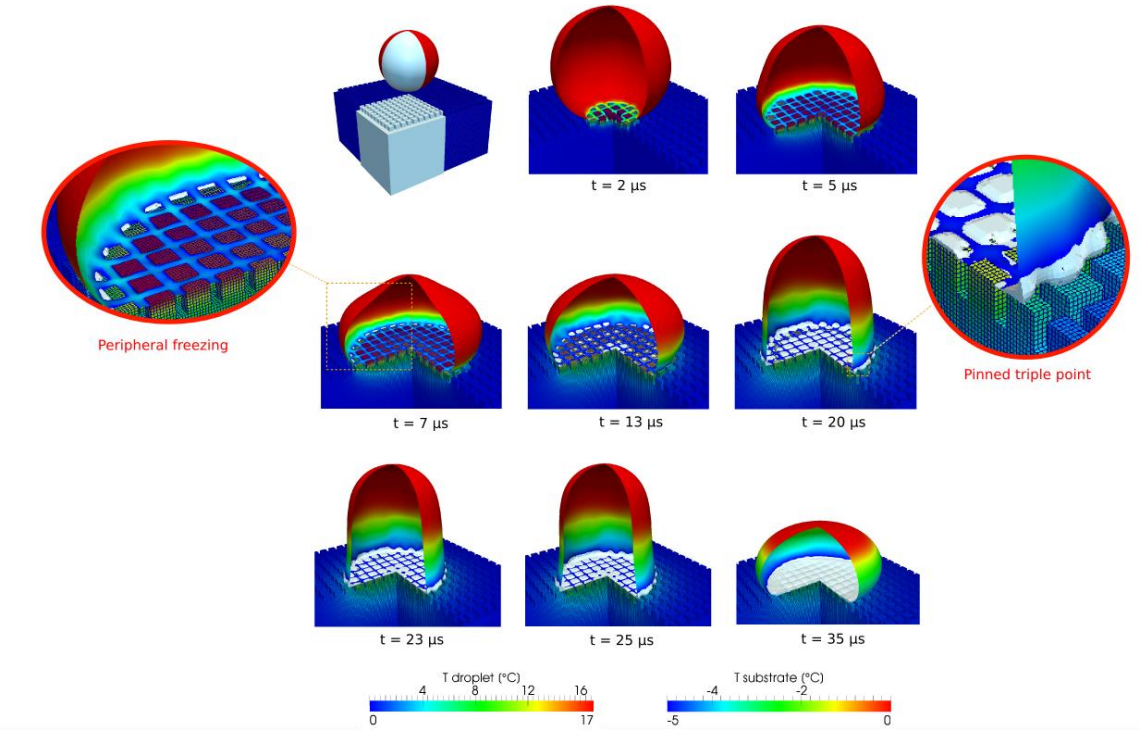

Figure 5-7: Time-lapse sequence of the freezing front dynamic inside the micro-droplet on a (V = 1.6 m/s, T = 17 ˚C) a cold Al substrate

The maximum wetted diameter becomes larger as the post spacing length is increased between adjacent pillars. Relative quantitative information is given in Figure 5-8. The maximum spreading diameter for droplets in a collision with Al and TiO2 on w2p3 is same. However, due to the freezing phenomena on Al surface, the triple point of the droplet where surface-droplet-gas meet gets pinned to the surface and resist against completion of the droplet recoiling phase.

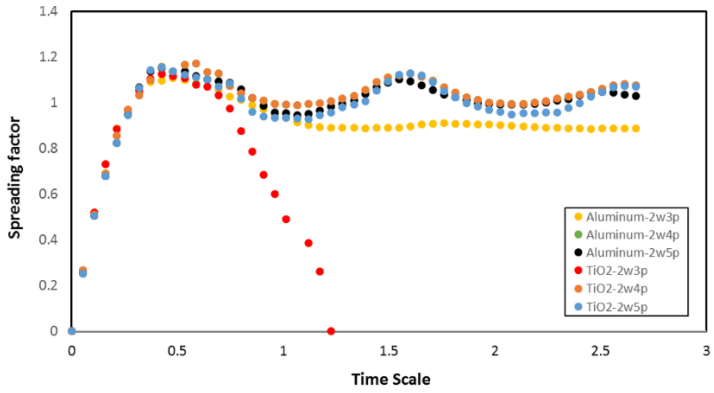

Figure 5-8: Temporal evolution ($T^* = tV_0/D_0$) of the spreading diameter ($\beta = D/D_0$) along the lattice axis direction after water droplet impact on different surfaces topologies.

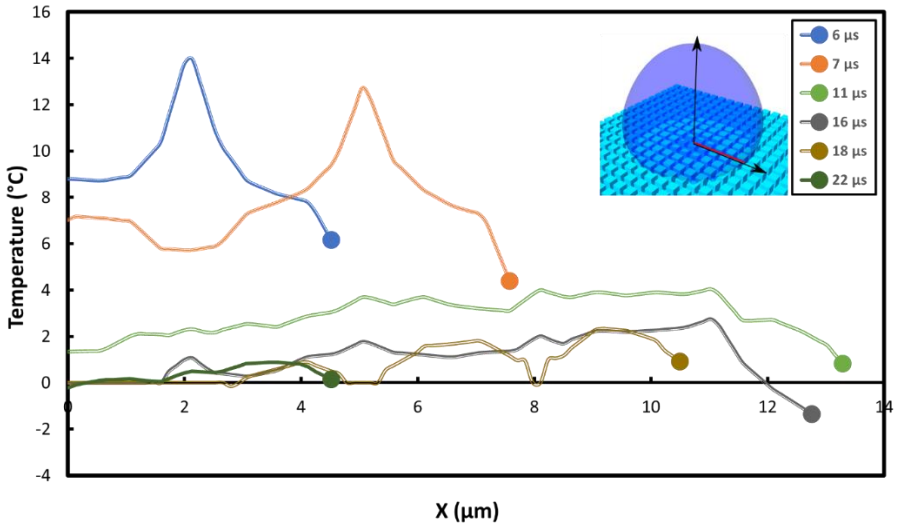

Figure 5-9: Temperature variation along the lattice axis at the surface of the TiO2

Figure 5-9 and Figure 5-11, show the time evolved temperature variation inside the droplet along the surface lattice (red line) for two substrates, TiO2 and Alumina, respectively. The axial length of each plot represents the maximum spreading length of the droplet at respected time. According to the Figure 5-9, the spreading length of the micro-droplet on TiO2 gradually increases to $X = 13.5\mu m$ with respect to the time at $t = 11\mu s$, and then it starts decaying to initiate recoiling phase and consequently bounce off the surface. It was observed that the temperature of the liquid in contact with the solid pillars does not fall below 0 °C except for a fraction of microseconds in the maximum spreading length ($t = 16\mu s$), when droplet is in sessile state. For $t = 11\ \mu s$ to $t = 16\ \mu s$, there is the maximum heat transfer between the two mediums, which results in appearance of the ice nuclei around peripheral edges of the micro-droplet as shown in Figure 5-10. However, because of the effect of surface tension during this stage (recoiling) and the convection of the heat inside the micro-droplet, the temperature of this region rises just enough to reverse phase transition, and facilitates the recoiling of the micro-droplet. In addition, at $t = 18\ \mu s$ and $t = 5\ \mu m$, there is a graph plateau indicating the liquid volume undergoing phase transition by

releasing the latent heat of fusion. Nevertheless, droplet rebounds before the entire latent heat releases and solidifies on the surface.

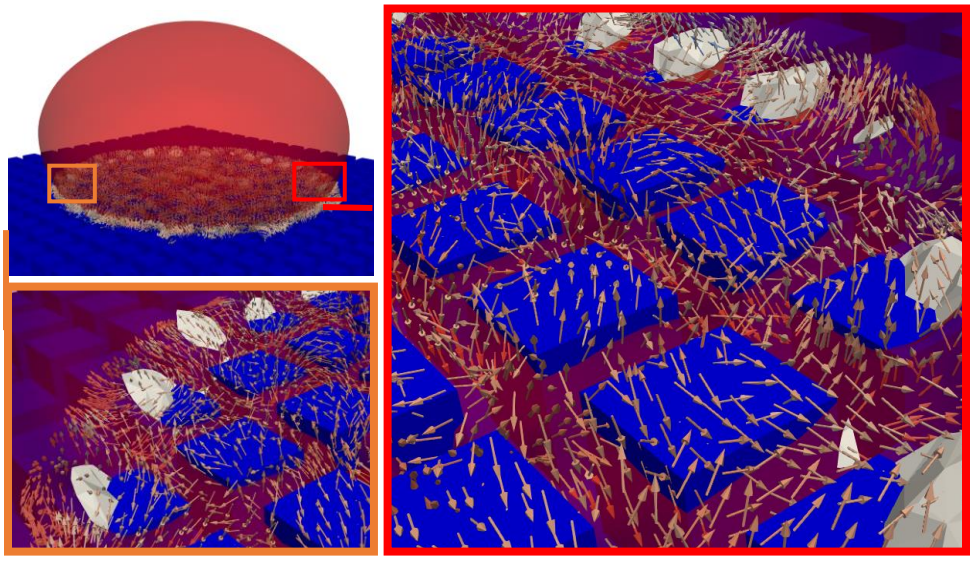

Figure 5-10: Interaction of the liquid flow with ice nuclei near the substrate at t=16 µs.

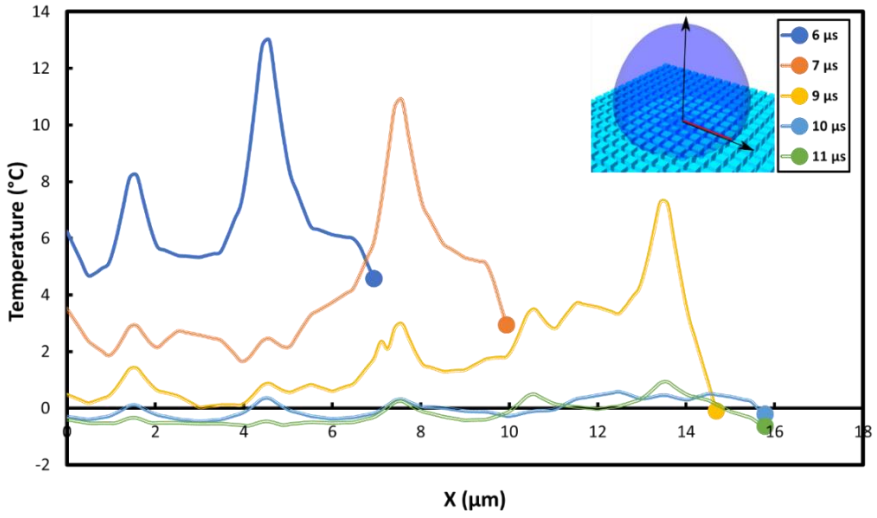

Figure 5-11: Temperature variation along the lattice axis at the surface of the Aluminum

According to Figure 5-11, the spreading length of the droplet on Alumina increases with time to 13.5 μm. Temperature of the peripheral edge falls dramatically below 0°C at $t = 9\ \mu s$ despite $t = 16\ \mu s$, on TiO2. At the maximum spreading phase, not only the edges, also some middle portion of the liquid has turned to ice. It was observed the droplet internal convection is not sufficient to

overcome the rate of heat transfer between the liquid and substrate, consequently it pins to surface. It has been shown that the higher thermal lower thermal diffusivity of Alumina acted as a barrier to diffuse the heat, and results in higher heat transfer rate.

5.5 Conclusions

In this paper, a volume of fluid (VOF) based multi-region conjugate heat transfer model is developed to undertake micro-droplet impact on textured surfaces accompanied by continues the exchange of heat between solid and fluid including phase change phenomena. The model is based on the enthalpy formulation of the energy equation. Coupling the momentum equation and contact angle model enabled us to directly model the effect of wall contact resistance through the inclusion of surface asperities into the model. Further conclusions are drawn as follow,

1. The method used in this paper could simulate the impact of cloud-sized droplet on superhydrophobic surfaces.
2. The textured patterns have a considerable influence on the hydrodynamics of the micro-droplet impact. Meanwhile, these patterns (roughness) can also change the contact resistance of the surface.
3. For substrates with high thermal diffusivity, ice growth initiates from the periphery of the droplet in the maximum spreading stage, while for low thermal diffusivity, ice growth initiates from the center point of the impact.
4. Combine effect of convective heat transfer inside the droplet, surface energy of the liquid droplet, and low diffusion of the heat inside solid bulk results in melting the ice nuclei from the peripheral edge of the micro-droplet.

Chapter 6

On the Numerical Modelling of Supercooled Micro-Droplet Impact and Freezing on Hydrophilic and Superhydrophobic Surfaces

6.1 Abstract

Most of the ice accretion on airframe is due to supercooled droplets in clouds which are located at altitudes below 2400m which aircrafts frequently have to pass during takeoff and landing. In the present work, the impact and freezing of a supercooled droplet is modeled based on (*i*) the volume of fluid (VOF) method coupled with a dynamics contact angle model to track the interface upon impacting, (ii) the modified momentum and the enthalpy formulation of the energy equations for the phase change during freezing, (iii) the nucleation theory, making use of Gibbs free energy as a barrier to be overcome before the supercooled liquid instantly freezes upon contact with the substrate. This analysis also avoids the use of any adjusting parameter regarding the supercooled liquid water (SLW) freezing. The simulation retrieves the characteristic concave ice-shape during droplet freezing, which is also found to promote the contact angle pinning. The solidification time which controls the type of ice is found to evolve exponentially with both the droplet maximum spreading diameter and the impact velocity. The model developed which accounts for the relevant proprieties for droplet freezing, can be used to better understand supercooled droplet freezing involved in ice accretion.

6.2 Introduction

Only in the US, airframe icing is responsible for more than 50 incidents and the loss of more than 800 lives between 1982 and 2000 [162]. Ice on aircrafts, roadways, and wind turbines are probably the most serious meteorological hazard facing the associated industries. Most of the ice accretion on airframe is due to supercooled droplets in clouds which are located at altitudes below 2400m which aircrafts frequently have to pass during takeoff and landing. The resulting in-flight icing of supercooled liquid water (SLW) droplet can take place on aircraft wing, tail, engine or instrument and lead to decrease the aerodynamic performance which could result in a lack of control or loss of thrust and constitute a major safety and security issue. In addition to the small SLW droplets (smaller than 50 μm), the supercooled large droplets (SLD) with sizes larger than 50 μm have been the focus of many researches. Better understanding of droplet impact dynamics including spreading, splashing, and recoiling on surfaces with various wettability from hydrophilic to superhydrophobic is necessary to predict the ice accretion on aircraft components.

The pioneering work on droplet spreading and solidification has been carried out by Madejski in 1976 [163], his analytical approach provides an estimation of the spreading diameter (or the degree of flattening) during solidification by combining the Stefan problem and a simple radial flow assumption. His model based on a 2D axisymmetric flow of the velocity field has been improved in [164] using a more suitable approximation for both the velocity field and the dissipation. Those works were only concerned with metal droplet solidification and do not address the water freezing. There are very few publications addressing water droplet solidification apart from the early work by Anderson et al. [165]–[167] based on geometrical analysis. More recently a geometrical model has been developed to analyze the singularity at the tip of a frozen water droplet [168], [169].

These models neglect the impact as well as the spreading; in addition, they fail to predict the concave ice-front.

It is worth noting that recent experimental, theoretical, and numerical works on supercooled droplet freezing are focused on the micro-physical processes involved such as the pattern and growth of dendrite following droplet impact. A very good agreement has been found on dendrite tip velocity between the numerical simulations based on both volume of fluid and level set methods, the experiments and the marginal stability theory of Langer and Muller-Krumbhaar in [170]. In addition, by repeating numerous supercooled droplets impact, a statistical model has been derived in [88] to estimate the rate of heterogeneous nucleation. A nice review in the physics, hydrodynamics and thermodynamics involved in the supercooled water droplet freezing can been found in [159]. Although the local micro-physical processes involved in the supercooled droplet freezing is important, there is still a challenge to derive a numerical model, retaining the relevant physics, capable of modelling supercooled water droplet freezing upon impact. The present work, at an intermediate scale between a micro-physical approach [171], [172] and the classical thin film or panel method used in icing code, aims to provide an approach to simulate droplet impact and freezing.

From a numerical point of view, for instance, the work by Pasandideh-Fard *et al.* [63] which rely on the enthalpy formulation in [70], [173] is the one reported treating the droplet impact and solidification, though their approach is based on the weak formulation solution method and is more suited for metal droplet as pointed out by these authors. Although their approach dealt with numerical modelling of droplet impact, their model still makes use of experimental data to describe the complex dynamics contact angle for the spreading and neglect the air presence considered as

void. It is important to emphasize that air may be entrapped at droplet impact and modify the heat transfer inside the droplet [174], [175].

We recently showed [85] both theoretically and experimentally the critical role played by the surrounding air on supercooled water droplet dynamics impacting on superhydrophobic surfaces. Although the Volume of Fluid (VOF) model can capture the physics governing metal solidification phenomenon relatively well (albeit neglecting the air phase), the water freezing problem which presents much more severe discontinuity at the phase front, seems out of reach by the conventional technique based on the enthalpy formulation as pointed out in [63]. Finding a formulation for water droplet capable of addressing these limitations of the enthalpy method will be one of the aims of the present paper.

Since all the icing certification conditions are tested in flight condition and/or tunnel experiments mostly due to the cost, development of reliable numerical tools is necessary. Most of the codes for aircraft icing are based either on thin film approach, panel method, or over-simplified scenarios for droplet impact and solidification using the average mass and heat transfer balance at the surface to predict ice accretion and neglect the dynamics of droplet impact and freezing. In this study a model of the impact and freezing of a supercooled droplet is developed by coupling the volume of fluid (VOF) method and a dynamics adaptive mesh refinement technique to track water interfaces with air and ice. The phase change is handled through both the modified momentum and the enthalpy formulation of the energy equations. Finally, the nucleation theory via Gibbs free energy is used to control the SLW upon impacting on the substrate.

The paper is organized as follows: in Section 2, the governing equations to handle supercooled water droplet impact and freezing are presented and in Section 3 the numerical schemes and the

model validation are provided. Numerical results and discussion are detailed in Section 4. Finally, conclusions are drawn in Section 5.

6.3 Methodology

Supercooled droplet modelling is challenging due to the combining effect of a moving contact line, simultaneous heat transfer and phase change. We assume a stable freezing of the supercooled droplet and neglect the anisotropic effects. An isotropic surface tension seems sufficient to describe the mechanism of supercooled droplet freezing [78]. While the models focused on the dendritic growth [176] are local, the present paper provides a global framework where both the interaction with the substrate through the contact angle and ice-liquid-gas is taken into consideration.

6.3.1 Governing equations

Supercooled droplet modeling is challenging due to the combining effect of a moving contact line, simultaneous heat transfer and phase change. We assume a stable freezing of the supercooled droplet and neglect the anisotropic effects. An isotropic surface tension seems sufficient to describe the mechanism of supercooled droplet freezing [78]. While the models focused on the dendritic growth [176] are local, the present paper provides a global framework where both the interaction with the substrate through the contact angle and ice-liquid-gas is taken into consideration.

The numerical simulation concerns with the modeling of the evolving 3-phases in presence, namely liquid, solid (ice), and air during a droplet impact on a superhydrophobic substrate exhibiting a hysteric effect. The 3-phase problem is addressed under the volume of fluid (VOF) framework, in which the liquid fraction is captured through the phase fraction parameter, α along,

with the liquid/solid(ice) fraction, f_{ls} . As a first attempt in modeling the critical recalescence phase in supercooled droplet freezing, the density variation effect is neglected as well as the thermal contact resistance at the droplet/substrate interface. The substrate is assumed to be at a constant temperature. The governing equations are based on the coupling between the liquid phase fraction equations, modified momentum and enthalpy conservation equations, and the classical nucleation theory to describe and derive in a physically-based manner the solid(ice) phase fraction.

2.3 The Liquid Fraction Equation

The two phases liquid (either in liquid and solid form) and the gas are defined by the volume phase fraction (α) which is advected by the flow, and the transport equation accounting for the interface compression method proposed in [85].

$$\frac{\partial \alpha}{\partial t} + \mathbf{U}\nabla\alpha + \nabla.\left[\mathbf{U}_c\alpha(1-\alpha)\right] = 0 \tag{6-1}$$

Where $\mathbf{U}_c$ represents the relative velocity at the free surface. The artificial compression technique in [101] results in adding an interface compression term on volume fraction transport equation.

The phase fraction or indicator function α is defined as follow,

$$\alpha = \begin{cases} 0, & gas\ phase \\ 0 < \alpha < 1, & phase\ interface \\ 1, & liquid\ phase \end{cases} \tag{6-2}$$

The phase fraction (α) enables to discriminate between the liquid/ice ($\alpha = 1$) phase from the gas phase ($\alpha = 0$). Similar to α, in order to distinguish ice from liquid, the solid-liquid fraction (f_{ls}) must satisfy the following conditions,

$$f_{ls} = \begin{cases} 0, & solid(ice)\ phase \\ 0 < f_{ls} < 1, & phase\ interface \\ 1, & liquid\ phase \end{cases} \tag{6-3}$$

The interaction with the substrate is handled through the dynamic contact angle. The accuracy in droplet dynamics is highly related to the way the dynamic contact angle is modeled. Here the contact angle is implemented using the correlation by Kistler [102], an extension of Tanner's law based on the capillary number $Ca = \mu U_{cl} / \gamma$ and the equilibrium contact angle θ_E ,

$$\theta_d = f_H(Ca + f_H^{-1}(\tilde{\theta}_E)) \tag{6-4}$$

where the Hoffman function allowing to calculate the inverse Hoffmann function is given by,

$$f_H(\tilde{\theta}_E) = \arccos\left\{1-2\tanh\left[5.16\left[\frac{\tilde{\theta}_E}{1+1.31\tilde{\theta}_E^{\,0.99}}\right]^{0.706}\right]\right\} \tag{6-5}$$

where, U_{cl} is the contact line velocity which is approximated by using the velocity at the interface in the first computational cell above the wall. In order to account for the hysteresis effect in the numerical model, the equilibrium contact angle θ_E in (6-13) is replaced by either the advancing contact angle, θ_A, or the receding contact angle θ_R depending on the direction of the velocity at the contact line (Fig. 2). This implementation makes our model unlike the one reported in the literature to not rely systematically on experiments for imposing the contact angle. The modified contact angle $\tilde{\theta}_E$ in (13) is given by,

$$\tilde{\theta}_E = \begin{cases} \theta_A & U_{cl} > 0 \\ \theta_E & U_{cl} = 0 \\ \theta_R & U_{cl} < 0 \end{cases}$$

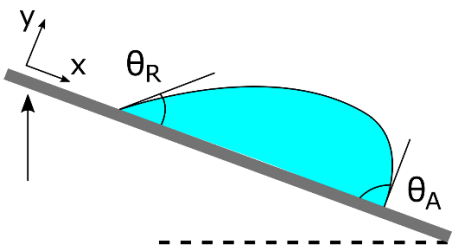

Figure 6-1: Advancing and receding contact angle captured by titling base method.

The schematic in Figure 6-2 shows the numerical cells assignment, based on α and f_{ls}, for a freezing droplet. This function combining with α is essential in the development of the freezing model which will be detailed below.

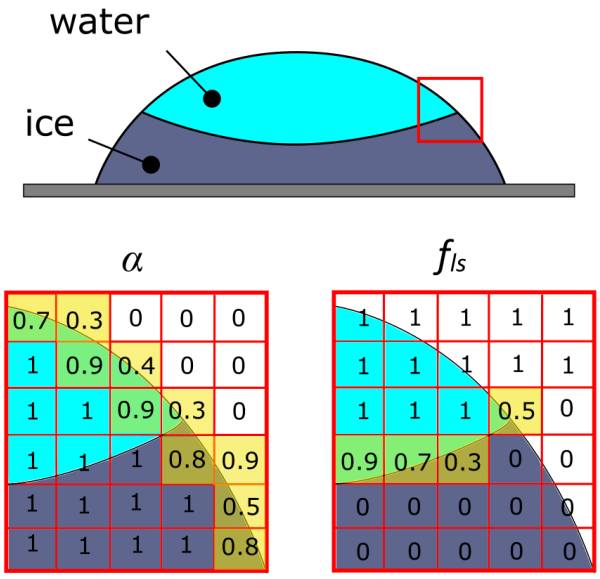

Figure 6-2: Schematic of the numerical cells (values of α and f_{ls}) in the freezing droplet.

6.3.2 Modified Momentum Equation

In addition to the energy equation, the fluid motion and droplet impact are modeled using Navier-Stokes equations, assuming the liquid of density (ρ), viscosity (μ) and surface tension (σ) to be incompressible and Newtonian, and the flow to be laminar. The momentum equations to be numerically solved in the VOF formulation are:

$$\frac{\partial(\rho \mathbf{U})}{\partial t} + \nabla.(\rho \mathbf{U}\mathbf{U}) = -\nabla p + \rho g + \nabla.\mathbf{T} + \gamma\kappa\nabla\alpha + \alpha B\mathbf{U} \tag{6-6}$$

In equation (6-15), the continuum surface force (CSF) method of Brackbill *et al*. [177] is used to model the surface tension as a body force acting only on interfacial cells; and the mean curvature at the interface is given by,

$$\kappa = -\nabla.\left(\frac{\nabla\alpha}{|\nabla\alpha|}\right) \tag{6-7}$$

where the viscous tensor expresses as $\mathbf{T} = \mu\left(\nabla\mathbf{U} + \nabla\mathbf{U}^T\right)/2$.

The fifth right-hand source term originates from porous media analysis, this contribution enables to discriminate the solid (ice) from the liquid phase by ensuring a zero velocity for the solid phase while ensuring the momentum equation for the gas phase is unaffected owing to the introduction of the phase fraction (α). The coefficient, *B,* should increase from zero for liquid to a large value as the liquid is solidified.

$$B = \frac{b(1-f_{ls})^2}{f_{ls}^{\,3} + \varepsilon} \tag{6-8}$$

6.3.3 Energy Conservation Equation

The heat transfer modelling involved between the liquid, solid and air is addressed using an energy conservation equation based on the enthalpy, *H*. However, as a simplification, the thermal contact resistance at the droplet/substrate interface will be neglected thus the substrate will not be explicitly modeled. The energy equation based on the enthalpy formulation can be expressed as follows,

$$\frac{\partial(\rho H)}{\partial t} + \nabla.(\rho \mathbf{U} H) = \nabla.[\nabla(KT)] \tag{6-9}$$

where ρ is the density, C_p, the heat capacity, K the thermal conductivity. V_0 and ΔT are characteristic velocity and temperature, respectively. Since the Eckert number, representing the ratio between the kinetic energy to the enthalpy, $Ec = V_0^2 / C_p \Delta T \approx 10^{-4} << 1$, the viscous dissipation is neglected. In order to account for phase change due to the solidification, the specific sensible enthalpy is extended by the latent heat of fusion *L*.

$$H = C_p T + \alpha f_{ls} L \tag{6-10}$$

This latent heat should be multiplied by the liquid/solid fraction f_{ls} within the numerical cell.

The energy equation in the framework of the VOF method can be formulated in terms of temperature. by inserting Eq. (6-2) in Eq. (6-1)**,**

$$\frac{\partial(\rho c_p T)}{\partial t} + \nabla.(\rho C_p \mathbf{U} T) = \nabla.[\nabla(KT)] + S_H \tag{6-11}$$

where a source term, $S_{\mathrm{H,}}$ accounting for the phase change appears as expressed in Eq. (5).

$$S_H = -L\left[\frac{\partial}{\partial t}(\rho f_{ls}) + \nabla.(\rho \mathbf{U} f_{ls})\right] \tag{6-12}$$

There is a special treatment to be performed when solving the enthalpy formation Eqn.(6-101) which requires a scheme for the enthalpy to be carried out at each outer iteration of the energy equation [10]. This scheme is used to ensure boundness and convergence. In the present study, to avoid the classical numerical ad hoc treatment for solving the energy enthalpy-based equation and due the severe transition for water freezing, an approximate analytical function of the liquid/solid (ice) fraction is proposed and expressed as follows.

$$f_{ls} = \frac{1}{2}\left[1 + \tanh(k_l(T - T_{ms})\right] \tag{6-13}$$

The liquid fraction in the freezing liquid, fully dependent of the temperature, indicates that phase change can occur in a very narrow range of temperature as for water or pure substance. The parameters k_l and T_{ms} define respectively the width and center of the phase change transition. T_{ms} corresponds to the drop-substrate interface temperature, at which the unstable supercooled water droplet instantly starts to freeze upon impact. The parameter k_l adjusts the slope of the liquid/ice phase transition zone, it controls the temperature ranges at which phase change occurs; unlike metal alloy, for water the transition is very steep. Here under supercooled condition, we express the parameter k_l through the classical nucleation theory as detailed in the next sub-section. This expression avoids the use of an ad-hoc scheme and the steep nature of this function can enable the treatment of material like water which presents a much more severe discontinuity at the phase front, mainly due to the fact that the ratio of latent heat to sensible heat is about an order of magnitude greater than that for metals. This is one of the reasons that the water freezing treatment is not well addressed by the classical use of the weak solution of the enthalpy method [63], [173]. The introduction of this function then allows to derive the source term in the energy equation and to handle more accurately phase change involving water. The determination of the parameter k_l under supercooled conditions will be performed using the classical nucleation theory.

6.3.4 Classical Nucleation Theory

The heterogeneous nucleation at the solid-liquid interface is assumed to be the leading mechanism that initiates droplet freezing, which is the situation observed experimentally without any external gas flow [78], [85]. The nuclei formation is controlled by the energy barrier to be overcome for ice formation. Since the nucleation rate is related to the ratio of the population of frozen and unfrozen droplets. It is assumed that this mechanism is applied locally within the droplet. Therefore, the solidification can be viewed as the result of the formation of multiple critical nucleus (seeds) which induces the whole droplet freezing heterogeneously starting from different portion of the substrate. According to the classical nucleation theory, the rate of nucleation under supercooled condition can be expressed through the critical Gibbs free energy as follows,

$$J = N_c \exp\left[-\Delta G^* / k_B T\right] = \frac{dv_s}{dt} \tag{6-14}$$

where J is the nucleation rate and can be approximated by $J=dv_s/dt$, where the volume v_s corresponds to the volume of ice at a given time in the droplet. The prefactor N_c corresponds to kinetic coefficient for nucleation, k_B is the Boltzmann constant, and ΔG^* the critical Gibbs free energy under heterogenous supercooling freezing condition is given by,

$$\Delta G^* = \frac{16\pi \gamma_{SL}{}^3 T_m{}^2}{3L^2 \Delta T^2} S(\theta_E) \tag{6-15}$$

where $S(\theta_E) = \left(2 + \cos\theta_E\right)\left(1 - \cos\theta_E\right)^2 / 4$, T_m is the water melting temperature and γ_{LS} is the ice water interfacial energy. The greater the supercooling $\Delta T=T_m-T$, the smaller the critical radius and the energy required to initiate the nucleation.

From Eqn.(6-7) and using the derivative with respect to the temperature, one can write the followings.

$$\frac{dv_s}{dT} = v_s \frac{d}{dT}\left[-\Delta G^*/k_B T\right] \tag{6-16}$$

On the other hand, the nucleation rate can be derived from the liquid solid fraction Eqn.(6-6).

$$\frac{dv_s}{dT} = \frac{d\left[V_T(1-f_{ls})\right]}{dT} = -\frac{1}{2}k_l V_T\left[1-\tanh k_l(T-T_{ms})^2\right] \approx -2k_l v_s \tag{6-17}$$

Using the definition of ice volume fraction within a droplet of volume V_T that $1\text{-}f_{ls} = v_s/V_T$ and assuming $\tanh(x) \to 1 \quad x >> 1$ under supercooled conditions and after factoring $1-\tanh(x)^2$.

Finally, comparing eqn (6-9) and (6-10) we can deduce the equation for k_l as follows.

$$k_l = \frac{8\pi\gamma_{SL}{}^3 T_m{}^2}{3L^2 k_B \Delta T^5 T^2}\left(2T-\Delta T\right)S(\theta_E) \tag{6-18}$$

6.4 Numerical techniques and model validation

6.4.1 Numerical techniques

The governing equations eqn. (6-9)-(6-18) are implemented in OpenFOAM/C++ and discretized using a finite volume based volume of fluid method following the schemes detailed in Table 6-1.

Table 6-1: Discretization schemes

Term	Discretization scheme	Method
$\frac{\partial}{\partial t}(\rho U), \frac{\partial}{\partial t}(\rho C_p T),$	Euler	Bounded implicit scheme
$\nabla.(\rho C_p U T)$	van Leer	See [178]
$\nabla.(\rho U U), \nabla.(\rho C_p U T), \nabla.(U\alpha_l)$	van Leer	See [178]
$\nabla.U_c\alpha_l(1-\alpha_l)$	Interface compression	See [179]

$\nabla.(\rho UT)$	Gauss upwind	See [180]
$\nabla.(\nabla kT)$	Gauss harmonic corrected	See [181]

6.4.2 Adaptive time step control

Since the flow field is unknown at the beginning of the calculation, introducing a proper time step can be challenging. In addition, during the calculation if the values of the time step are not controlled, this may result in an unstable solution unless very small time steps are chosen. However, extremely small time steps consume much more computational efforts. Therefore, using adjustable or adaptive time step enables accurate calculations and reduce the computational effort. The time step is adjusted according to the prescribed maximum Courant number and maximum time step size. The new time step is initiated from the following form:

$$\Delta t = \min\left\{\min\left[\min\left(\frac{Co_{\max}}{Co_o}\,\Delta t_o, \left(1+\lambda_1\frac{Co_{\max}}{Co_o}\right)\Delta t_o\right), \lambda_2\Delta t_o\right], \Delta t_{\max}\right\} \tag{6-19}$$

Where the courant number is determined from the following equation,

$$Co = \frac{U_f.\mathrm{d}}{|\mathrm{d}|^2}\Delta t < 1 \tag{2}$$

The local courant number Co_o is calculated using valued from the previous (old) time step. In order to avoid time step oscillation, the increase of the time step is damped using the factors λ_1 and λ_2. At the beginning of the calculation the time step size is evaluated from,

$$\Delta t_o = \min\left(\frac{Co_{\max}\Delta t_{\text{init}}}{Co_o}, \Delta t_{\max}\right) \tag{3}$$

And this intermediate value is then used in eqn.(1) in order to ensure that the value of Co_o at the initial time step be close to the prescribed limit value $Co_{\max}$. In this study $Co_{\max} = 0.2$.

The simulations are performed on a 2D axisymmetric geometry and run in parallel using a domain decomposition method. The Pressure Implicit with Splitting of Operators (PISO) algorithm is used to calculate the pressure and velocity, while the energy equation is solved using a preconditioned bi-conjugate gradient technique.

6.4.3 Geometrical configuration and meshing

A 2D axisymmetric computational domain size of $4D_0 \times 8D_0$ was used to model the impact of the sub-millimeter droplet. As shown in Figure 6-3 the impact occurs in an open system. The top and side wall surfaces are subjected to the atmospheric pressure with no gradient effect of velocity. The bottom surface is a non-slip wall carrying zero gradient effect of pressure. The inner axis is the symmetry line which the domain revolves radially around this axis. The side walls are extended far enough from the location of impact to ensure that the imposed pressure boundary condition would have a minimal effect on the hydrodynamic of the droplet impact. From the mesh refinement study performed in an isothermal condition [121], the optimum mesh size was found to be 60 cells per droplet diameter. For non-isothermal condition, three computational mesh resulting to 60, 180 and 300 cells per diameter of the droplet was performed to compare the total freezing time of the micro-droplet. Since the change in freezing time of the droplet between 180/D and 300/D was minimal, the computational domain composed of coarser mesh with 180 cells per initial diameter of the droplet was selected in this study.

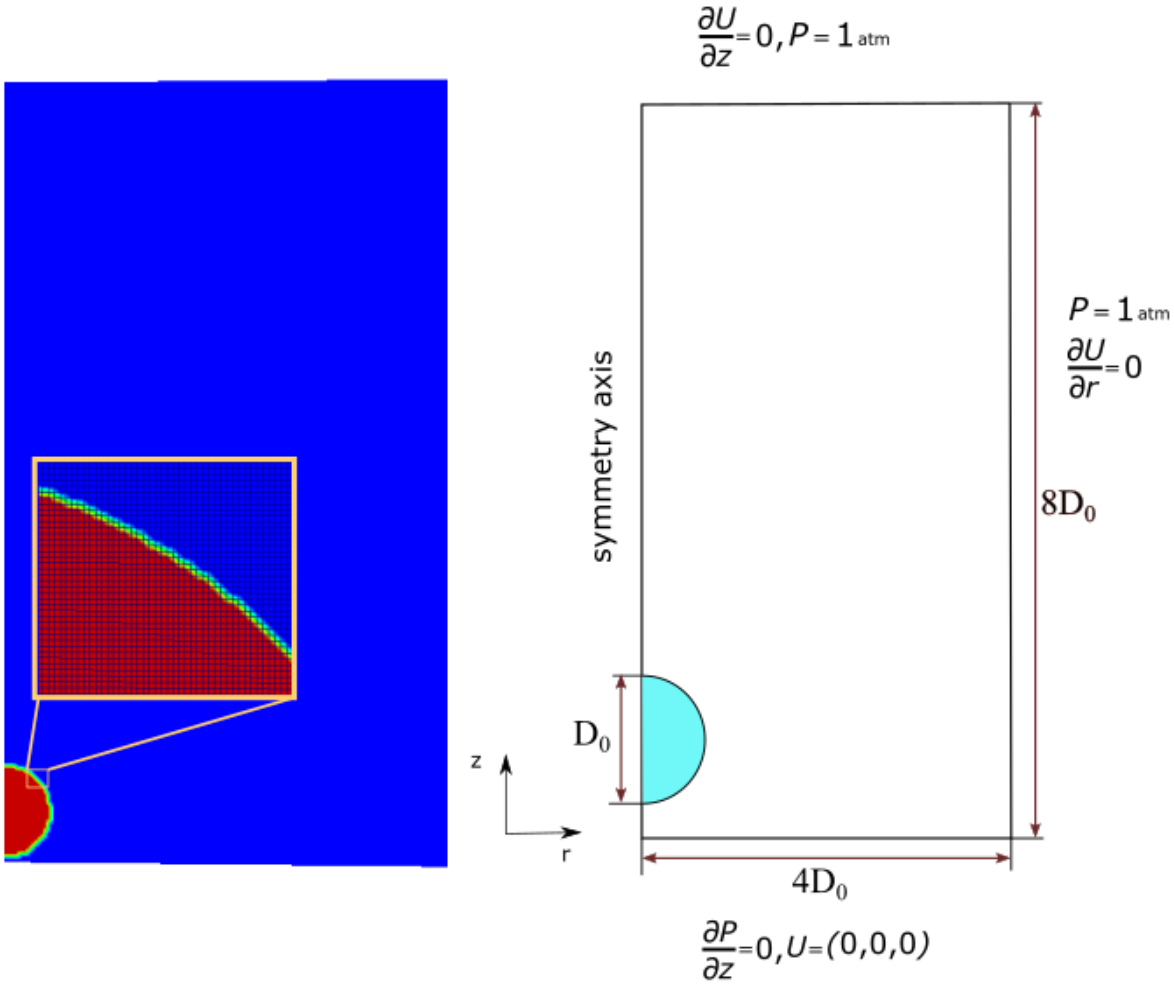

Figure 6-3:Computational domain of the numerical model.

6.4.4 Validation

Our numerical approach to handle droplet dynamics has been previously validated at isothermal conditions. In [121], a numerical validation against the experiment of droplet impact, coalescence and induced detachment on a solid surface is provided. A numerical modelling of two identical micro-droplet coalescence on superhydrophobic surfaces in [144] was validated with the experimental data reported in the literature [116]. While Droplets coalescence under the effect of shear flow is investigated both experimentally and numerically in [157]. These studies highlight the capability of the current interface tracking method (VOF) to capture the hydrodynamic of the

micro-droplet on superhydrophobic surfaces. In the present work, the previous model is extended to probe the impact of a supercooled droplet on a cold surface. In addition to the Stefan problem, the model will be compared with the experimental work reported by [182] which is one the most detailed study on the impact of supercooled droplet impact on a superhydrophobic surface.

In order to validate the approach a comparison is performed with the Stefan problem for which an exact analytical solution exist. The system consists of a semi-infinite domain in the liquid phase before freezing from the boundary. As time progresses the interface moves upwards. The analytical solution for the freezing front evolution, known as Neumann's solution is given by [183],

$$y(t) = 2\chi\sqrt{\alpha_T t} \tag{6-20}$$

where α_T is the thermal diffusivity and χ is dependent on the Stefan number [183].

Assuming that the thermal capacities as well as the densities of ice and liquid phases are equal, the evolution of freezing front is shown in Fig.3. The simulated freezing front growth is well predicted with the square root of the time evolution ($\sim t^{1/2}$) in accordance with the Stefan problem. The comparison with the 2D Stephan problem is promising, though the model is slightly faster in estimating the solidification time. This may be due to the fact that the density change effect is neglected.

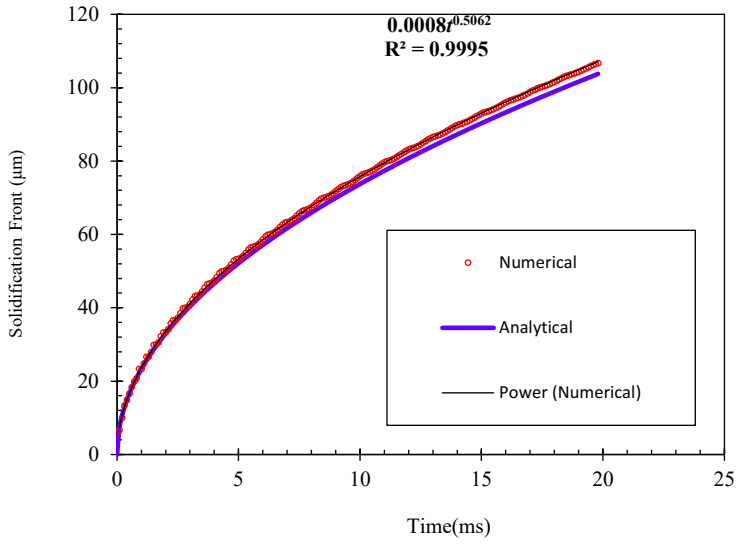

Figure 6-4: Simulated and analytical evolution of the freezing front.

6.5 Results and Discussion

In order to determine if the simulation agrees with physical reality, a comparative study was performed for a certain range of SLW droplet temperatures with various impact velocities as reported in the work of Maitra et al. [182]. The substrate is superhydrophobic with a static contact angle of 154° and an advancing and receding contact of 162°/148°, respectively. Figure 6-5 shows the time evolution of the impact of 2 mm supercooled water droplet at -5°C. It is noticeable that icing layer started appearing around 1.5 ms after the impact. The iced layer expands at t=3.5 ms and as a result, the droplet is pinned to the surface at t= 4.5 ms. This pinning is known as the main cause of superhydrophobic failure which resists water droplets to complete their retraction phase and detach from the surface.

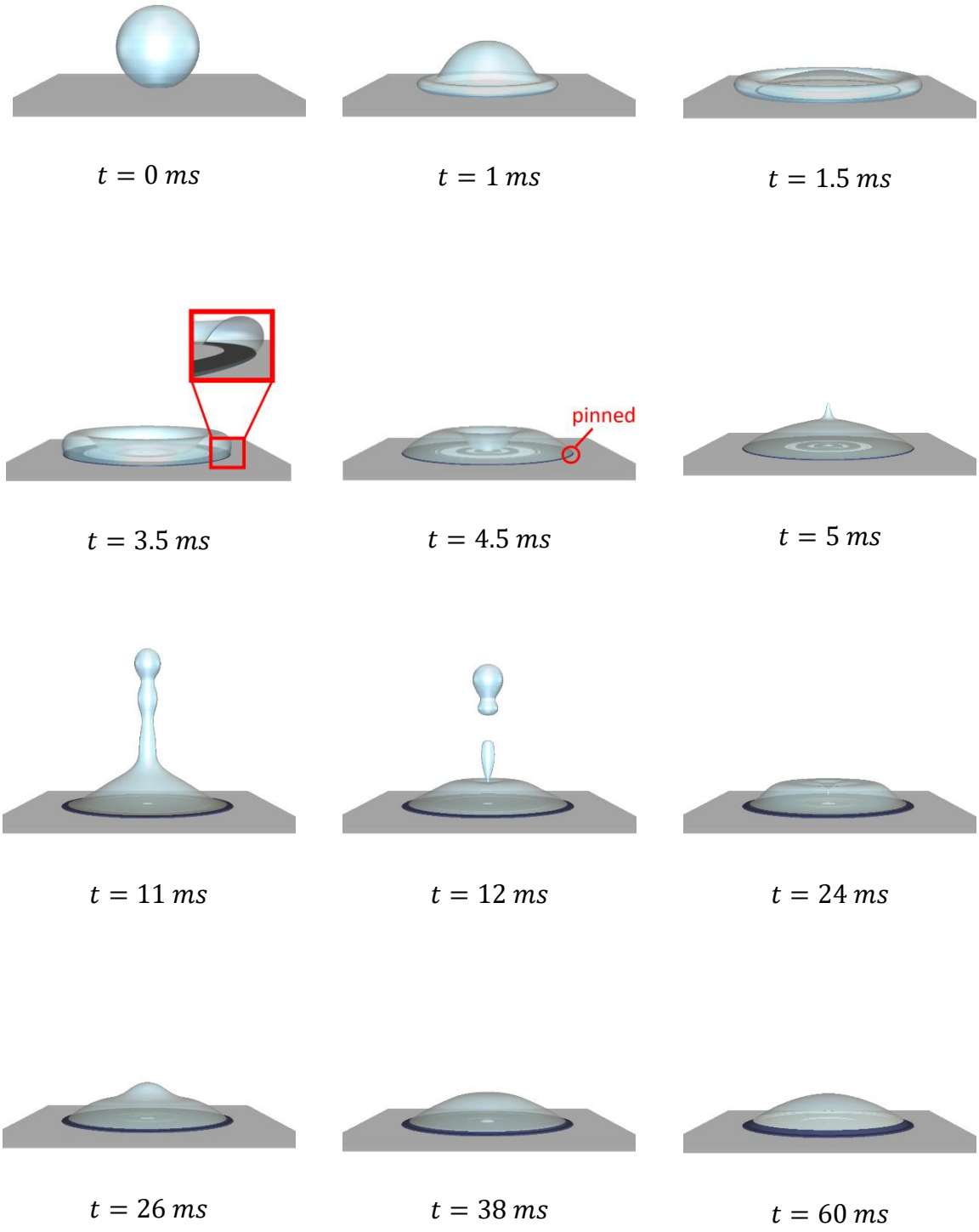

Figure 6-5: Freezing of a 2 mm droplet SLW with an impact velocity of 1.3m/s on a substrate at -10°C.

The maximum spreading length at different supercooled temperatures are shown in Fig. 6-6. The dash lines are approximations obtained from the experiment and the symbols are the results of the simulations. The results are in close agreement with the experimental data [182] although slightly smaller spreading length was captured in all simulated cases. This can be likely due to the change in density of the liquid and ice which has not been considered in the model.

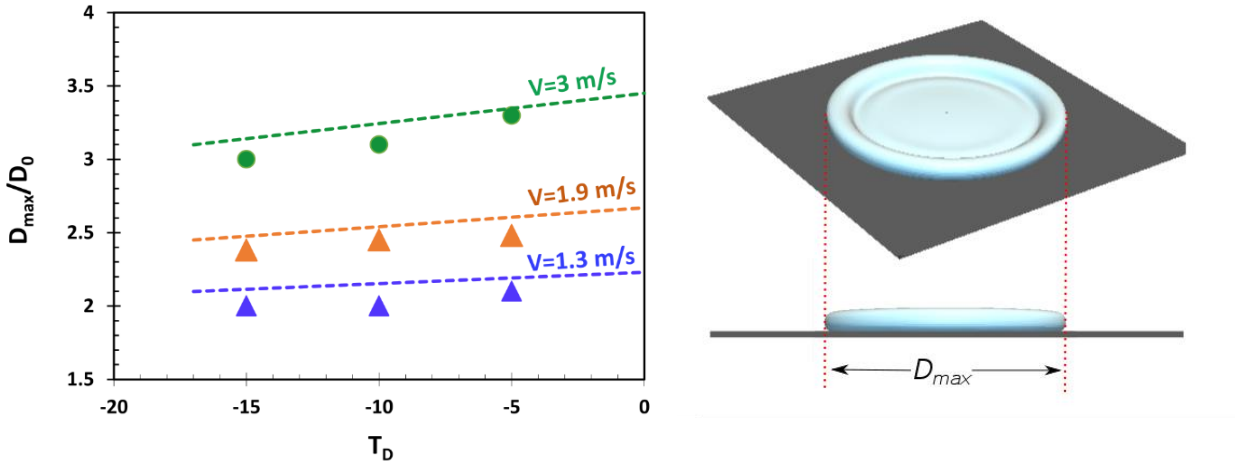

Figure 6-6: Simulated (symbols) and experimental [18] (lines) spreading length at different supercooled droplet temperatures and impact velocities.

One of the interesting features of the present model is the capability to simulate the droplet impact and freezing under a wide range of operating conditions. In Figure 6-7, the impact at 1 m/s of a supercooled droplet at -5°C on a substrate at -10°C is presented. The substrate is superhydrophobic with a astatic contact angle of 154°, as well as advancing and receding contact angles of 162° and 148°, respectively. In order to observe the whole process of freezing and the freezing line motion and shape during the phase change process, a rather small droplet (200 µm) has been opted in this simulation.

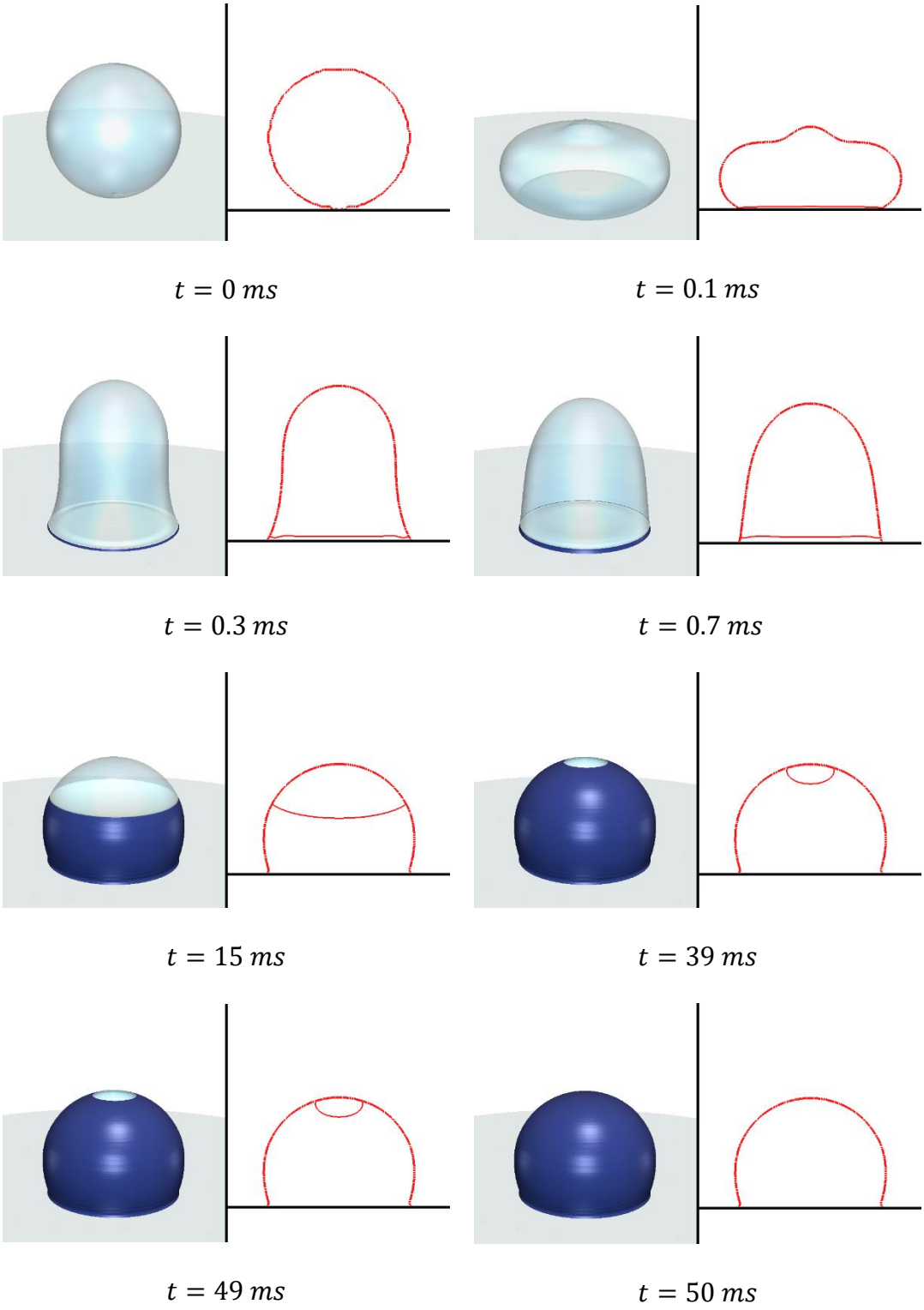

Figure 6-7: Simulated freezing of a 200µm SLW droplet with an impact speed of 1m/s on a superhydrophobic substrate at -10°C.

Because of the instantaneous freezing, the droplet oscillation is damped, and the droplet is pinned right after the impact on the substrate. The simulation clearly shows the concave ice-front of the freezing droplet. Evolution of the droplet freezing front is different from that of a semi-infinite freezing as in the Stefan problem. Indeed, in the case of supercooled droplet, even though the freezing front evolution is initially comparable to that of the Stefan profile, after a certain time, the freezing profile becomes concave ($t > 15\ ms$). This effect is associated with the finite size of the droplet as opposed to the freezing of a semi-infinite domain.

Finally, freezing of supercooled droplets at different velocities is investigated. A comparative transient evolution is shown in Fig. 7 for a supercooled droplet at a temperature of -5 C on a superhydrophobic surface at -10 C for two different velocities of 0.5 and 5 m/s. As expected, the higher velocity leads to a higher contact area before the freezing starts. Consequently, the freezing time is much smaller for the case with a larger impact velocity.

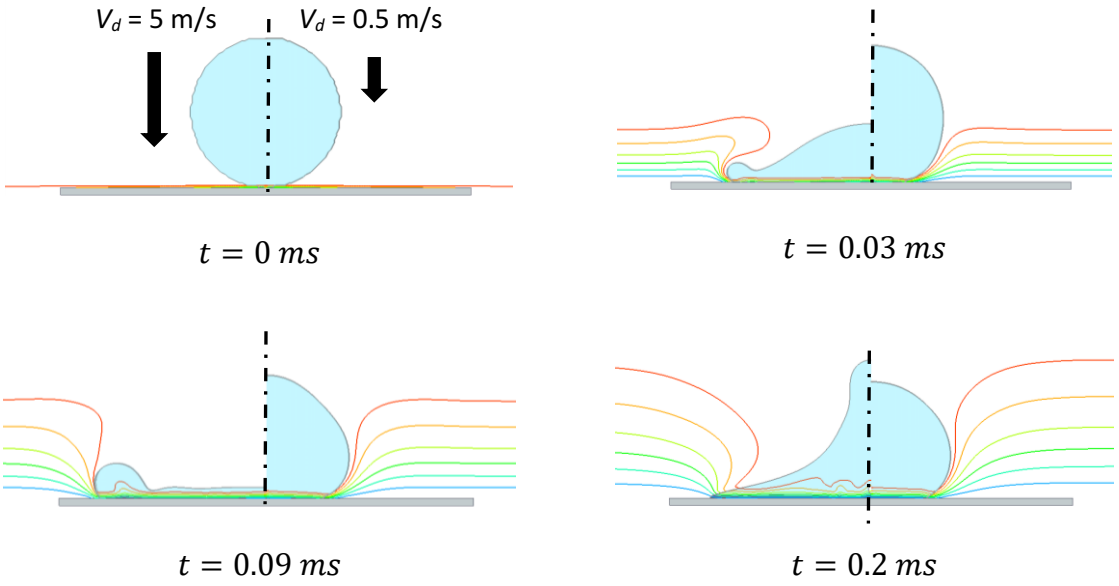

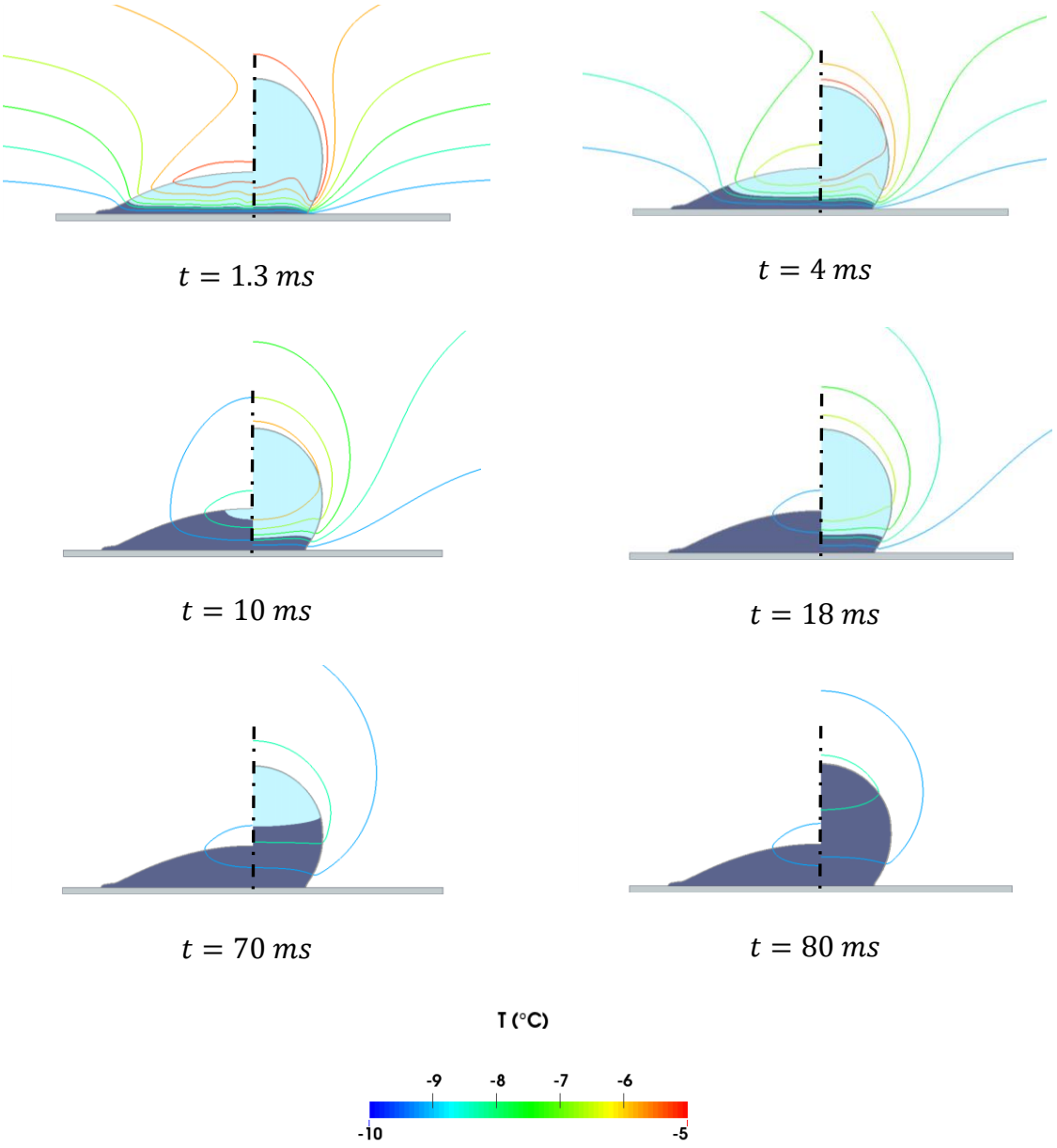

Figure 6-8: The effect of velocity on the freezing dynamics along with the temperature contour of a droplet of 200µm impacting at (right) 0.5 m/s and (left) 5m/s.

A detailed analysis indicates that the maximum spreading diameter is one of the main parameters which controls the droplet freezing time. A correlation shows that the evolution of the freezing time versus the maximum spreading diameter is exponential (Fig 8). For convenience, the freezing time (T_s) and the maximum spreading diameter or length (D_{max}) are made dimensionless through the thermal diffusivity ($\alpha_T=k/\rho Cp$) and the initial diameter (D_0).

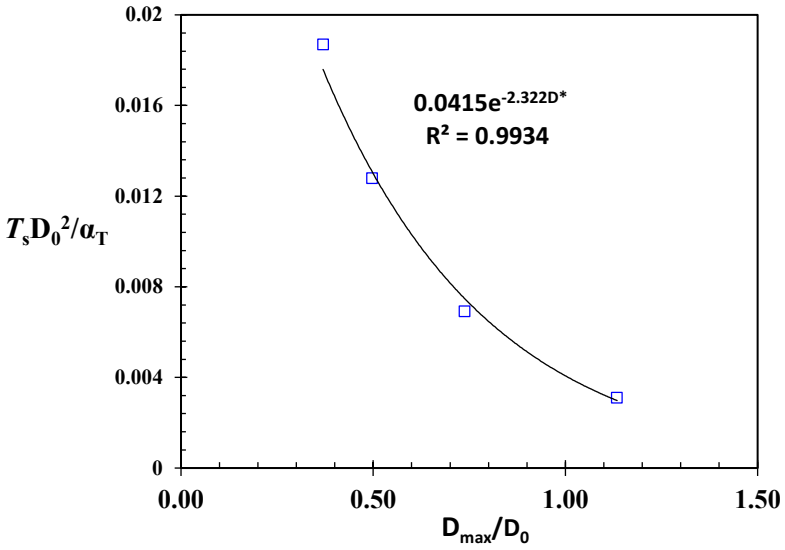

Figure 6-9: Dimensionless solidification time versus the dimensionless maximum spreading diameter.

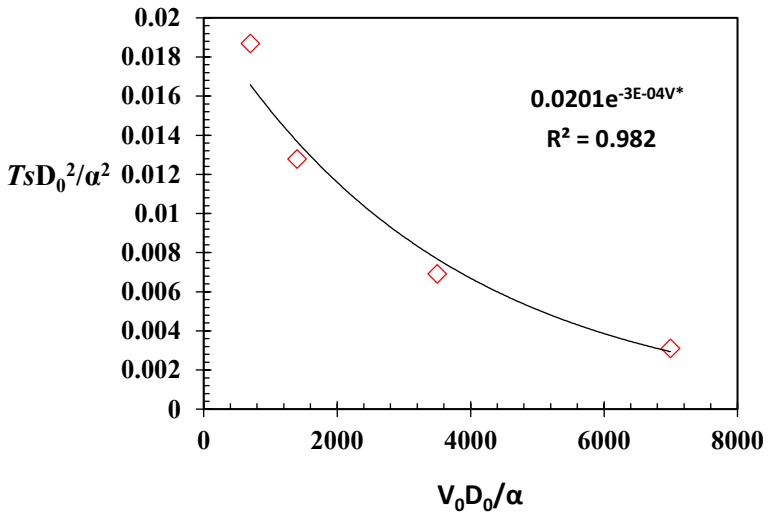

Figure 6-10: Dimensionless solidification time versus the dimensionless impact velocity.

6.6 Conclusions

In this paper, a volume of fluid (VOF) based model is developed to undertake water droplet impact, spreading and freezing under supercooled conditions. The model is based on the enthalpy formulation of the energy equation, and an approximation of the liquid/solid fraction, as well as

the nucleation theory. These equations by coupling the momentum and contact angle model enabled us to simulate the water freezing upon droplet impact. The freezing front evolution of an impacted freezing droplet is found to differ from that of the Stefan problem. The model also retrieves the well-known concave ice-front for a freezing water droplet. In addition, the solidification time which controls the type of ice is found to evolve exponentially with both maximum droplet spreading diameter and the impact velocity. The model developed can be used to better understand the dynamics of a freezing droplet for ice mitigation in the aerospace industry. Future work will address the extension of the model to account for the thermal contact resistance as well as the density variation along with a detailed transient comparison with the experiments tailored to more realistically track the freezing front.

Chapter 7

Conclusions and Suggestions for Future Work

7.1 Summary and conclusions

Despite a vast field of superhydrophobic applications, many parts of the physics associated with the impact of micro-droplets on superhydrophobic surfaces are not entirely understood. Because of this knowledge gap, understanding the interaction between micro-droplets and the roughness of superhydrophobic surfaces, as well as the role of the roughness in the functionality of ice-phobic surfaces was the main aim of this thesis. Although micro/nano-structured coatings created by thermal spray, laser patterning, chemical or physical vapor deposition technologies have unique properties (i.e., hydrophobic, thermal barrier, etc), controlling these properties are still challenging. For instance, superhydrophobic surfaces are well known for their excellent water repellent properties, but it is as yet unknown if they can be fabricated in such a way to mitigate ice in freezing conditions.

To this aim, a numerical model was developed based on a finite volume methodology to study the impact and freezing of liquid micro-droplet impingement on micro-structured superhydrophobic surfaces. The model is applicable to transient non-isothermal multiphase flow with a phase change (solidification) along with a conjugate heat transfer boundary condition between the fluid (composed of liquid and gas) and the solid domains through the solid-fluid and

fluid-solid interfaces. In this thesis, the model was used to analyze the hydrodynamics of a micro-droplet on physicochemical superhydrophobic surfaces. Previous studies neglected the direct effect of surface topography/asperities on the hydrodynamics of the droplet, as well as the simultaneous impact and freezing of the micro-droplet when the size of the droplet and the surface asperities are in the same order of magnitude. Surface asperities is an important property of superhydrophobic coatings, and so these features are incorporated into the model developed here as a series of micro-structured pillars with square cross sections and aligned in a square pattern. In addition, surface chemistry and nano-pillars were simplified through the implementation of Kistler's dynamic contact angle model. For the sake of applicability, the intrinsic contact angle of the stearic acid surface (barely hydrophobic) was imposed on the surface of the micro-structures. To resolve the influence of air around the droplet and between the pillars, extensive simulations were performed for different droplet sizes on a textured surface. Parallel computations with the OpenMP algorithm were used to accelerate computation speed to meet the convergence criteria. It was shown that the composition of the air-solid surface underneath the droplet facilitated capturing the transition from a no-slip/no-penetration condition to a partial-slip with penetration condition as the contact line at the triple point starts moving into the air pockets. The most notable finding to emerge from this study is that the accuracy of the model of capturing the transition from a wetting surface to a non-wetting surface can be achieved by the modelling of surface asperities to resolve the air flow field between the pillars, and including the chemical property of the surface in the form of an appropriate dynamic contact angle model.

Moreover, the roughness effect on the droplets can be successfully analyzed by using the relative roughness, which relates the average surface roughness of the substrate to the initial diameter of the droplet. Therefore, for modelling of superhydrophobic surfaces, we determined the threshhold

of relative roughness (ε=70), below which an assumption of a smooth surface for superhydrophobic surfaces is no longer applicable.

In addition, we showed that direct inclusion of surface roughness in the model has a significant impact on the micro-droplet impact dynamics, including the maximum spreading diameter, penetration depth, and the contact time, factors that were not considered in previous studies. We determined the optimum dimensions for superhydrophobic surface features (size and configuration) to repel cloud-sized particles. The results that were presented here can facilitate improvement in the fabrication of functional superhydrophobic surfaces with high apparent contact angle and minimal contact angle hysteresis. Furthermore, based on the energy balance before and at the instant of maximum spreading, an analytical model was derived. The model is based on an assumption that the micro-droplet is shaped as a disc at the maximum spreading phase. While this study was limited to a specific configuration, it did partially substantiate the reliability of the numerical model by comparing the spreading factors of the droplet on a textured surface.

The phenomenon of ice accretion on a surface is a heat transfer phenomenon. Therefore, we reformulated the enthalpy form of the energy equation with the contribution of the latent heat to account for the phase change, and we solved it simultaneously with the momentum and mass balance equations. In order to track the freezing line during solidification, a second volume fraction indicator was employed to distinguish the solidified region from the liquid region. Special attention was paid to the local freezing (solidification) at the three-phase contact line. The physics of the contact line velocity near the wall was reviewed, and the existing enthalpy-porosity technique was employed to treat the mushy region as a porous medium and to replicate the viscosity change of the liquid as it turns to ice at the wall. For the calculation of heat conduction inside the droplet and through the solid substrate simultaneously, the model was extended to a multiregional solver. This

partitioned technique was used for coupling between the fluid and solid regions, where a separate set of governing equations describing the physics in the respected regions were solved and met convergence conditions at the shared interface. Consequently, 3D models were employed for the heat transfer and simultaneous freezing in the droplet and conduction heat transfer in the substrate. Comparing the impact of a droplet on two substrates with infinitely thin superhydrophilic and superhydrophobic coatings, it was shown that the total heat transfer rate on the superhydrophobic surface was significantly higher despite the smaller contact area with the substrate. The simulations revealed that the better mixing of liquid inside the droplet bulk in the maximum spreading phase was the leading cause of this difference. This data may lead to improvements of the systems where a sudden change of temperature is essential (e.g., ice-free surfaces, spray cooling system).

In the case of cloud particles impacting on superhydrophobic surfaces, it is clear that the wall contact resistance can no longer be oversimplified because at a small size of droplets the roughness effects greatly influence the impact physics. This is due to the dependence of heat transfer to the relative roughness. Therefore, with direct modelling of surface roughness, the contact resistance at the surface was directly modeled and consequently computed from the simulations. Moreover, the net effect of substrate thermal properties on transient heat conduction through the substrate was investigated by studying the impact of a droplet on two substrates with different thermal diffusivities. Aluminium (Al) and a material of low thermal diffusive, in this case titanium dioxide (TiO_2), were used as substrates for these studies. The air-exposed surface of the substrates was composed of microstructures with an intrinsic contact angle replicating the stearic acid sub-micron layer coating. This study aimed to compare the net effect of heat transfer on the hydrodynamics of the micro-droplet for two substrates with different thermal properties but similar surface wettabilities. We found from the simulations that the impacting micro-droplet on a substrate with

a low thermal diffusivity (such as titanium dioxide) bounces off the surface, whereas with aluminum as a substrate, the droplet freezes to the surface due to the higher thermal diffusivity. This effect is caused by a significant delay in the onset of freezing on the substrate with lower diffusivity. Taken together, it was also observed that the onset of freezing occurs from the peripheral edges of the droplet in contact with the surface. It is noteworthy that the internal convection and the bulk-solid heat diffusion preserved the temperature of the liquid bulk in contact with the solid surface slightly above 0°C so that it does not immediately freeze. The evidence from this study indicates that ceramic-based coatings such as TiO_2 have promising anti-icing properties that can be used for the fabrication of ice-free surfaces.

Moreover, a freezing model for supercooled water droplets was derived based on classical nucleation theory. The model is an approximation for a supercooled droplet at the recalescence step, which assumes that freezing is initiated by heterogeneous nucleation at the substrate interface. The model recreates the well-known concave ice front for a freezing water droplet. In addition, the solidification time, which controls the type of ice, is found to evolve exponentially with both maximum droplet spreading diameter and impact velocity. The maximum solidified spreading lengths obtained from the simulations were compared with the data in the literature and they were found to be in good agreement.

In summary, this thesis unveils just the tip of iceberg of the freezing mechanism of cloud-sized particles. Nevertheless, we demonstrated that the models developed herein can serve as a design tool to engineer the surface topology and thermo-physical properties of superhydrophobic coatings to prevent the freezing of cloud-sized droplets in practical flight conditions.

7.1 Future work

For tracking the ice-liquid interface, volume of fluid was used which was operates based on tracking of a volume fraction scalar indicator. Hence there is always some underestimated calculation of the latent heat release during the phase change at the interface. Therefore, future wok may address recalculation of the interface advection based on an interface tracking technique such as Level-set method. Since there is a notable change of density during the solidification process, the volume of the entire droplet changes as it starts freezing. Therefore, future work may address the extension of the current model to account for the density variation of the liquid. In addition, the effect of surface tension change can be included in the model as the droplet solidifies. The current surface tension model can be replaced with a temperature dependent surface tension model to account for the variation of the contact angle during the solidification or evaporation process. Besides, the conjugated heat transfer boundary condition may be extended to simulate the impact and freezing of a supercooled water droplet on textured superhydrophobic surface. Potentially, the model can be extended to include the adhesion of the ice with solid surface as a separate entity to calculate the drag force required to shed the ice from the surface.

An individual study can be performed to investigate the impact of the liquid droplet on textured superhydrophobic surfaces accompanied with air co-flow to determine the change of the droplet contact time and maximum spreading diameter. In addition, the mobility of droplet can be examined in air cross flow situation to determine the change in drag force required to shed the micro-droplet off the textured superhydrophobic surfaces. Last but not least, in order to replicate the scenario of in-flight cloud particles impact, the model can be used to simulate the impact of a micro-droplet on a high-pressure zone resembling stagnation point.

References

[1] S. D. Green, “A study of US inflight icing accidents and incidents, 1978 to 2002,” 2006.

[2] “Aerospaceweb.org | Ask Us - Effect of Rain & Snow on Jet Engines.” [Online]. Available: http://www.aerospaceweb.org/question/propulsion/q0293.shtml. [Accessed: 06-Dec-2017].

[3] “Aircraft icing | Cloudman23.” .

[4] “NTSB cites crew actions in ATR-42 cargo flight crash in Texas,” *ASN News*, 27-Apr-2011. .

[5] N. Ozay, U. Topcu, and R. M. Murray, “Distributed power allocation for vehicle management systems,” in *2011 50th IEEE Conference on Decision and Control and European Control Conference*, 2011, pp. 4841–4848.

[6] L. Cao, A. K. Jones, V. K. Sikka, J. Wu, and D. Gao, “Anti-Icing Superhydrophobic Coatings,” *Langmuir*, vol. 25, no. 21, pp. 12444–12448, Nov. 2009.

[7] S. A. Kulinich and M. Farzaneh, “Ice adhesion on super-hydrophobic surfaces,” *Appl. Surf. Sci.*, vol. 255, no. 18, pp. 8153–8157, Jun. 2009.

[8] A. J. Meuler, J. D. Smith, K. K. Varanasi, J. M. Mabry, G. H. McKinley, and R. E. Cohen, “Relationships between Water Wettability and Ice Adhesion,” *ACS Appl. Mater. Interfaces*, vol. 2, no. 11, pp. 3100–3110, Nov. 2010.

[9] M. Mohammadi, D. D. Pauw, M. Tembely, and A. Dolatabadi, “Droplet Impact and Solidification on Hydrophilic and Superhydrophobic Substrates in Icing Conditions,” in *43rd Fluid Dynamics Conference*, American Institute of Aeronautics and Astronautics.

[10] T. Young, “An essay on the cohesion of fluids,” *Philos. Trans. R. Soc. Lond.*, vol. 95, pp. 65–87, 1805.

[11] F. Ç. Cebeci, Z. Wu, L. Zhai, R. E. Cohen, and M. F. Rubner, “Nanoporosity-driven superhydrophilicity: a means to create multifunctional antifogging coatings,” *Langmuir*, vol. 22, no. 6, pp. 2856–2862, 2006.

[12] T. Sun, L. Feng, X. Gao, and L. Jiang, “Bioinspired surfaces with special wettability,” *Acc. Chem. Res.*, vol. 38, no. 8, pp. 644–652, 2005.

[13] “Water vapor harvesting : Darkling Beetles,” *AskNature*. .

[14] “Lotus effect,” *Wikipedia*. 20-Aug-2017.

[15] L. Chen, Z. Xiao, P. C. H. Chan, Y.-K. Lee, and Z. Li, "A comparative study of droplet impact dynamics on a dual-scaled superhydrophobic surface and lotus leaf," *Appl. Surf. Sci.*, vol. 257, no. 21, pp. 8857–8863, Aug. 2011.

[16] R. N. Wenzel, "Resistance of solid surfaces to wetting by water," *Ind. Eng. Chem.*, vol. 28, no. 8, pp. 988–994, 1936.

[17] A. B. D. Cassie and S. Baxter, "Trans. Faraday Soc.," 1944.

[18] L. Gao and T. J. McCarthy, "Contact angle hysteresis explained," *Langmuir*, vol. 22, no. 14, pp. 6234–6237, 2006.

[19] S. S. Latthe, C. Terashima, K. Nakata, and A. Fujishima, "Superhydrophobic surfaces developed by mimicking hierarchical surface morphology of lotus leaf," *Molecules*, vol. 19, no. 4, pp. 4256–4283, 2014.

[20] C. Josserand and S. T. Thoroddsen, "Drop Impact on a Solid Surface," *Annu. Rev. Fluid Mech.*, vol. 48, no. 1, pp. 365–391, 2016.

[21] A. M. Worthington, "A Study of Splashes, Longman's Green, and Co," *Inc Lond.*, 1908.

[22] G. Yamauchi, K. Takai, and H. Saito, "PTEE based water repellent coating for telecommunication antennas," *IEICE Trans. Electron.*, vol. 83, no. 7, pp. 1139–1141, 2000.

[23] L. Feng, H. Zhang, Z. Wang, and Y. Liu, "Superhydrophobic aluminum alloy surface: fabrication, structure, and corrosion resistance," *Colloids Surf. Physicochem. Eng. Asp.*, vol. 441, pp. 319–325, 2014.

[24] Q. Zhu *et al.*, "Robust superhydrophobic polyurethane sponge as a highly reusable oil-absorption material," *J. Mater. Chem. A*, vol. 1, no. 17, pp. 5386–5393, 2013.

[25] T. Snyder and S. Korol, "Modeling the offset solid-ink printing process," in *International Conference on Digital Printing Technologies*, 1997, pp. 709–715.

[26] Y. Zhang, Y. Chen, P. Li, and A. T. Male, "Weld deposition-based rapid prototyping: a preliminary study," *J. Mater. Process. Technol.*, vol. 135, no. 2–3, pp. 347–357, Apr. 2003.

[27] P. Gao and J. J. Feng, "Enhanced slip on a patterned substrate due to depinning of contact line," *Phys. Fluids 1994-Present*, vol. 21, no. 10, p. 102102, Oct. 2009.

[28] H. Sirringhaus *et al.*, "High-Resolution Inkjet Printing of All-Polymer Transistor Circuits," *Science*, vol. 290, no. 5499, pp. 2123–2126, Dec. 2000.

[29] R. Attarzadeh and A. Dolatabadi, “Numerical study of the effect of surface wettability on performance of the spray cooling process,” *Int. J. Comput. Methods Exp. Meas.*, vol. 4, no. 4, pp. 615–624, Nov. 2016.

[30] R. W. Gent, N. P. Dart, and J. T. Cansdale, “Aircraft icing,” *Philos. Trans. R. Soc. Lond. Math. Phys. Eng. Sci.*, vol. 358, no. 1776, pp. 2873–2911, 2000.

[31] H. Nakanishi, “Splash seed dispersal by raindrops,” *Ecol. Res.*, vol. 17, no. 6, pp. 663–671, Nov. 2002.

[32] S. Edward Law, “Agricultural electrostatic spray application: a review of significant research and development during the 20th century,” *J. Electrost.*, vol. 51, pp. 25–42, May 2001.

[33] Y. J. Jiang, A. Umemura, and C. K. Law, “An experimental investigation on the collision behaviour of hydrocarbon droplets,” *J. Fluid Mech.*, vol. 234, pp. 171–190, Jan. 1992.

[34] S. T. Thoroddsen, T. G. Etoh, and K. Takehara, “High-Speed Imaging of Drops and Bubbles,” *Annu. Rev. Fluid Mech.*, vol. 40, no. 1, pp. 257–285, 2008.

[35] R. Li, N. Ashgriz, S. Chandra, J. R. Andrews, and S. Drappel, “Coalescence of two droplets impacting a solid surface,” *Exp. Fluids*, vol. 48, no. 6, pp. 1025–1035, Jun. 2010.

[36] R. Rioboo, M. Marengo, and C. Tropea, “Time evolution of liquid drop impact onto solid, dry surfaces,” *Exp. Fluids*, vol. 33, no. 1, pp. 112–124, Jul. 2002.

[37] “Drawback During Deposition of Overlapping Molten Wax Droplets | Journal of Manufacturing Science and Engineering | ASME DC.” [Online]. Available: http://manufacturingscience.asmedigitalcollection.asme.org/article.aspx?articleid=1468063. [Accessed: 29-Jul-2017].

[38] D. C. D. Roux and J. J. Cooper-White, “Dynamics of water spreading on a glass surface,” *J. Colloid Interface Sci.*, vol. 277, no. 2, pp. 424–436, 2004.

[39] R. Li, N. Ashgriz, and S. Chandra, “Maximum spread of droplet on solid surface: low Reynolds and Weber numbers,” *J. Fluids Eng.*, vol. 132, no. 6, p. 061302, 2010.

[40] H. Marmanis and S. T. Thoroddsen, “Scaling of the fingering pattern of an impacting drop,” *Phys. Fluids*, vol. 8, no. 6, pp. 1344–1346, 1996.

[41] L. Cheng, “Dynamic spreading of drops impacting onto a solid surface,” *Ind. Eng. Chem. Process Des. Dev.*, vol. 16, no. 2, pp. 192–197, 1977.

[42] S. F. Lunkad, V. V. Buwa, and K. D. P. Nigam, “Numerical simulations of drop impact and spreading on horizontal and inclined surfaces,” *Chem. Eng. Sci.*, vol. 62, no. 24, pp. 7214–7224, 2007.

[43] S. Mukherjee and J. Abraham, “Investigations of drop impact on dry walls with a lattice-Boltzmann model,” *J. Colloid Interface Sci.*, vol. 312, no. 2, pp. 341–354, 2007.

[44] S. Chandra and C. T. Avedisian, “On the Collision of a Droplet with a Solid Surface,” *Proc. R. Soc. Lond. Math. Phys. Eng. Sci.*, vol. 432, no. 1884, pp. 13–41, Jan. 1991.

[45] A. Frohn and N. Roth, *Dynamics of droplets*. Springer Science & Business Media, 2000.

[46] M. Rein, “Interactions between drops and hot surfaces,” in *Drop-Surface Interactions*, Springer, 2002, pp. 185–217.

[47] T. Deng *et al.*, “Nonwetting of impinging droplets on textured surfaces,” *Appl. Phys. Lett.*, vol. 94, no. 13, p. 133109, Mar. 2009.

[48] M. Pasandideh-Fard, Y. M. Qiao, S. Chandra, and J. Mostaghimi, “Capillary effects during droplet impact on a solid surface,” *Phys. Fluids 1994-Present*, vol. 8, no. 3, pp. 650–659, Mar. 1996.

[49] W. J. Rider and D. B. Kothe, “Reconstructing volume tracking,” *J. Comput. Phys.*, vol. 141, no. 2, pp. 112–152, 1998.

[50] D. J. Benson, “Volume of fluid interface reconstruction methods for multi-material problems,” *Appl. Mech. Rev.*, vol. 55, no. 2, pp. 151–165, 2002.

[51] J. E. Pilliod, “An analysis of piecewise linear interface reconstruction algorithms for volume-of-fluid methods,” U. of Calif., Davis., 1992.

[52] F. H. Harlow and J. P. Shannon, “The splash of a liquid drop,” *J. Appl. Phys.*, vol. 38, no. 10, pp. 3855–3866, 1967.

[53] K. TSURUTANI, M. YAO, J. SENDA, and H. FUJIMOTO, “Numerical analysis of the deformation process of a droplet impinging upon a wall,” *JSME Int. J. Ser 2 Fluids Eng. Heat Transf. Power Combust. Thermophys. Prop.*, vol. 33, no. 3, pp. 555–561, 1990.

[54] V. Mehdi-Nejad, J. Mostaghimi, and S. Chandra, “Air bubble entrapment under an impacting droplet,” *Phys. Fluids 1994-Present*, vol. 15, no. 1, pp. 173–183, Jan. 2003.

[55] M. Mohammadi and M. Mohammadi, “Droplet Impact and Solidification on Solid Surfaces in the Presence of Stagnation Air Flow,” phd, Concordia University, 2016.

[56] J. L. Laforte, M. A. Allaire, and J. Laflamme, “State-of-the-art on power line de-icing,” *Atmospheric Res.*, vol. 46, no. 1, pp. 143–158, Apr. 1998.

[57] S. Wang, “Influence of ice accretions on mechanical and electrical performance of overhead transmission lines,” *J. Electr. Mech. Eng.*, vol. 1, no. 1, 2010.

[58] R. Frederking *et al.*, “cold regions science and technology.”

[59] N. Czernkovich, “Understanding in-flight icing,” in *Transport Canada Aviation Safety Seminar*, 2004, pp. 1–21.

[60] J. Hallett, G. Isaac, M. Politovich, D. Marcotte, A. Reehorst, and C. Ryerson, *Alliance Icing Research Study II (AIRS II) science plan*. 2002.

[61] T. G. Myers and J. P. Charpin, “A mathematical model for atmospheric ice accretion and water flow on a cold surface,” *Int. J. Heat Mass Transf.*, vol. 47, no. 25, pp. 5483–5500, 2004.

[62] L. Mishchenko, B. Hatton, V. Bahadur, J. A. Taylor, T. Krupenkin, and J. Aizenberg, “Design of Ice-free Nanostructured Surfaces Based on Repulsion of Impacting Water Droplets,” *ACS Nano*, vol. 4, no. 12, pp. 7699–7707, Dec. 2010.

[63] M. Pasandideh-Fard, S. Chandra, and J. Mostaghimi, “A three-dimensional model of droplet impact and solidification,” *Int. J. Heat Mass Transf.*, vol. 45, no. 11, pp. 2229–2242, May 2002.

[64] S. Tabakova and F. Feuillebois, “On the solidification of a supercooled liquid droplet lying on a surface,” *J. Colloid Interface Sci.*, vol. 272, no. 1, pp. 225–234, 2004.

[65] J. R. Cannon, “The One-dimensional Heat Equation, Addision-Wesley,” *Reading*, 1984.

[66] J. Madejski, “Solidification of droplets on a cold surface,” *Int. J. Heat Mass Transf.*, vol. 19, no. 9, pp. 1009–1013, 1976.

[67] M. Pasandideh-Fard, R. Bhola, S. Chandra, and J. Mostaghimi, “Deposition of tin droplets on a steel plate: simulations and experiments,” *Int. J. Heat Mass Transf.*, vol. 41, no. 19, pp. 2929–2945, 1998.

[68] D. B. Kothe, R. C. Mjolsness, and M. D. Torrey, *RIPPLE: a computer program for incompressible flows with free surfaces*. Available to DOE and DOE contractors from OSTI, 1991.

[69] M. Bussmann, J. Mostaghimi, and S. Chandra, “On a three-dimensional volume tracking model of droplet impact,” *Phys. Fluids 1994-Present*, vol. 11, no. 6, pp. 1406–1417, Jun. 1999.

[70] Y. Cao, A. Faghri, and W. S. Chang, “A numerical analysis of Stefan problems for generalized multi-dimensional phase-change structures using the enthalpy transforming model,” *Int. J. Heat Mass Transf.*, vol. 32, no. 7, pp. 1289–1298, 1989.

[71] H. Liu, E. J. Lavernia, and R. H. Rangel, “Numerical simulation of impingement of molten Ti, Ni, and W droplets on a flat substrate,” *J. Therm. Spray Technol.*, vol. 2, no. 4, pp. 369–378, 1993.

[72] H. Liu, E. J. Lavernia, and R. H. Rangel, “Modeling of molten droplet impingement on a non-flat surface,” *Acta Metall. Mater.*, vol. 43, no. 5, pp. 2053–2072, 1995.

[73] M. Chung and R. H. Rangel, “Simulation of metal droplet deposition with solidification including undercooling and contact resistance effects,” *Numer. Heat Transf. Part Appl.*, vol. 37, no. 3, pp. 201–226, 2000.

[74] H. Zhang, X. Y. Wang, L. L. Zheng, and X. Y. Jiang, “Studies of splat morphology and rapid solidification during thermal spraying,” *Int. J. Heat Mass Transf.*, vol. 44, no. 24, pp. 4579–4592, 2001.

[75] S. D. Aziz and S. Chandra, “Impact, recoil and splashing of molten metal droplets,” *Int. J. Heat Mass Transf.*, vol. 43, no. 16, pp. 2841–2857, 2000.

[76] “Supercooled Water Droplets - SKYbrary Aviation Safety.” [Online]. Available: https://www.skybrary.aero/index.php/Supercooled_Water_Droplets. [Accessed: 08-Sep-2017].

[77] A. Alizadeh *et al.*, “Dynamics of ice nucleation on water repellent surfaces,” *Langmuir*, vol. 28, no. 6, pp. 3180–3186, 2012.

[78] S. Jung, M. K. Tiwari, N. V. Doan, and D. Poulikakos, “Mechanism of supercooled droplet freezing on surfaces,” *Nat. Commun.*, vol. 3, p. 615, 2012.

[79] S. Bauerecker, P. Ulbig, V. Buch, L. Vrbka, and P. Jungwirth, “Monitoring ice nucleation in pure and salty water via high-speed imaging and computer simulations,” *J. Phys. Chem. C*, vol. 112, no. 20, pp. 7631–7636, 2008.

[80] D. Cheremisov and A. Dolatabadi, “Freezing of supercooled water droplets on hydrophobic surface: An experimental study.” Concordia University, 21-Apr-2016.

[81] F. Feuillebois, S. Tabakova, S. Radev, and V. Daru, “Entrained Film of Ice–Water Slurry with Impinging Supercooled Water Droplets,” *J. Eng. Phys. Thermophys.*, vol. 87, no. 1, pp. 51–68, 2014.

[82] T. G. Myers, J. P. F. Charpin, and C. P. Thompson, “Slowly accreting ice due to supercooled water impacting on a cold surface,” *Phys. Fluids*, vol. 14, no. 1, pp. 240–256, 2002.

[83] V. Bahadur, L. Mishchenko, B. Hatton, J. A. Taylor, J. Aizenberg, and T. Krupenkin, “Predictive model for ice formation on superhydrophobic surfaces,” *Langmuir*, vol. 27, no. 23, pp. 14143–14150, 2011.

[84] K. Okumura, F. Chevy, D. Richard, D. Quéré, and C. Clanet, “Water spring: A model for bouncing drops,” *EPL Europhys. Lett.*, vol. 62, no. 2, p. 237, 2003.

[85] M. Mohammadi, M. Tembely, and A. Dolatabadi, “Predictive Model of Supercooled Water Droplet Pinning/Repulsion Impacting a Superhydrophobic Surface: The Role of the Gas–Liquid Interface Temperature,” *Langmuir*, vol. 33, no. 8, pp. 1816–1825, 2017.

[86] B. Zobrist, T. Koop, B. P. Luo, C. Marcolli, and T. Peter, “Heterogeneous Ice Nucleation Rate Coefficient of Water Droplets Coated by a Nonadecanol Monolayer,” *J. Phys. Chem. C*, vol. 111, no. 5, pp. 2149–2155, Feb. 2007.

[87] S. Jung, M. Dorrestijn, D. Raps, A. Das, C. M. Megaridis, and D. Poulikakos, “Are superhydrophobic surfaces best for icephobicity?,” *Langmuir*, vol. 27, no. 6, pp. 3059–3066, 2011.

[88] M. Schremb, I. V. Roisman, and C. Tropea, “Transient effects in ice nucleation of a water drop impacting onto a cold substrate,” *Phys. Rev. E*, vol. 95, no. 2, p. 022805, 2017.

[89] I. V. Roisman, “Inertia dominated drop collisions. II. An analytical solution of the Navier–Stokes equations for a spreading viscous film,” *Phys. Fluids*, vol. 21, no. 5, p. 052104, 2009.

[90] A. L. Yarin, “DROP IMPACT DYNAMICS: Splashing, Spreading, Receding, Bouncing…,” *Annu. Rev. Fluid Mech.*, vol. 38, no. 1, pp. 159–192, Jan. 2006.

[91] A. L. Yarin, I. V. Roisman, and C. Tropea, *Collision Phenomena in Liquids and Solids*. Cambridge University Press, 2017.

[92] G. Yang, K. Guo, and N. Li, “Freezing mechanism of supercooled water droplet impinging on metal surfaces,” *Int. J. Refrig.*, vol. 34, no. 8, pp. 2007–2017, 2011.

[93] H. Li, I. V. Roisman, and C. Tropea, “Water drop impact on cold surfaces with solidification,” in *AIP Conference Proceedings*, 2011, vol. 1376, pp. 451–453.

[94] D. Richard and D. Quéré, “Bouncing water drops,” *EPL Europhys. Lett.*, vol. 50, no. 6, p. 769, 2000.

[95] Š. Šikalo, H.-D. Wilhelm, I. V. Roisman, S. Jakirlić, and C. Tropea, “Dynamic contact angle of spreading droplets: Experiments and simulations,” *Phys. Fluids 1994-Present*, vol. 17, no. 6, p. 062103, Jun. 2005.

[96] H. M. Shang, Y. Wang, S. J. Limmer, T. P. Chou, K. Takahashi, and G. Z. Cao, “Optically transparent superhydrophobic silica-based films,” *Thin Solid Films*, vol. 472, no. 1, pp. 37–43, 2005.

[97] L. Feng *et al.*, “Superhydrophobicity of nanostructured carbon films in a wide range of pH values,” *Angew. Chem. Int. Ed.*, vol. 42, no. 35, pp. 4217–4220, 2003.

[98] P. R. Gunjal, V. V. Ranade, and R. V. Chaudhari, “Dynamics of drop impact on solid surface: experiments and VOF simulations,” *AIChE J.*, vol. 51, no. 1, pp. 59–78, 2005.

[99] S. Mitra *et al.*, “Droplet impact dynamics on a spherical particle,” *Chem. Eng. Sci.*, vol. 100, pp. 105–119, 2013.

[100] C. W. Hirt and B. D. Nichols, “Volume of fluid (VOF) method for the dynamics of free boundaries,” *J. Comput. Phys.*, vol. 39, no. 1, pp. 201–225, Jan. 1981.

[101] H. Rusche, “Computational fluid dynamics of dispersed two-phase flows at high phase fractions,” Imperial College London (University of London), 2003.

[102] S. F. Kistler, “Hydrodynamics of wetting,” *Wettability*, vol. 49, pp. 311–429, 1993.

[103] Š. Šikalo, C. Tropea, and E. N. Ganić, “Impact of droplets onto inclined surfaces,” *J. Colloid Interface Sci.*, vol. 286, no. 2, pp. 661–669, Jun. 2005.

[104] I. V. Roisman, L. Opfer, C. Tropea, M. Raessi, J. Mostaghimi, and S. Chandra, “Drop impact onto a dry surface: Role of the dynamic contact angle,” *Colloids Surf. Physicochem. Eng. Asp.*, vol. 322, no. 1–3, pp. 183–191, Jun. 2008.

[105] P. G. Pittoni, Y.-C. Lin, and S.-Y. Lin, “The impalement of water drops impinging onto hydrophobic/superhydrophobic graphite surfaces: the role of dynamic pressure, hammer pressure and liquid penetration time,” *Appl. Surf. Sci.*, vol. 301, pp. 515–524, May 2014.

[106] M. Denesuk, G. L. Smith, B. J. J. Zelinski, N. J. Kreidl, and D. R. Uhlmann, "Capillary Penetration of Liquid Droplets into Porous Materials," *J. Colloid Interface Sci.*, vol. 158, no. 1, pp. 114–120, Jun. 1993.

[107] K. K. Varanasi, T. Deng, M. Hsu, and N. Bhate, *Hierarchical Superhydrophobic Surfaces Resist Water Droplet Impact*. Nano Science and Technology Institute, 2009.

[108] K. M. Wisdom, J. A. Watson, X. Qu, F. Liu, G. S. Watson, and C.-H. Chen, "Self-cleaning of superhydrophobic surfaces by self-propelled jumping condensate," *Proc. Natl. Acad. Sci. U. S. A.*, vol. 110, no. 20, pp. 7992–7997, 2013.

[109] Q. Zhang, M. He, J. Chen, J. Wang, Y. Song, and L. Jiang, "Anti-icing surfaces based on enhanced self-propelled jumping of condensed water microdroplets," *Chem. Commun.*, vol. 49, no. 40, p. 4516, 2013.

[110] J. B. Boreyko and C. P. Collier, "Delayed Frost Growth on Jumping-Drop Superhydrophobic Surfaces," *ACS Nano*, vol. 7, no. 2, pp. 1618–1627, Feb. 2013.

[111] C. Dietz, K. Rykaczewski, A. G. Fedorov, and Y. Joshi, "Visualization of droplet departure on a superhydrophobic surface and implications to heat transfer enhancement during dropwise condensation," *Appl. Phys. Lett.*, vol. 97, no. 3, p. 033104, Jul. 2010.

[112] A. Menchaca-Rocha, A. Martínez-Dávalos, R. Núñez, S. Popinet, and S. Zaleski, "Coalescence of liquid drops by surface tension," *Phys. Rev. E*, vol. 63, no. 4, p. 046309, Mar. 2001.

[113] M. A. Nilsson and J. P. Rothstein, "The effect of contact angle hysteresis on droplet coalescence and mixing," *J. Colloid Interface Sci.*, vol. 363, no. 2, pp. 646–654, Nov. 2011.

[114] F.-C. Wang, F. Yang, and Y.-P. Zhao, "Size effect on the coalescence-induced self-propelled droplet," *Appl. Phys. Lett.*, vol. 98, no. 5, p. 053112, Jan. 2011.

[115] T. Q. Liu, W. Sun, X. Y. Sun, and H. R. Ai, "Mechanism study of condensed drops jumping on super-hydrophobic surfaces," *Colloids Surf. Physicochem. Eng. Asp.*, vol. 414, pp. 366–374, Nov. 2012.

[116] J. B. Boreyko and C.-H. Chen, "Self-Propelled Dropwise Condensate on Superhydrophobic Surfaces," *Phys. Rev. Lett.*, vol. 103, no. 18, p. 184501, Oct. 2009.

[117] F. Liu, G. Ghigliotti, J. J. Feng, and C.-H. Chen, “Numerical simulations of self-propelled jumping upon drop coalescence on non-wetting surfaces,” *J. Fluid Mech.*, vol. 752, pp. 39–65, Aug. 2014.

[118] N. Miljkovic, D. J. Preston, R. Enright, and E. N. Wang, “Electric-Field-Enhanced Condensation on Superhydrophobic Nanostructured Surfaces,” *ACS Nano*, vol. 7, no. 12, pp. 11043–11054, Dec. 2013.

[119] L. Baroudi, M. Kawaji, and T. Lee, “Effects of initial conditions on the simulation of inertial coalescence of two drops,” *Comput. Math. Appl.*, vol. 67, no. 2, pp. 282–289, Feb. 2014.

[120] R. Narhe, D. Beysens, and V. S. Nikolayev, “Dynamics of Drop Coalescence on a Surface: The Role of Initial Conditions and Surface Properties,” *Int. J. Thermophys.*, vol. 26, no. 6, pp. 1743–1757, Nov. 2005.

[121] M. M. Farhangi, P. J. Graham, N. R. Choudhury, and A. Dolatabadi, “Induced Detachment of Coalescing Droplets on Superhydrophobic Surfaces,” *Langmuir*, vol. 28, no. 2, pp. 1290–1303, Jan. 2012.

[122] S. Moghtadernejad, M. Tembely, M. Jadidi, N. Esmail, and A. Dolatabadi, “Shear driven droplet shedding and coalescence on a superhydrophobic surface,” *Phys. Fluids 1994-Present*, vol. 27, no. 3, p. 032106, Mar. 2015.

[123] B. Peng, S. Wang, Z. Lan, W. Xu, R. Wen, and X. Ma, “Analysis of droplet jumping phenomenon with lattice Boltzmann simulation of droplet coalescence,” *Appl. Phys. Lett.*, vol. 102, no. 15, p. 151601, Apr. 2013.

[124] X. Liu, P. Cheng, and X. Quan, “Lattice Boltzmann simulations for self-propelled jumping of droplets after coalescence on a superhydrophobic surface,” *Int. J. Heat Mass Transf.*, vol. 73, pp. 195–200, Jun. 2014.

[125] X. Shan and H. Chen, “Lattice Boltzmann model for simulating flows with multiple phases and components,” *Phys. Rev. E*, vol. 47, no. 3, pp. 1815–1819, Mar. 1993.

[126] S. Farokhirad, J. F. Morris, and T. Lee, “Coalescence-induced jumping of droplet: Inertia and viscosity effects,” *Phys. Fluids 1994-Present*, vol. 27, no. 10, p. 102102, Oct. 2015.

[127] T. Lee and L. Liu, “Lattice Boltzmann simulations of micron-scale drop impact on dry surfaces,” *J. Comput. Phys.*, vol. 229, no. 20, pp. 8045–8063, Oct. 2010.

[128] H. G. Weller, G. Tabor, H. Jasak, and C. Fureby, “A tensorial approach to computational continuum mechanics using object-oriented techniques,” *Comput. Phys.*, vol. 12, no. 6, pp. 620–631, Nov. 1998.

[129] M. Bussmann, J. Mostaghimi, and S. Chandra, “On a three-dimensional volume tracking model of droplet impact,” *Phys. Fluids*, vol. 11, no. 6, pp. 1406–1417, 1999.

[130] E. Kumacheva and P. Garstecki, *Microfluidic Reactors for Polymer Particles*. John Wiley & Sons, 2011.

[131] C.-H. Chen *et al.*, “Dropwise condensation on superhydrophobic surfaces with two-tier roughness,” *Appl. Phys. Lett.*, vol. 90, no. 17, p. 173108, Apr. 2007.

[132] S. Ganesan, “On the dynamic contact angle in simulation of impinging droplets with sharp interface methods,” *Microfluid. Nanofluidics*, vol. 14, no. 3–4, pp. 615–625, Oct. 2012.

[133] P. G. de Gennes, “Wetting: statics and dynamics,” *Rev. Mod. Phys.*, vol. 57, no. 3, pp. 827–863, Jul. 1985.

[134] A. Ashish Saha and S. K. Mitra, “Effect of dynamic contact angle in a volume of fluid (VOF) model for a microfluidic capillary flow,” *J. Colloid Interface Sci.*, vol. 339, no. 2, pp. 461–480, Nov. 2009.

[135] M. Wu, T. Cubaud, and C.-M. Ho, “Scaling law in liquid drop coalescence driven by surface tension,” *Phys. Fluids 1994-Present*, vol. 16, no. 7, pp. L51–L54, Jul. 2004.

[136] J. Eggers, J. R. Lister, and H. A. Stone, “Coalescence of liquid drops,” *J. Fluid Mech.*, vol. 401, pp. 293–310, Dec. 1999.

[137] M. Reyssat, D. Richard, C. Clanet, and D. Quéré, “Dynamical superhydrophobicity,” *Faraday Discuss.*, vol. 146, pp. 19–33, 2010.

[138] P. Tsai, M. H. W. Hendrix, R. R. M. Dijkstra, L. Shui, and D. Lohse, “Microscopic structure influencing macroscopic splash at high Weber number,” *Soft Matter*, vol. 7, no. 24, pp. 11325–11333, Nov. 2011.

[139] M. Reyssat, A. Pépin, F. Marty, Y. Chen, and D. Quéré, “Bouncing transitions on microtextured materials,” *EPL Europhys. Lett.*, vol. 74, no. 2, p. 306, Mar. 2006.

[140] J. L. Xie, Z. W. Gan, F. Duan, T. N. Wong, S. C. M. Yu, and R. Zhao, “Characterization of spray atomization and heat transfer of pressure swirl nozzles,” *Int. J. Therm. Sci.*, vol. 68, pp. 94–102, Jun. 2013.

[141] J. Kim, “Spray cooling heat transfer: The state of the art,” *Int. J. Heat Fluid Flow*, vol. 28, no. 4, pp. 753–767, Aug. 2007.

[142] F. Girard, E. Meillot, S. Vincent, J. P. Caltagirone, and L. Bianchi, “Contributions to heat and mass transfer between a plasma jet and droplets in suspension plasma spraying,” *Surf. Coat. Technol.*, vol. 268, pp. 278–283, Apr. 2015.

[143] “Effects of Injection Pressure and Nozzle Geometry on Spray SMD and D.I. Emissions.” [Online]. Available: http://papers.sae.org/952360/. [Accessed: 03-Jul-2016].

[144] R. Attarzadeh and A. Dolatabadi, “Coalescence-induced jumping of micro-droplets on heterogeneous superhydrophobic surfaces,” *Phys. Fluids*, vol. 29, no. 1, p. 012104, Jan. 2017.

[145] T. L. Bergman and F. P. Incropera, *Fundamentals of heat and mass transfer*. John Wiley & Sons, 2011.

[146] D. Richard, C. Clanet, and D. Quéré, “Surface phenomena: Contact time of a bouncing drop,” *Nature*, vol. 417, no. 6891, pp. 811–811, Jun. 2002.

[147] S. Farhadi, M. Farzaneh, and S. A. Kulinich, “Anti-icing performance of superhydrophobic surfaces,” *Appl. Surf. Sci.*, vol. 257, no. 14, pp. 6264–6269, May 2011.

[148] M. Mohammadi, M. Tembely, and A. Dolatabadi, “Supercooled Water Droplet Impacting Superhydrophobic Surfaces in the Presence of Cold Air Flow,” *Appl. Sci.*, vol. 7, no. 2, p. 130, Jan. 2017.

[149] Y. Wang, J. Xue, Q. Wang, Q. Chen, and J. Ding, “Verification of Icephobic/Anti-icing Properties of a Superhydrophobic Surface,” *ACS Appl. Mater. Interfaces*, vol. 5, no. 8, pp. 3370–3381, Apr. 2013.

[150] J. C. Bird, R. Dhiman, H.-M. Kwon, and K. K. Varanasi, “Reducing the contact time of a bouncing drop,” *Nature*, vol. 503, no. 7476, pp. 385–388, Nov. 2013.

[151] A. J. B. Milne and A. Amirfazli, “Drop shedding by shear flow for hydrophilic to superhydrophobic surfaces,” *Langmuir*, vol. 25, no. 24, pp. 14155–14164, 2009.

[152] B. L. Scheller and D. W. Bousfield, “Newtonian drop impact with a solid surface,” *AIChE J.*, vol. 41, no. 6, pp. 1357–1367, 1995.

[153] Š. Šikalo, M. Marengo, C. Tropea, and E. N. Ganić, “Analysis of impact of droplets on horizontal surfaces,” *Exp. Therm. Fluid Sci.*, vol. 25, no. 7, pp. 503–510, Jan. 2002.

[154] J. Fukai *et al.*, “Wetting effects on the spreading of a liquid droplet colliding with a flat surface: experiment and modeling,” *Phys. Fluids*, vol. 7, no. 2, pp. 236–247, 1995.

[155] Q. Xu, Z. Li, J. Wang, and R. Wang, “Characteristics of single droplet impact on cold plate surfaces,” *Dry. Technol.*, vol. 30, no. 15, pp. 1756–1762, 2012.

[156] L. Huang, Z. Liu, Y. Liu, Y. Gou, and L. Wang, “Effect of contact angle on water droplet freezing process on a cold flat surface,” *Exp. Therm. Fluid Sci.*, vol. 40, pp. 74–80, 2012.

[157] S. Moghtadernejad, M. Jadidi, M. Tembely, N. Esmail, and A. Dolatabadi, “Concurrent droplet coalescence and solidification on surfaces with various wettabilities,” *J. Fluids Eng.*, vol. 137, no. 7, p. 071302, 2015.

[158] Joshua D. Blake, David S. Thompson, Dominik M. Raps, and Tobias Strobl, “Simulating the Freezing of Supercooled Water Droplets Impacting a Cooled Substrate,” in *52nd Aerospace Sciences Meeting*, 0 vols., American Institute of Aeronautics and Astronautics, 2014.

[159] M. Schremb, S. Borchert, E. Berberovic, S. Jakirlic, I. V. Roisman, and C. Tropea, “Computational modelling of flow and conjugate heat transfer of a drop impacting onto a cold wall,” *Int. J. Heat Mass Transf.*, vol. 109, pp. 971–980, Jun. 2017.

[160] P. Hao, C. Lv, and X. Zhang, “Freezing of sessile water droplets on surfaces with various roughness and wettability,” *Appl. Phys. Lett.*, vol. 104, no. 16, p. 161609, Apr. 2014.

[161] C. W. Visser, Y. Tagawa, C. Sun, and D. Lohse, “Microdroplet impact at very high velocity,” *ArXiv12061574 Phys.*, Jun. 2012.

[162] K. R. Petty and C. D. Floyd, “A statistical review of aviation airframe icing accidents in the US,” in *Proceedings of the 11th Conference on Aviation, Range, and Aerospace Hyannis*, 2004.

[163] J. Madejski, “Solidification of droplets on a cold surface,” *Int. J. Heat Mass Transf.*, vol. 19, no. 9, pp. 1009–1013, 1976.

[164] J.-P. Delplanque and R. H. Rangel, “An improved model for droplet solidification on a flat surface,” *J. Mater. Sci.*, vol. 32, no. 6, pp. 1519–1530, 1997.

[165] D. M. Anderson, M. G. Worster, and S. H. Davis, “The case for a dynamic contact angle in containerless solidification,” *J. Cryst. Growth*, vol. 163, no. 3, pp. 329–338, 1996.

[166] D. M. Anderson and S. H. Davis, “Fluid flow, heat transfer, and solidification near tri-junctions,” *J. Cryst. Growth*, vol. 142, no. 1–2, pp. 245–252, 1994.

[167] V. S. Ajaev and S. H. Davis, “Boundary-integral simulations of containerless solidification,” *J. Comput. Phys.*, vol. 187, no. 2, pp. 492–503, 2003.

[168] J. H. Snoeijer and P. Brunet, “Pointy ice-drops: How water freezes into a singular shape,” *Am. J. Phys.*, vol. 80, no. 9, pp. 764–771, Sep. 2012.

[169] O. R. Enríquez, Á. G. Marín, K. G. Winkels, and J. H. Snoeijer, “Freezing singularities in water drops,” *Phys. Fluids 1994-Present*, vol. 24, no. 9, p. 091102, 2012.

[170] P. Rauschenberger *et al.*, “Comparative assessment of Volume-of-Fluid and Level-Set methods by relevance to dendritic ice growth in supercooled water,” *Comput. Fluids*, vol. 79, pp. 44–52, 2013.

[171] C. Tropea, M. Schremb, and I. Roisman, “Physics of SLD Impact and Solidification,” presented at the European conference for aeronautics and space sciences, Milan (Italy), 2017.

[172] M. Schremb, J. M. Campbell, H. K. Christenson, and C. Tropea, “Ice Layer Spreading along a Solid Substrate during Solidification of Supercooled Water: Experiments and Modeling,” *Langmuir*, vol. 33, no. 19, pp. 4870–4877, 2017.

[173] V. Voller and M. Cross, “An explicit numerical method to track a moving phase change front,” *Int. J. Heat Mass Transf.*, vol. 26, no. 1, pp. 147–150, 1983.

[174] W. Bouwhuis *et al.*, “Maximal air bubble entrainment at liquid-drop impact,” *Phys. Rev. Lett.*, vol. 109, no. 26, p. 264501, 2012.

[175] E. Berberović, I. V. Roisman, S. Jakirlić, and C. Tropea, “Inertia dominated flow and heat transfer in liquid drop spreading on a hot substrate,” *Int. J. Heat Fluid Flow*, vol. 32, no. 4, pp. 785–795, 2011.

[176] F. Gibou, R. Fedkiw, R. Caflisch, and S. Osher, “A level set approach for the numerical simulation of dendritic growth,” *J. Sci. Comput.*, vol. 19, no. 1–3, pp. 183–199, 2003.

[177] J. U. Brackbill, D. B. Kothe, and C. Zemach, “A continuum method for modeling surface tension,” *J. Comput. Phys.*, vol. 100, no. 2, pp. 335–354, Jun. 1992.

[178] B. Van Leer, “Towards the ultimate conservative difference scheme. II. Monotonicity and conservation combined in a second-order scheme,” *J. Comput. Phys.*, vol. 14, no. 4, pp. 361–370, 1974.

[179] H. G. Weller, “A new approach to VOF-based interface capturing methods for incompressible and compressible flow,” *OpenCFD Ltd Rep. TRHGW04*, 2008.

[180] R. Courant, E. Isaacson, and M. Rees, “On the solution of nonlinear hyperbolic differential equations by finite differences,” *Commun. Pure Appl. Math.*, vol. 5, no. 3, pp. 243–255, 1952.

[181] D. L. Barrow and A. H. Stroud, “Existence of Gauss harmonic interpolation formulas,” *SIAM J. Numer. Anal.*, vol. 13, no. 1, pp. 18–26, 1976.

[182] T. Maitra *et al.*, “Supercooled Water Drops Impacting Superhydrophobic Textures,” *Langmuir*, vol. 30, no. 36, pp. 10855–10861, Sep. 2014.

[183] H. S. Carslaw and J. C. Jaeger, *Heat in solids*, vol. 1. Clarendon Press, Oxford, 1959.

[184] H. Miyata, S. Nishimura, and A. Masuko, “Finite difference simulation of nonlinear waves generated by ships of arbitrary three-dimensional configuration,” *J. Comput. Phys.*, vol. 60, no. 3, pp. 391–436, 1985.

[185] C. W. Hirt, A. A. Amsden, and J. L. Cook, “An arbitrary Lagrangian-Eulerian computing method for all flow speeds,” *J. Comput. Phys.*, vol. 14, no. 3, pp. 227–253, 1974.

[186] S. Chen and G. D. Doolen, “Lattice Boltzmann method for fluid flows,” *Annu. Rev. Fluid Mech.*, vol. 30, no. 1, pp. 329–364, 1998.

[187] I. Steinbach *et al.*, “A phase field concept for multiphase systems,” *Phys. Nonlinear Phenom.*, vol. 94, no. 3, pp. 135–147, 1996.

[188] H. Jasak, “Error analysis and estimation for finite volume method with applications to fluid flow,” 1996.

Appendix

Computational tool

All numerical simulations were performed using Open Source Field Operation And Manipulation (OpenFOAM) C++ libraries, a free-source CFD-toolbox developed by OpenCFD[21]. The code is based on the finite-volume numerical method with the co-located variable arrangement for solving systems of transient transport equations on arbitrary unstructured meshes in three-dimensional space. The core idea behind these libraries is the attempt to create tools to allow easy mimic the mathematical representation of PDE's in a high level computational language. OpenFOAM is fully object oriented and uses all the strength of high-level C++.

Numerical methods

Numerical modelling of droplet dynamic belongs to the class of interfacial two phase problems. With the growing computational capabilities and the development of new numerical, the simulation of micro-droplet impact on rough surfaces in icing condition has become possible. One of the key problems is the numerical description of the two-phase flow. There are six methods which are used for the simulation of droplet impact on solid surfaces.

- **Marker and Cell (MAC)** method [184]: the interface is masked by weightless particles that are convectively transported with the velocity field and can be used to reconstruct the interface position on a fixed mesh.
- **Arbitrary Lagrangian-Eulerian (ALE)** method [185]: based on a dynamic mesh that follows the motion of the interface. Thus, the interface coincides with a boundary of the computational domain at all times.

- **Lattice Boltzmann (LB)** method [186]: uses a lattice of weightless particles which are colliding relative to the speed of sound in various directions.
- **Phase-Field method (PFM)** [187]: uses two distinct values (for instance +1 and -1) in each of the phases, with smooth change between both values in the zone around the interface, which is then diffuse with a finite width.
- **Volume of Fluid (VOF)** method [100]: uses a volume tracer carrying information about the volume fraction of each phase in each computational cell in the computational domain.
- **Level-Set (LS)** method: uses a field that carries information about the distance of a numerical cell to the interface and which is convectively transported with the velocity field.

Discretization of numerical schems:

The code uses the Finite Volume (FV) approach to numerically solve the governing PDE's. This means that the computational domain is divided into fixed control volumes, and the solution is obtained on a grid of point. The cells do not overlap with each other.

The discretized values can be stores either in the cell centers, at the surfaces or at the points which span the mesh. In general, the PDE's are discretized by mapping them onto a set of algebraic equations, which in the matrix form can be written as

$$Ax = b, \tag{9-1}$$

Where A is the coefficient matric, x is the variable vector and b is the source term vector. The coefficient of matrix A are determined by the schemes used to discretized given PDE. For discretization, the Gauss integration theorem is used extensively,

$$\int_V \nabla\emptyset \, dV = \int_S dS \, \emptyset$$

$$\int_V \nabla.\emptyset \, dV = \int_S dS.\emptyset \qquad (9\text{-}2)$$

$$\int_V \nabla\times\emptyset \, dV = \int_S dS\times \emptyset$$

which facilitates the conversion of volume integral into a surface integral.

The general equation that will be considered is in the form of:

$$\underbrace{\rho\frac{\partial\emptyset}{\partial t}}_{time} + \underbrace{\nabla.(\rho u\emptyset)}_{convection} = -\underbrace{\frac{\partial p}{\partial x}}_{gradient} + \underbrace{\nabla.(\Gamma\nabla\emptyset)}_{laplacian} + \underbrace{f}_{source} \qquad (9\text{-}3)$$

where $\emptyset$ is an arbitrary variable, Equation above is integrated over control volume V and each individual term is discretized separately.

Following are the numerical schemes used for discretization of solved PDE's and applied numerical models.

Interpolation

In order to interpolate values of a variable from cell centers to face centers, central difference interpolation scheme is used,

$$\emptyset_f = d_x\emptyset_P + (1-d_x)\emptyset_N \qquad (9\text{-}4)$$

where $d_x \equiv \overline{PF_c}/\overline{PN}$. The variables P and N represents the adjacent cell centers, F_c is the cell face center. For a well-structured grid, F_c coincides with the line connecting points P and N. In case it does not happen, additional explicit term may be added [188].

Gradient

The implicit formation of gradient calculates the value at the faces using variable values at the cell centers,

$$(\nabla \emptyset)_f = \frac{\emptyset_N - \emptyset_P}{|\mathrm{d}|} \tag{9-5}$$

And the explicit formulation interpolates gradient values at the cell center using Gauss interpolation theorem,

$$\int_V \nabla \emptyset \, dV = \int_S dS_f \emptyset = \sum_f S_f \emptyset_f \tag{9-6}$$

Laplacian

The Laplacian term is integrated over a control volume and, after applying Gauss theorem, discretized in the following way,

$$\int_V \nabla . (\Gamma \nabla \emptyset) \, dV = \int_S dS . (\Gamma \nabla \emptyset) = \sum_f \Gamma_f S_f . (\nabla \emptyset)_f \tag{9-7}$$

Convection

The integrated and linearized convection term can be written as,

$$\int_V \nabla . (\rho \mathrm{U} \emptyset) \, dV = \int_S dS . (\rho \mathrm{U} \emptyset) = \sum_f S_f . (\rho \mathrm{U})_f \emptyset_f = \sum_f \mathrm{I} \, \emptyset_f \tag{9-8}$$

where $\mathrm{I} \equiv S_f . (\rho \mathrm{U})_f$ is the normal flux through the surface. The convection term can be used implicitly, in which case it returns matrix parameters.

Divergence

The divergence term is strictly explicit. In opposition to convection term it is not product with the velocity field. It is integrated over control volume and discretized in the following way,

$$\int_V \nabla . \emptyset \, dV = \int_S dS . \emptyset = \sum_f S_f . \emptyset_f \tag{9-9}$$

Source terms

The source terms are incorporated into the equations in explicit or implicit way. The explicit source terms are put into eqn.(9-1) directly as the b parameter. The implicit source terms are integrated over control volume and linearized:

$$\int_V \rho \emptyset \, dV = \sum_f \rho_P V_P \, \emptyset_P \tag{9-10}$$

First order time derivative

The first time derivative is integrated over control volume as follow:

$$\frac{\partial}{\partial t} \int_V \rho \emptyset \, dt \tag{9-11}$$

The time is discretized into time steps Δt. In order to model the change in time the following values are used:

New values	$\emptyset^n \equiv \emptyset(t + \Delta t)$	at the time step that is being solved;
Old values	$\emptyset^o \equiv \emptyset(t)$	from the previous time step;
Old-old values	$\emptyset^{oo} \equiv \emptyset(t - \Delta t)$	from the time step previous to the last one.

Two time schemes are considered

Euler implicit that is first order accurate in time:

$$\frac{\partial}{\partial t}\int_V \rho\emptyset\, dt = \frac{(\rho_P\emptyset_P V)^n - (\rho_P\emptyset_P V)^o}{\Delta t} \tag{9-12}$$

Backward differencing that is second order accurate in time, but requires storage of old-old values:

$$\frac{\partial}{\partial t}\int_V \rho\emptyset\, dt = \frac{3(\rho_P\emptyset_P V)^n - 4(\rho_P\emptyset_P V)^o + (\rho_P\emptyset_P V)^{oo}}{2\Delta t} \tag{9-13}$$

Time integration

All equations are integrated in time over one time step. Let Λ be a general spatial operator (eg. Laplacian, Divergence), and Λ^*be its spatial discretized form.

$$\int_t^{t+\Delta t}\left[\int_V \rho\emptyset\, dV\right]\mathrm{dt} = \int_t^{t+\Delta t}\Lambda\emptyset dt \approx \int_t^{t+\Delta t}\Lambda^*\emptyset^n dt \tag{9-14}$$

The time integral can be represented in three way,

Implicit uses current values $\emptyset^n$. It is first order in time accurate guarantees boundedness and it unconditionally stable,

$$\int_t^{t+\Delta t}\Lambda^*\emptyset dt = \Lambda^*\emptyset^n\Delta t \tag{9-15}$$

Explicit takes the old values $\emptyset^o$,

$$\int_t^{t+\Delta t}\Lambda^*\emptyset\, dt = \Lambda^*\emptyset^o\Delta t \tag{9-16}$$

It is the first order accurate in time and remains stable until courant number *Co* is smaller than one,

$$Co = \frac{U_f.\mathrm{d}}{|\mathrm{d}|^2}\Delta t < 1 \tag{9-17}$$

Crank Nicholson is second order in time accurate. It takes the average of current value $\emptyset^n$ and old value $\emptyset^o$. It is unconditionally stable but does not guarantee boundness.

$$\int_t^{t+\Delta t} \Lambda^* \emptyset \, dt = \Lambda^* \left(\frac{\emptyset^n + \emptyset^o}{2} \right) \Delta t \tag{9-18}$$

Boundary conditions

There are two types of boundary conditions that may be selected:

Dirichlet condition that specifies a value to variable at the boundary nodes. It is often referred to as fixed value boundary condition. If value $\emptyset_b$ is given, then the gradient of this value can be found,

$$(\nabla \emptyset)_b = \frac{\emptyset_b - \emptyset_p}{|\mathrm{d}|} \tag{9-19}$$

Neumann condition which sets a gradient of a value onto the boundary nodes. It is also known as fixed gradient boundary condition. For a fixed gradient of $(\nabla \emptyset)_b$ the value of $\emptyset_b$ can be found:

$$\emptyset_b = \emptyset_p + |\mathrm{d}|.(\nabla \emptyset)_b \tag{9-20}$$

Coupling boundary condition

The boundary condition on both sides of the coupled domain have to satisfy the continuity of flux at the coupled interface,

$$\begin{cases} T_{\lambda \to f} = T_{\lambda \to s} = T_\lambda \\ k_f \left(\dfrac{\partial T_f}{\partial n_f} \right) = k_s \left(\dfrac{\partial T_s}{\partial n_s} \right) \end{cases} \tag{9-21}$$

Where $T_{\lambda \to f}, T_{\lambda \to s}$ is the value of Temperature field in fluid and solid domain at the interface, and T_λ the interface value of temperature.

Coupling conditions (Dirichlet-Neumann)

Start from equating the gradient to calculate the T_λ

$$k_f \frac{T_f - T_\lambda}{\Delta_f} = k_s \frac{T_\lambda - T_s}{\Delta_s} \tag{9-22}$$

Finding T_λ and initializing wall temperature,

$$T_\lambda = \frac{k_f \Delta_s T_f + k_s \Delta_f T_s}{k_f \Delta_s + k_s \Delta_f} \tag{9-23}$$

Solving fluid with wall temperature,

$$T_{\lambda - f} = \frac{k_f \Delta_s T_f + k_s \Delta_f T_s}{k_f \Delta_s + k_s \Delta_f} \tag{9-24}$$

Mapping wall gradient for solid calculations,

$$k_s \left(\frac{\partial T}{\partial n}\right)_{\lambda - s} = k_f \frac{T_f - T_\lambda}{\Delta_f} \tag{9-25}$$

Boundary coupling chart,

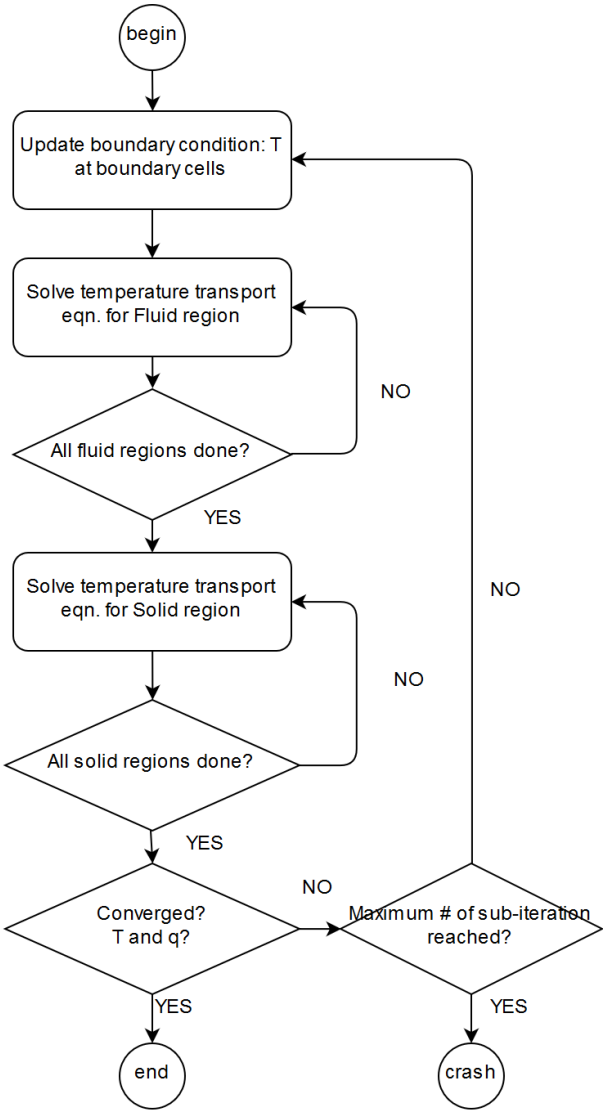

Adaptive time step control

Since the flow field is unknown at the beginning of the calculation, introducing a proper value for time step is tricky. In addition, during the calculation if the values of the time step are not controlled, this may result in an unstable solution unless very small time steps are chosen. However, extremely small time steps consume much more computational efforts. Therefore, using adjustable or adaptive time step enables accurate calculations and reduce the computational effort. The time step is adjusted according to the prescribed maximum Courant number and maximum time step size. The new time step is initiated from the following form:

$$\Delta t = \min\left\{\min\left[\min\left(\frac{Co_{\max}}{Co_o}\,\Delta t_o, \left(1+\lambda_1\frac{Co_{\max}}{Co_o}\right)\Delta t_o\right), \lambda_2\Delta t_o\right], \Delta t_{\max}\right\} \quad (9\text{-}26)$$

where the courant number is determined from eq.(9-17).

The local courant number Co_o is calculated using valued drom the previous (old) time step. In order to avoid time step oscillation, the increase of the time step is damped using the factors λ_1 and λ_2. At the beginning of the calculation the time step size is evaluated from

$$\Delta t_o = \min\left(\frac{Co_{\max}\Delta t_{\text{init}}}{Co_o}, \Delta t_{\max}\right) \quad (9\text{-}27)$$

And this intermediate value is then used in eqn.(9-26) in order to ensure that the value of Co_o at the initial time step be close to the prescribed limit value $Co_{\max}$.

Continuum surface force model

At the free surface of a fluid, an imbalance in molecular forces between adjacent sides of the interface can result in a surface force existing at the interface. This surface force, known as surface tension, is directed normal to the interface and is dependent on the curvature of the fluid interface for magnitude. Surface tension is calculated in OpenFOAM using the Continuum Surface Force (CSF) model of Brackbill et al.[177]. Under the CSF model, surface tension surface forces are replaced by a volume force, which acts on the fluid within a small transitional region surrounding the interface. The CSF model has been shown to represent surface tension behaviour accurately

for a wide variety of problems. Under the CSF model, the surface tension volume force is defined by [177],

$$\lim_{n\to 0}\int_{\Delta V} \mathrm{F}_{sv}(\mathrm{x})d^3x = \int_{\Delta A} \mathrm{F}_{sa}(\mathrm{x_s})dA \tag{9-28}$$

In this equation, $\mathrm{F}_{sa}(\mathrm{x_s})$ is the surface force resulting from surface tension at location $\mathrm{x_s}$. This force is integrated over a small area of the free surface, ΔA. $\mathrm{F}_{sv}(\mathrm{x})$ is the CSF volume force equivalent to F_{sa} , and is integrated over a small volume surrounding the surface, ΔV. The width of the transition region surrounding the surface is n, such that $\Delta V = n \times \Delta A$. The surface tension surface force, F_{sa}, can be defined as

$$\mathrm{F}_{sa}(\mathrm{x_s}) = \sigma\kappa(\mathrm{x_s})\ \hat{\mathrm{n}}\ (\mathrm{x_s}), \tag{9-29}$$

where σ is the surface tension coefficient for the fluids, $\kappa(\mathrm{x_s})$ is the curvature of the free surface, defined positive if the centre of curvature is located on the fluid side of the interface, and $\hat{\mathrm{n}}\ (\mathrm{x_s})$ is a unit normal to the interface, directed towards the fluid side of the interface. Using the method of Brackbill et al.[177], equations (9-28)and (9-29) can be combined to give the CSF volume force simply as,

$$\mathrm{F}_{sv}(\mathrm{x}) = \sigma\kappa(\mathrm{x})\ n\ (\mathrm{x}) \tag{9-30}$$

where the surface normal are defined as the gradient of the VOF function,

$$\mathrm{n}(\mathrm{x}) = \nabla F(x) \tag{9-31}$$

and the curvature is defined as the negative divergence of the unit normal,

$$\kappa(\mathrm{x}) = -\left(\nabla.\,\hat{\mathrm{n}}\ (\mathrm{x})\right). \tag{9-32}$$